University of Exeter

College of Engineering, Mathematics and Physical Sciences

Department of Mathematics and Computer Science

A New Way to Quantify Stratosphere-Troposphere Coupling in Observations and Climate Models

Thomas Daniel Clemo

November 2017

Supervisors:

Mark BALDWIN
David STEPHENSON

Abstract

Atmospheric mass is transported in and out of the stratospheric polar cap region by a wave-driven meridional circulation. Using composites of polar cap pressure anomalies, defined as deviations from the average annual cycle, it is shown that this stratospheric mass flux is accompanied by a similar mass flux near the surface. This '*tropospheric amplification*' of the stratospheric signal is introduced as a new way to quantify stratosphere-troposphere coupling. Regression analysis is used to create a vertical profile of atmospheric pressure during a tropospheric amplification event, and the regression slope profile is used as a tool to quantify the amplification. Using data from 5 reanalysis datasets and 11 climate models, it is shown that high-top models, with a model lid of above 1 hPa, are significantly better at reproducing tropospheric amplification than low-top models, due to having more detailed parameterisations of stratospheric processes. However, the regression slope profiles of all models, bar one, are significantly different to the profile of reanalysis data at a 95% confidence level. Tropospheric amplification is also investigated in historical and future simulations from these models, and it is concluded that there is not expected to be a large change in the phenomenon over the next 100 years. The processes needed to reproduce tropospheric amplification can be identified by comparing idealised models of different complexity. A simple dry-core model is not able to reproduce tropospheric amplification, while a model with a comprehensive radiation scheme does produce the basic regression slope profile under certain configurations. The associations between pressure change and mass flux are further investigated using primitive equations. It is found that vertical and horizontal contributions to mass flux act to mostly cancel each other out, leaving a poorly-conditioned residual, and that the horizontal mass flux across the polar cap boundary has both geostrophic and ageostrophic components.

Contents

List of Figures

7

List of Tables

List of Abbreviations

AO   Arctic Oscillation

BDC   Brewer-Dobson Circulation

CCM   Chemistry-Climate Model

CCMVal   Chemistry-Climate Model Validation activity

CMAM   Canadian Middle Atmosphere Model

CMIP3   Coupled Model Intercomparison Project, Phase 3

CMIP5   Coupled Model Intercomparison Project, Phase 5

ECMWF   European Centre for Medium-Range Weather Forecasts

ENSO   El Niño Southern Oscillation

EOF   Empirical Orthogonal Function

ERA   ECMWF Re-Analysis

GCM   General Circulation Model

GFDL-SDC   Geophysical Fluid Dynamics Laboratory, Spectral Dynamical Core

MiMA   Model of an idealised Moist Atmosphere

NAM   Northern Annular Mode

NAO   North Atlantic Oscillation

PCA   Principal Component Analysis

PNJ   Polar Night Jet

PV   Potential Vorticity

QBO   Quasi-Biennial Oscillation

RCP   Representative Concentration Pathway

S-T   Stratosphere-Troposphere

SAM   Southern Annular Mode

SPARC   Stratosphere-troposphere Processes and their Role in Climate

SSW   Sudden Stratospheric Warming

WCRP   World Climate Research Programme

Acknowledgements

1 Introduction

1.1 Overview

Stratospheric variability has become an increasingly relevant area of active research as we begin to understand more about its role on the weather patterns we experience on the Earth's surface. It has been shown to affect both short-term and seasonal weather patterns (Gerber et al., 2012; Baldwin and Dunkerton, 2001), and has been associated with the position of the mid-latitude jet stream and storm track (Gerber et al., 2012), tropospheric blocking patterns (Woollings et al., 2010), and the surface annular modes (Baldwin and Thompson, 2009; Simpson et al., 2011). At longer timescales, predictable changes in the strength of stratospheric circumpolar flow resulting from other atmospheric processes can lead to an increase in forecasting skill (Baldwin et al., 2003; Kidston et al., 2015). However, we still do not fully understand the mechanisms which couple the stratosphere to the troposphere (Gerber et al., 2012; Kidston et al., 2015).

In order to better understand stratospheric processes, climate models are now more frequently being configured to include the stratosphere and lower mesosphere; initially, this was mainly to simulate ozone chemistry, but now also as an attempt to generally improve climate model performance (Gerber et al., 2010; Osprey et al., 2013).

The aims of this thesis are as follows:

1. To introduce a new way to quantify stratosphere-troposphere (S-T) coupling through the movement of mass in and out of the polar cap, as measured by mean polar cap pressure at fixed heights.

2. To quantitatively investigate tropospheric amplification in reanalysis data and climate model output. By using models of varying complexity, from a simple dynamical core model to a complex General Circulation Model (GCM), with at least one intermediate model, it should be possible to determine which physical processes, e.g. baroclinic eddies, are required in the model to recreate

tropospheric amplification, from which the dynamical mechanisms behind the amplification itself could be inferred.

3. To discover how tropospheric amplification is likely to change in the future as a result of greenhouse warming, and the associated stratospheric cooling, using RCP (Representative Concentration Pathway) scenarios of the previously-investigated GCMs, and discuss alterations that may need to be made to forecasting or climate management as a result of this.

4. To study the underlying stratospheric and tropospheric mass fluxes involved in tropospheric amplification – primarily the fluxes of mass into and out of the polar cap – in order to assess the contribution of the zonal mean and eddy components of the meridional flow, and to investigate the effects of both vertical and horizontal mass movement on the resulting pressure deviation.

1.2   Structure

Chapter 2 provides a review of recent literature on S-T dynamics, focusing primarily on interactions between the stratosphere and the troposphere, meridional stratospheric circulation, the use of climate models in stratospheric prediction, and the current state of research into S-T coupling mechanisms. Chapter 3 then goes on to introduce tropospheric amplification and its relationship to other known phenomena, such as the polar vortex and the Northern and Southern Annular Modes (NAM/SAM), with reference to the ERA-interim reanalysis. Chapter 4 continues this investigation by comparing with other reanalysis datasets, and Chapter 5 subsequently considers historical simulations from a number of climate models. The second half of Chapter 5 takes these same climate models and uses their RCP scenarios to explore future projections, while Chapter 6 focuses on less complex climate models in order to ascertain what level of complexity is needed to sufficiently recreate tropospheric amplification. Chapter 7 returns to the ERA-interim data to further investigate mass fluxes. Finally, Chapter 8 presents the conclusions of the project and discusses possible future directions for this research.

2 Background

2.1 Overview

This chapter provides a review of the background information surrounding S-T dynamics. The first section focuses on interactions between the stratosphere and the troposphere, starting with the structure of the atmosphere before moving on to discussion of atmospheric processes and their timescales. Section 2.3 introduces the Brewer-Dobson circulation, a meridional circulation of the stratosphere. Section 2.4 then introduces empirical orthogonal functions, which can be used to decompose a field into space and time components. Sections 2.5 and 2.6 review respectively the use of climate models in stratospheric prediction, and the consistency between those models and reanalysis data. Finally, 2.7 covers the current state of research into S-T coupling mechanisms.

2.2 Stratosphere-Troposphere Interaction

The review papers by Holton et al. (1995), Haynes (2005), and Kidston et al. (2015) present a good starting point on the field of stratosphere-troposphere (S-T) coupling. Holton et al. (1995) aimed to not only review synoptic and small-scale mechanisms of S-T exchange, but also those on a global scale; a factor which had not been considered in much detail in prior studies. They made the important division between an 'overworld' and a 'lowermost stratosphere', where the latter acts as a boundary layer between the stratosphere and troposphere, as shown in Figure 2.1 by the shaded area. The boundary between these divisions was designated along the 380K isentropic surface (which is around 100 hPa), above which isentropic surfaces are wholly within the stratosphere, and below which isentropic surfaces intersect the tropopause (the thick line in Fig. 2.1). The lowermost stratosphere directly exchanges mass with the troposphere by transport along these isentropic surfaces. Mass transport between the overworld and lowermost stratosphere occurs at a much slower rate, and is driven by eddy motions. Holton et al. (1995) concluded that S-T exchange is controlled by the generation of Rossby waves and gravity waves in
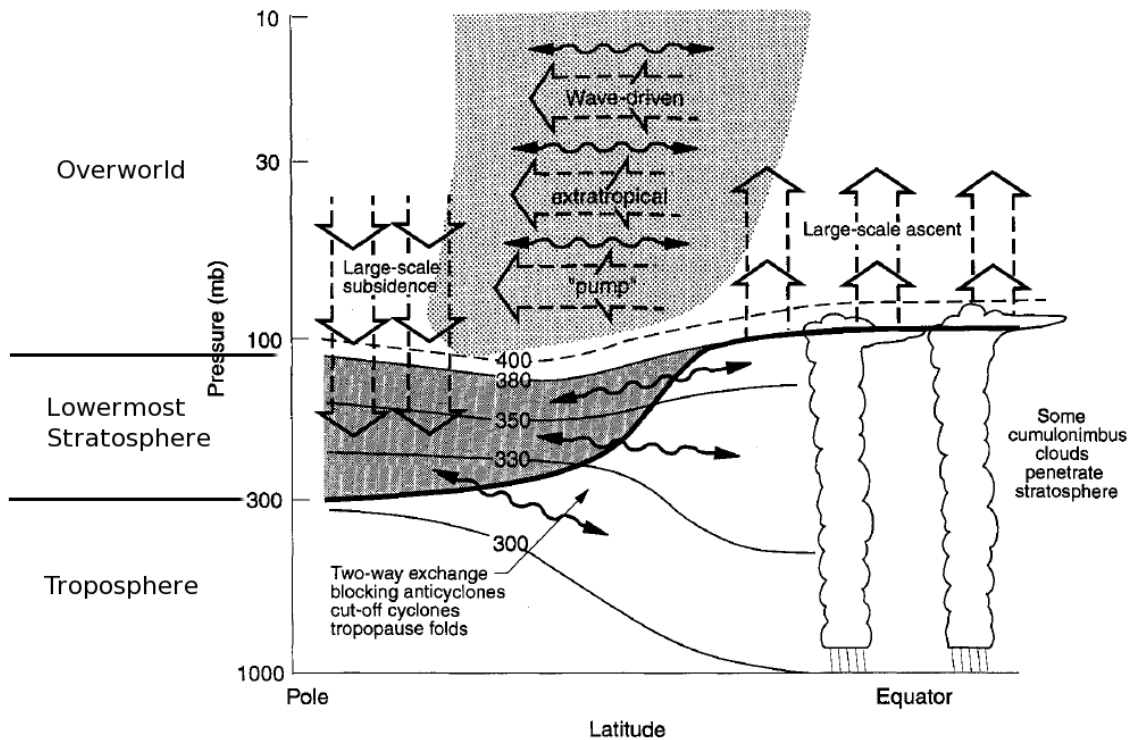
Figure 2.1: Dynamical aspects of stratosphere-troposphere exchange. (From Holton et al., 1995, Fig. 3.)

the troposphere which propagate upwards and dissipate, creating a westward zonal force. Gravity waves are caused by vertical oscillations of a fluid parcel in a stably-stratified atmosphere. Gravity waves propagate upwards through the troposphere and stratosphere, and typically break in the middle of the mesosphere, resulting in a significant descent of mesospheric air into the stratosphere (Plumb, 2002). Rossby waves, or planetary waves, are features in the global circulation currents caused by conservation of potential vorticity and influenced by the Coriolis force and diabatic heating. These waves typically break in the mid-stratosphere, where conservation of potential vorticity results in a westward flow. Air moving westwards is also directed polewards by the Coriolis force, inducing what has been named the 'wave-driven pump' (see Section 2.3).

Upward-propagating Rossby waves from the troposphere are known to disturb the stratospheric polar vortex (Holton et al., 1995). With sufficient wave forcing, the vortex may be displaced from the pole, or divided into two parts. This causes descent and adiabatic warming, which can be diagnosed by inversion of the potential vorticity (PV) field. This split or displacement of the vortex and the associated adi-
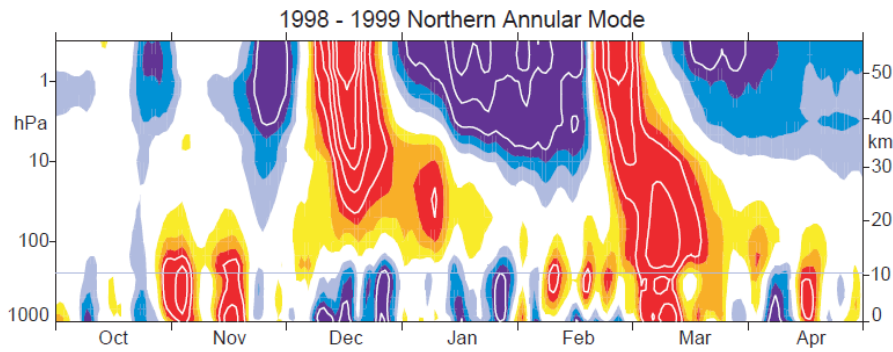
Figure 2.2: Time-height development of the northern annular mode during the winter of 1998–1999. Blue corresponds to positive values (strong polar vortex), and red corresponds to negative values (weak polar vortex). (From Baldwin and Dunkerton, 2001, Fig. 1.)

abatic warming is known as 'sudden stratospheric warming' (SSW) (Haynes, 2005). Based on observations of variations in the polar vortex, Baldwin and Dunkerton (2001) presented the idea that it may be possible to predict tropospheric weather 'regimes' based on earlier stratospheric 'harbingers'. They noted that there appears to be an association between a change in strength of the polar vortex and the particular weather systems that occur in the troposphere in the following 60 days (Fig. 2.3, composited from events like those seen in Fig. 2.2), and that the strength of the polar vortex is characterised by the annular modes. The Northern Annular Mode (NAM) and Southern Annular Mode (SAM) are large scale patterns of variability in the atmospheric circulations of each hemisphere. Baldwin and Dunkerton (2001) showed that large, positive anomalies in the NAM represent a strong, organised vortex, while negative anomalies indicate a weak, chaotic vortex. They also showed that the Atlantic storm track is displaced further to the south during the 60 days following a weak vortex event. The study in Baldwin and Dunkerton (2001) followed on from Baldwin and Dunkerton (1999), in which they detailed downward propagation of anomalies in the Arctic Oscillation pattern (AO, identical in concept to the NAM) from the stratosphere to the troposphere, and discussed the evidence of stratospheric anomalies preceding tropospheric weather patterns. The study also led on to Baldwin et al. (2003), in which they qualified the additional skill of using the stratosphere to forecast the AO using an empirical statistical model, and suggested that the time-scale of NAM variations is an important factor in understanding how stratospheric circulation affects the troposphere.
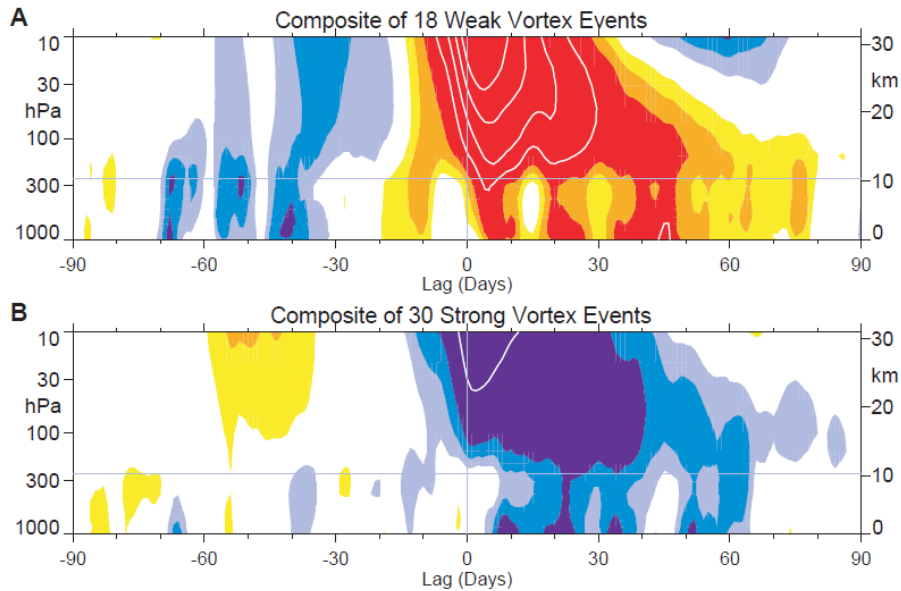
Figure 2.3: Composites of time-height development of the northern annular mode for (A) 18 weak vortex events and (B) 30 strong vortex events. (From Baldwin and Dunkerton, 2001, Fig. 2.)

Whereas Baldwin and Dunkerton (2001) looked at the immediate and intraseasonal coupling between the stratosphere and the troposphere, Ivy et al. (2014) investigated connections between decadal changes in the Arctic tropospheric and stratospheric circulations. By examining 'dynamically quiescent' (inert) years, that is years without major SSWs, they found that there has been a trend towards a stronger polar vortex and colder mid-stratosphere temperatures in the polar region. They did note however that due to the increase in the frequency of SSWs, the number of quiescent years since 2000 is low, and the results may be biased as a consequence. They concluded by saying that the downward propagation of temperature and geopotential height trends within the stratosphere in quiescent years is robust, while the stratospheric trends in these fields do not clearly couple with tropospheric values during these years. This reinforces the 'harbingers' idea of Baldwin and Dunkerton (2001) by presenting a complementary case; i.e., if a major stratospheric event occurs, the phase of zonal mean zonal wind anomalies tends to propagate downwards into the troposphere, but if no major stratospheric events occur, there is no downward phase propagation. This raises the question over whether there may be a linear relationship between the strength of the polar vortex, and the state of the NAM, both of which are affected by tropospheric wave fluxes. This however is

different to the Antarctic S-T coupling, where sudden stratospheric warmings are rare, with only one event during an active season (Thompson et al., 2005), due to the stronger southern vortex suppressing upward propagation of planetary waves. As a result, the downward influence of the stratosphere is stronger in the Southern Hemisphere, suppressing planetary wave variability and leading to a quasi-steady circumpolar flow (Kidston et al., 2015). Despite the potential bias in the results, Ivy et al. (2014) made useful progress in evaluating long-term trends, as they were able to examine the years without major events and integrate that with previous results to create a clearer picture of the whole. This could be extended by investigating future climate simulations in models.

Reichler et al. (2005) considered a related situation by examining 'troposhere-stratosphere-troposhere' events; that is, specific events which start as a planetary wave in the tropsphere, propagate up to the stratosphere, and directly cause a circulation anomaly which propagates back down to the troposphere. The lag time for the associated zonal mean circulation anomaly to propagate back down to the troposphere, of between 30 and 100 days, is related to the wave drag in the zonal mean circulation. Where the maximum eddy driving is higher in the stratosphere, the lag time is longer, as it takes the initial wave longer to propagate to that height, and the resulting circulation anomaly longer to propagate down. It was therefore possible for Reichler et al. (2005) to devise criteria to predict the long-term surface response to a tropospheric planetary wave pulse.

Gerber et al. (2009) extended the work of Baldwin and Dunkerton (2001) and Baldwin et al. (2003) to demonstrate that there is an active downward influence of the stratosphere on the troposphere, and not just a passive response which is solely driven by tropospheric processes. Using an idealised General Circulation Model (GCM), they initiated an ensemble forecast before an SSW, and as long as each ensemble member produced the same SSW, they were able to isolate a robust signal in the troposphere as a direct response to stratospheric anomalies above. Any residual upward-propagating dynamics in the troposphere would have been erased as the ensemble members separated due to synoptic variability. They concluded

that even though the SSW is forced by tropospheric wave activity, the SSW signal is preserved in the stratosphere and is able to influence the troposphere after a long lag time. The signal results in a persistent equatorward shift of the eddy-driven tropospheric jet stream following an SSW, lasting for around two months.

Gerber et al. (2009) also suggested that forecast skill can be improved by resolving the stratosphere and incorporating stratospheric data in forecast models. Forecast skill is derived from slow, predictable factors at the surface, such as extratropical sea surface temperature and surface albedo, as well as long-lived factors in the atmosphere, such as the Madden-Julian Oscillation and stratospheric circulation (Baldwin et al., 2003). Predictability of SSWs themselves is limited by the chaotic nature of the troposphere, but predictability of the state of the stratosphere and lower troposphere following an SSW should improve if stratospheric data is included. Due to the lack of any tropospheric precursors in the study of Gerber et al. (2009), it is clear that certain downward aspects of S-T coupling would not be identified without stratospheric processes included in model setups. Excluding these processes would result in limited understanding and less accurate forecasts.

Baldwin et al. (2003) differentiated between the NAM and the AO, where the AO is identical to the NAM at 1000 hPa, but the NAM is defined separately at each isobaric level. This appears to supersede the earlier definition of the AO presented in Baldwin and Dunkerton (1999), and presents a clearer distinction between the two terms. Baldwin and Thompson (2009) explained that while there is a common definition for annular modes, other methods may be used depending on the application. The different methods are mostly based on the leading EOFs (empirical orthogonal functions, see Section 2.4) of geopotential or geopotential height, while a few are based on the EOFs of pressure or zonal wind. They went on to suggest that each method of calculation of annular modes can be useful in particular circumstances. Ambaum et al. (2001) considered the difference between the AO (Arctic Oscillation) and NAO (North Atlantic Oscillation), and concluded that while they are related, they are not the same phenomenon. While the AO is defined using the mean sea level pressure field in the Northern Hemisphere, and has two centres of

action (one over the Pacific, and one over the Atlantic), the NAO is associated with a north-south dipolar structure in the Atlantic pressure field, and therefore has no Pacific component. Ambaum et al. (2001) noted that the correlation between the time series of the NAO and the Atlantic section of the AO is as high as 0.92 during the extended winter (DJFM), but that the difference in the patterns suggests different physical processes, with a regional Atlantic mechanism being responsible for the NAO, as opposed to the zonally symmetric annular mode pattern represented by the AO. They concluded that the NAO is likely to be more relevant with regard to Northern Hemisphere variability than the AO, and that the NAO is more likely to have predictable behaviour.

Charlton et al. (2003) extended the work of Baldwin and Dunkerton (1999, 2001), by establishing the magnitude of the link between the states of the 'stratospheric AO' and the 'tropospheric AO'. Given the previous discussion, this would be equivalent to the NAM in the lower stratosphere and the NAM near the surface, respectively. Prior studies had only qualitatively discussed the link, so attempting to quantify it was an important step in increasing understanding of the processes. Their method included creating a linear regression model to fit the lag times of the time series between stratospheric AO and tropospheric AO, as well as the lag times between tropospheric AO time series and themselves. They identified a relationship between the AO of the lower stratosphere and the AO at 1000 hPa, in which the correlations were statistically significant at 5% over a time-scale of 10-60 days. The correlation itself however was quite low, at around 0.2. They also determined that the relationship appeared strongest at around the height of the tropopause, and during the winter period. Unlike the relationship between the lower stratospheric AO and the tropospheric AO, the relationship between the 1000 hPa AO and itself following some lag time did not appear consistent, with correlation varying between -0.02 and 0.15 over different 10-year slices. In comparison to the focus of Baldwin et al. (2003), where they sought to significantly increase forecast skill using stratospheric memory, Charlton et al. (2003) here suggested an increase in skill of only 5% in forecasting the 1000 hPa AO when including stratospheric information. The forecasting

skill was defined using the mean square error of the forecasted AO divided by the mean square error of the AO climatology,

$$\text{skill} = 1 - \frac{\text{MSE}_{\text{forecast}}}{\text{MSE}_{\text{climatology}}} (\text{Charlton et al., 2003}).$$

In investigating S-T coupling, it is important to understand how different stratospheric phenomena affect each other, as a change in equatorial stratospheric events such as the quasi-biennial oscillation (QBO) could have an impact on polar region surface weather if both the equatorial stratosphere and the polar troposphere are connected to the stratospheric polar vortex. Similarly, a change in the polar stratosphere could have an impact on the equatorial troposphere through the same connection, given the influence of the QBO on the troposphere (e.g. Garfinkel and Hartmann, 2011a,b). Garfinkel and Hartmann (2007) had shown previously that the polar vortex is affected independently by both the QBO and ENSO (El Niño Southern Oscillation). The QBO is an equatorial stratospheric phenomenon whose two states closely resemble the NAM pattern (Watson and Gray, 2014), and the NAM itself represents the state of the polar vortex (Baldwin and Dunkerton, 2001). Watson and Gray (2014) investigated this to show that the polar vortex is weaker during the easterly phase of the QBO. They used a GCM to show that the transient (short-term) response of the polar vortex to a forcing by the QBO is consistent with a mechanism proposed by Holton and Tan (1980), and concluded by saying that similar use of a transient response may be helpful in understanding the influence of the stratosphere on the troposphere.

2.3 Brewer-Dobson Circulation

The Brewer-Dobson circulation (BDC) is a slow global-scale meridional circulation of the stratosphere (Seviour et al., 2012; Butchart, 2014), which characterises stratospheric mass transport and influences the location of stratospheric ozone (Gerber, 2012). The mechanism behind the circulation is the 'wave-driven pump' mentioned previously. Known as the 'wave-driven extratropical pump' in some literature (Holton et al., 1995), a preferable name would be 'Rossby wave pump' (Plumb,

2002), to distinguish it from the related 'gravity wave pump' of the mesosphere. The zonal-mean momentum budget suggests that the mechanism becomes more efficient near the equator (Plumb, 2002; Butchart, 2014), so 'Rossby wave pump' also serves to not downplay the implications of this, whereas 'extratropical' suggests it has no near-equator activity.

The BDC describes Lagrangian-mean transport (Butchart, 2014; Seviour et al., 2012), characterised by a single-cell stratospheric system, and works in partial opposition to the Eulerian-mean meridional stratospheric circulation, which is a two-cell system (Butchart, 2014; Matsuno and Nakamura, 1979). 'Lagrangian-mean transport' refers to mass transport within the Lagrangian-mean meridional circulation. As explained by Matsuno and Nakamura (1979), the Lagrangian-mean is 'an average in the zonal direction along a curved material line', in contrast with the Eulerian-mean, which is the 'standard' zonal mean. The 'material line' is a string of individual air particles moving together within the flow. This aligns with the common distinction between Lagrangian and Eulerian reference frames, where in the former case you observe a fluid parcel from within the flow itself, and in the latter case you observe the fluid from a fixed external reference point. Lagrangian-mean circulation is then a circulation measured from the Lagrangian-mean reference frame. Streamlines of the Lagrangian-mean circulation can be seen in Figure 2.4. Physically, Lagrangian-mean transport describes the motion of the centres of mass of a group of fluid parcels in the presence of eddies, and thus the transport of mass itself, and not the motion of the individual fluid parcels (Dunkerton, 1978).

The difference between the Lagrangian-mean meridional circulation and the Eulerian-mean meridional circulation is due to the Stokes drift $\overline{\mathbf{u}}^S = \overline{\mathbf{u}}^L - \overline{\mathbf{u}}^E$, where $\overline{\mathbf{u}}^E$ is the Eulerian-mean velocity field and $\overline{\mathbf{u}}^L$ is the Lagrangian-mean velocity field (Dunkerton, 1978; Andrews and McIntyre, 1978a). The Stokes drift is the velocity form of the Stokes field corrections which associate the two means. For a field $\phi(\mathbf{x}, t)$:

$$\overline{\phi}^S(\mathbf{x}, t) = \overline{\phi}^L(\mathbf{x}, t) - \overline{\phi}^E(\mathbf{x}, t)$$
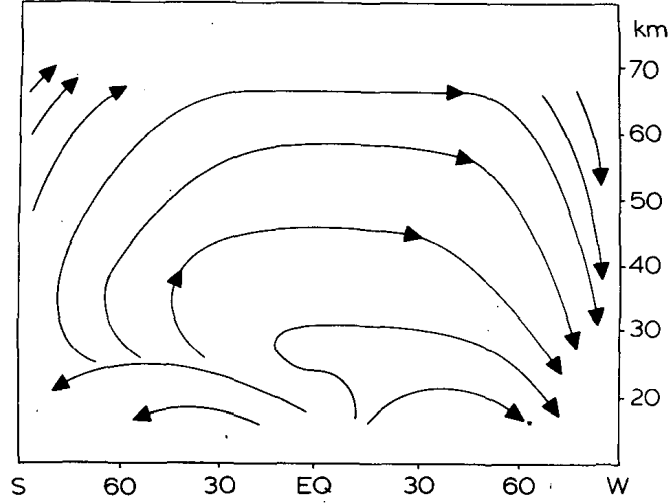
Figure 2.4: Streamlines associated with Lagrangian-mean velocities for the summer (S) and winter (W) hemispheres. (From Dunkerton, 1978, Fig. 4.)

where;

$$\overline{\phi}^{L}(\mathbf{x},t) = \overline{\phi(\mathbf{x},t)}^{L} = \overline{\phi(\mathbf{x}+\xi(\mathbf{x},t),t)}^{E} = \overline{\phi}^{E}(\mathbf{x}+\xi,t)$$

and $\xi(\mathbf{x},t)$ is a particle displacement field. Refer to Andrews and McIntyre (1978a) for further details and discussion. Dunkerton (1978) went on to show that one of the main differences between the Lagrangian and Eulerian mean meridional circulations is that the Eulerian circulation includes the 'Ferrel cell' circulation (see Fig. 2.5). The Ferrel cell has no effect on mass transport, as it is wave-induced and exists to oppose the Stokes drift in order to maintain thermal wind balance. Figure 2.5 therefore confirms the earlier physical description that meridional mass transport is primarily controlled by the Lagrangian-mean circulation. Figure 2.5 also illustrates that the stratospheric single-cell Lagrangian system (left) and two-cell Eulerian system (right) both exist above a separate two-cell system in the lower stratosphere.

As a Lagrangian system, the BDC cannot be seen directly in Eulerian diagnostics such as meridional velocity v; however, by transforming the Eulerian-mean equations according to Andrews and McIntyre (1976, 1978b), the contributions of mean and eddy transports can be combined into a 'residual-mean' circulation (Butchart, 2014), which can then be used as a proxy for the Lagrangian-mean transport (Seviour et al., 2012).

The BDC at first glance sounds like it may have great importance in seasonal

28
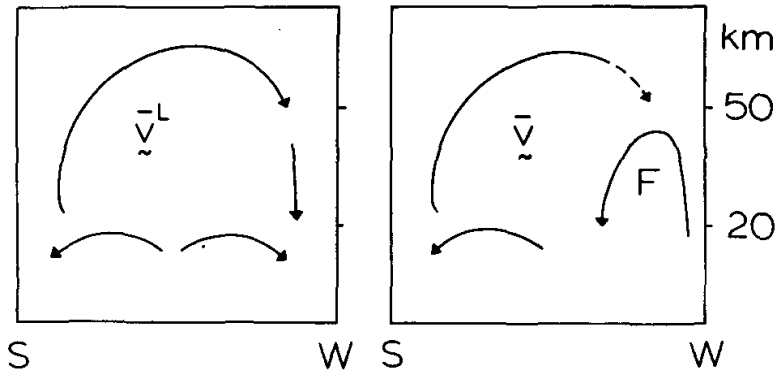
Figure 2.5: Distinction between Lagrangian (left) and Eulerian (right) mean meridional circulations at the solstices (S: Summer; W: Winter). The Eulerian circulation includes a wave-induced Ferrel cell (F). (From Dunkerton, 1978, Fig. 6.)

mass transport within the stratosphere; however, Dunkerton (1978) showed that parcels of air moving into the tropical stratosphere take approximately two years to reach polar latitudes. While this may therefore suggest that the BDC is too slow to be related to the mass movements that are studied in this investigation, this is referring to two years to travel a distance of the order of 10,000 km. Here, the distances in question are of the order of 100 km (approximately one degree of latitude), and the equivalent time for that distance is around one day. Based on Baldwin and Dunkerton (2001), the timeframe for such events is that they occur and dissipate within 60 days, so it should be possible to gauge how the strength of the residual-mean circulation changes during the event's 60-day progression.

2.4 Empirical Orthogonal Functions

Empirical orthogonal functions are used to decompose a space-time field into its space and time components (Hannachi et al., 2007). The space components form an orthogonal set of spatial patterns (hence EOF), while the time components are a set of uncorrelated time series known as the principal components (PCs); indeed, EOF analysis is closely related to Principal Component Analysis (PCA) (Hannachi et al., 2006). The principal components are uncorrelated linear combinations of the variables of the field that have maximum variance; the first principal component has the largest variance, the second has the next largest, and so on (Hannachi et al., 2006). EOF analysis can be used to determine the key modes of variability in dif-

ferent atmospheric fields, such as surface temperature, sea level pressure, and zonal and meridional components of wind speed. For example, Wallace et al. (1993) used EOFs to represent the QBO. The NAM itself is now defined to be the leading EOF of geopotential height, and thus is considered the main indicator of stratospheric variability in the Northern Hemisphere. Similarly, the SAM is the dominant factor in dynamic variability in the Southern Hemisphere (Baldwin and Thompson, 2009).

The EOFs themselves are the solution to the eigenvalue problem

$$S\mathbf{u} = \lambda\mathbf{u},$$

with the kth eigenvector of S being the kth EOF (Hannachi et al., 2007). S is the $p \times p$ sample covariance matrix of the $n \times p$ data anomaly field X, with n timesteps and p grid points, such that

$$S = \frac{1}{n}X^TX,$$

The eigenvalue λ_k gives a measure of the variance accounted for in the direction of the eigenvector $\mathbf{u}_k = (u_{k1}, u_{k2}, \ldots, u_{kp})^T$, where the $\mathbf{u}_k$ are chosen such to be orthonormal, $\mathbf{u}_i^T\mathbf{u}_j = 1$ if $i = j$, and 0 otherwise.

The PC of the kth EOF is the projection of X onto that EOF,

$$\mathbf{a}_k = X\mathbf{u}_k$$

with $\mathbf{a}_k = (a_{1k}, a_{2k}, \ldots, a_{nk})^T$. (Hannachi et al., 2007)

The EOFs and PCs can also be obtained using singular value decomposition $X = A\Lambda U^T$, or $XU = A\Lambda$, where A and U^T are $n \times r$ and $r \times p$ unitary matrices respectively, where $r \leq \min(n,p)$ is the rank of X, and A and U have columns $\mathbf{a}_k$ and $\mathbf{u}_k$. Λ is an $r \times r$ diagonal matrix with elements $\sqrt{\lambda_k}$.

Baldwin et al. (2009) reviewed spatial weighting for EOFs, which is a process designed, among other things, to desensitise the resulting spatial patterns from the grid used in the original data. On a latitude-longitude grid, the weighting matrix W compensates for latitude ϕ by multiplying by $\cos(\phi)$. W is a symmetric $p \times p$

matrix, such that

$$\mathbf{x}^T W \mathbf{x} = \mathbf{x}'^T \mathbf{x}'$$

where $\mathbf{x}' = W^{\frac{1}{2}} \mathbf{x}$. Here, W has the same dimensions as S to allow for off-diagonal elements which can vary the weighting across the covariance matrix. The mapping $\mathbf{x} \to \mathbf{x}'$ transforms the equation to Euclidean space, where the weighting is uniform. Transforming the data matrix X to Euclidean space for $\mathbf{x} \in X$ gives $X' = XW^{\frac{1}{2}}$, with the covariance matrix

$$S' = (W^{\frac{1}{2}})^T S W^{\frac{1}{2}}.$$

Then $S'\mathbf{u}' = \lambda \mathbf{u}'$ and the EOFs are gained by the inverse transformation $\mathbf{u} = W^{-\frac{1}{2}} \mathbf{u}'$.

The NAM is defined as the leading EOF of geopotential height, but there is no one method for even how this single definition of the NAM is acquired. Baldwin et al. (2009) used the weighting matrix W to resolve the EOF iteratively; more information on this can be found in Appendix F. Baldwin and Thompson (2009) presented a number of alternatives for X, including the monthly-mean geopotential height at 1000 hPa, Z_{1000}^m, from which a daily NAM index can be constructed for each level l by regressing Z_{1000}^m at l onto the leading PC time series index, and then projecting daily-mean geopotential height data onto the corresponding regression map. However, as the authors mentioned, this definition does not capture stratospheric variability, due to being based on 1000 hPa. The second definition they covered uses monthly-mean geopotential height Z_l^m at all available pressure levels l, but this is much more computationally expensive. Their third, and preferred, method uses daily-mean zonally averaged geopotential height at each pressure level, $[Z_l^d]$.

2.5 Climate Modelling

Chemistry-climate models (CCMs) are climate models which include parameters that respond to atmospheric chemistry, such as ozone trends and methane. In order to simulate these in the stratosphere, they need an increased vertical resolution and a model top positioned above the stratopause. These models also have more sophisticated parameterisations of stratospheric processes, such as gravity waves,

than many other climate models (Gerber et al., 2010). While they started out as models designed to explore atmospheric chemistry, these are also the models with the best stratospheric resolution. Using an ensemble of CCMs, Gerber et al. (2010) and Butchart et al. (2011) assessed the abilities of the models to reproduce observed stratospheric processes, with the 2010 paper focusing on annular modes and extratropical atmosphere, and the 2011 paper investigating polar stratospheric variability and the overall performance of the ensemble models. Both papers build on the Chemistry-Climate Model Validation activity (CCMVal) of the World Climate Research Programme's (WCRP) SPARC project (Stratosphere-troposphere Processes and their Role in Climate) (Eyring et al., 2005).

Using EOF analysis, Gerber et al. (2010) showed that the NAM characterises over three-quarters of the variance of zonally-averaged flow in both reanalysis and the models, but that the CCMs overestimate the significance of the annular modes (the first EOF) by up to 10% at the expense of the second EOF. This means that the models attribute more of the variance to the annular mode than reanalysis would suggest was appropriate. They suggested that this may be due to the models not accurately distinguishing the asymmetry between the Northern and Southern Hemispheres. The models used were from CCMVal Phase 2, with three from CMIP3 (Coupled Model Intercomparison Project, Phase 3) that had stratospheric data. Comparing these, they found that the CCMs evaluated the amplitude of the annular modes more accurately than the CMIP3 models. However, there are a number of common biases that they identified in the models, including the annular mode pattern being extended too far towards the equator. Notably, they discovered that the models with least bias have higher horizontal resolution, and suggested this may be due to them simulating eddy-mean flow interactions more accurately. Butchart et al. (2011) also identified a number of systematic biases in the models, and suggested that the models had poorer performance in the Southern Hemisphere.

Butchart et al. (2011) investigated the effectiveness of the CCMVal-2 models to evaluate different aspects of stratospheric circulation. They investigated the polar night jet (PNJ), which the models simulated well in the Northern Hemisphere, but

'not quite so well' in the south, where most models do not reproduce the observed tilt in the upper stratosphere of the jet towards the equator. Comparing the EOFs of extratropical zonal mean zonal wind at 50 hPa from both the model data and the reanalysis data from ERA-40, they found that the leading mode accounted for the majority of the variance, with the reanalysis data's Northern Hemisphere variability explained to 87%. The leading mode in the models explains a similar amount of variability. In the Southern Hemisphere, extratropical variability of zonal mean zonal wind in the stratosphere is explained by the first two modes of the EOF analysis, which the paper distinguishes to be the strength of the PNJ (59%) and its meridional shift (35%), respectively, accounting for 94% of the total variance. However, the model data is biased too much towards the leading mode compared to the reanalysis, and does not account enough for the meridional shift.

Simpson et al. (2011) took a closer look at the bias produced by General Circulation Models (GCMs) in the Southern Hemisphere using the Canadian Middle Atmosphere Model (CMAM), which has a model top at 100 km, but does not include the interactive chemistry found in CCMs. They investigated the stratospheric processes in the model which caused the bias, and noted the Southern Annular Mode (SAM) has a persistence which is not replicated in the north. Butchart et al. (2011) observed that the breakdown of the austral polar vortex occurs too late in the year, extending the influence of tropospheric systems on the stratosphere into early summer. Simpson et al. (2011) confirmed and attributed the majority of the persistence to tropospheric processes, such as the position of the jet streams. They concluded with the statement that models are likely to overestimate the magnitude of a poleward shift of the jet in scenarios of future climate change due to their bias in the response of the SAM, but that removing bias in tropospheric feedbacks may help reduce the bias in stratospheric processes.

Hitchcock and Simpson (2014) used the same model to investigate S-T coupling, focusing on three main issues: downward influence of zonal-mean stratospheric variability on the troposphere; separation of deterministic tropospheric signal from variability; and zonally asymmetric tropospheric response. When considering downward

influence, it is important to be able to differentiate between the effects of the upward-propagating waves that cause the SSW, which will also interact with tropospheric flow directly, and any influence from the SSWs on the troposphere, as shown in Section 2.2 with reference to Gerber et al. (2009). Because studies often use symmetric NAM and/or zonal mean responses, the zonal asymmetry of the troposphere is not often represented. However, despite the zonal symmetry of the stratospheric perturbation, Hitchcock and Simpson (2014) found a zonally asymmetric response similar to that shown in ERA-interim and the free-running CMAM simulation in simulations spun off from a December control. They concluded by stating that a model which does not properly capture the structure of the stratospheric circulation during and following an SSW cannot be expected to capture the tropospheric response.

2.6 Consistency between Models and Reanalysis

The accuracy to which climate models are able to replicate stratospheric variability, both between different models and when compared to ERA-40 and ERA-interim reanalysis data, was investigated by Woollings et al. (2010) and Osprey et al. (2013), among many others. ERA-40 is a 40-year reanalysis dataset from the European Centre for Medium-Range Weather Forecasts, for 1957–2002. ERA-interim covers 1979 onwards to the present, and is continually updated. Osprey et al. (2013) compared two configurations of the same climate model, Had-GEM2, where one had a model lid at 39 km and the other had a model lid at 84 km, with ERA-40 and ERA-interim data. Woollings et al. (2010) compared HadGAM, which has a well-resolved stratosphere, with ERA-40 data to investigate links between variability in the stratosphere and blocking systems in the troposphere. A blocking system is a large-scale anticyclone which 'blocks' the prevailing westerlies and mid-latitude storms, causing low pressure systems to be diverted polewards around the high pressure system (Pelly and Hoskins, 2003). Similar in concept to how SSWs are generated, Woollings et al. (2010) stated that the onset of a blocking event is associated with the breaking of a synoptic-scale Rossby wave, this time however in the upper troposphere rather than

the stratosphere. As with the NAM, there are a number of different criteria used to generate a 'blocking index' from which to define a blocking event, with Woollings et al. (2010) basing their definition on the breaking Rossby wave by looking for a reversal in the meridional gradient of potential temperature on the tropopause. (The tropopause used in this instance is the dynamic tropopause, which is based on PV rather than lapse rate.)

Osprey et al. (2013) used the forcing conditions as outlined for the Coupled Model Intercomparison Project Phase 5 (CMIP5), which can be found in Jones et al. (2011), and a modified version of the ozone dataset from SPARC, as inputs to their ensemble runs. There are many similarities between the models and ERA-40, including the general trend of stratospheric global cooling, and the high-top model's ability to simulate the 'final warming' of the polar vortex. In this paper, they defined the 'final warming' to be the last time over the winter period when zonal-mean zonal wind (at 60° and 10 hPa) becomes easterly. There was, however, considerable bias in many of the simulations. For example, the models exhibited a bias towards lower temperatures in the troposphere and higher temperatures in the stratosphere compared to the reanalysis data. In most instances, this bias was substantially reduced in the high-top ensemble runs. Also lacking from the low-top ensemble was the existence of some aspects of stratospheric circulation, including the QBO. It was clear that the model with higher vertical resolution was beneficial in modelling and understanding stratospheric processes.

Woollings et al. (2010) found that their model simulated tropospheric blocking and stratospheric variability reasonably well, and correlations between the GCM and ERA-40 were similar. However, the model underestimated aspects of blocking and variability in Europe and the Northern Hemisphere stratosphere; they suggested that these discrepancies were related, as the two systems are linked to each other. As suggested before by Baldwin and Dunkerton (1999) and others, tropospheric patterns, including the blocking systems, are potentially related to the downward influence of the stratosphere. Woollings et al. (2010) meanwhile said 'the influence of the stratosphere on blocking, if indeed there is one, is via the zonal mean flow'.

They also mentioned that correlations between the leading EOF and the blocking index are stronger when the stratosphere leads the blocking. They confirmed that the blocking systems themselves also affect the tropospheric planetary waves on a synoptic scale, by regionally modifying the stationary wave patterns, which in turn propagate anomalies back up into the stratosphere.

2.7 Proposed Coupling Mechanisms

The mechanisms and dynamics involved in coupling the stratosphere to other components of the earth system are not fully understood (Gerber et al., 2012; Kidston et al., 2015). Gerber et al. (2012) outlined potential future research, with a reminder that any new components in a climate model, such as adding stratospheric chemistry or nonorographic gravity waves, means a higher computational expense of running the model. They asked, 'how much of the stratosphere needs to be represented in a model to capture the influence on the troposphere?' As noted in Section 2.5, Hitchcock and Simpson (2014) conjectured that a model which does not properly capture the structure of the stratospheric circulation cannot be expected to capture the tropospheric response.

There are currently several theories about which mechanisms are most relevant for coupling the troposphere and stratosphere together, but no physical portrayal of the key process(es). As discussed in Section 2.5, Simpson et al. (2011) noted a connection between the location of tropospheric jet streams and the breakdown of the polar vortex. Gerber et al. (2012) reaffirmed this as an important factor, but one for which we do not know the key mechanism(s). They presented a number of suggestions for tropospheric response proposed in other research papers, including: a response based on stratospheric PV and wave-driven changes in meridional circulation; changes in synoptic eddies; refraction of synoptic waves; and the influence of planetary waves. Kidston et al. (2015) suggested that the latitude of tropospheric jet streams and storm tracks is influenced by the speed of the stratospheric jet streams above. Specifically, they looked at the influence of the stratospheric circumpolar jet, which marks the edge of the polar vortex, and its effects on the latitude of the

tropospheric polar jet, or mid-latitude jet. Echoing Gerber et al. (2012), they noted that the underlying dynamics of this coupling are not well understood. They recommended more investigation was needed on the dominant eddy feedback processes and the controls on wave propagation and generation.

Cohen et al. (2013) investigated the driving of parameterised and resolved gravity waves and planetary waves, and their impact on the Brewer-Dobson circulation (BDC). The resolution of climate models means that the smaller-scale waves cannot be resolved, and so these are parameterised. In atmospheric GCMs (AGCMs), these are primarily gravity waves originating from convection, frontal instabilities, and small mountains. Cohen et al. (2013) aimed to provide a better understanding of how waves of different scales contribute to the BDC. They found that when they perturbed parameterisations of orographic gravity waves, the resolved wave drag responded to compensate, resulting in little change to the total wave driving. Because of this, they suggested that the common decomposition of the BDC into linear wave-driven components (resolved and parameterised) using the principle of downward control (Haynes et al., 1991) may lead to an inaccurate representation of meridional circulation; if one component is altered, and the others compensate for the change, it would be hard to tell how each component contributes to the whole system.

A number of mechanisms for explaining the stratospheric influence on the troposphere were also reviewed by Song and Robinson (2004): reflection of the planetary waves propagating vertically from the troposphere to the stratosphere; interaction between planetary waves and the stratospheric zonal flow; responses to changes in stratospheric PV; wave-driven secondary circulations of PV in equilibrium (the so-called 'downward control' idea); and amplification of the intrinsic annular modes.

While potential vorticity (PV) is itself not a 'coupling mechanism', measuring the *changes* in stratospheric PV is one of the common themes throughout the different proposed mechanisms. Hartley et al. (1998) found that alterations in stratospheric PV, associated with distortions in the polar vortex and caused by upward-propagating tropospheric waves or stratospheric waves travelling east-

ward, induce perturbations in the geopotential height field in the upper troposphere. Using quasi-geostrophic piecewise PV inversion, they calculated the PV contribution to the geopotential height anomaly, and found that 15–34% of the anomaly at the tropopause could be attributed to stratospheric PV anomalies. This suggests that changes in the stratospheric PV field can significantly affect the height of the tropopause (Song and Robinson, 2004). This is explained further by Ambaum and Hoskins (2002), who showed that a positive potential vorticity anomaly in the polar stratosphere from a strong polar vortex results in the polar tropopause rising. This in turn leads to a low pressure signal over the North Pole. Black (2002) also considered this approach, showing that large scale PV anomalies induce zonal wind perturbations which extend right down to the surface. Black (2002) additionally brought up the issue of causality, stating that the interpretation of downward influence mechanisms must depend on the processes that are responsible for causing the initial stratospheric anomalies. Upward-propagating Rossby waves are one factor, but there are also local radiative processes within the stratosphere that need to be considered. This strengthens the recommendation, also echoed by Hartley et al. (1998), that atmospheric models must represent stratospheric processes sufficiently to properly simulate tropospheric feedback.

Another set of proposed mechanisms centres on the influence of planetary-scale Rossby waves. It is already known (see Section 2.2) that upward-propagating Rossby waves affect stratospheric circulation, but Perlwitz and Harnik (2003) investigated the suggestion (also proposed previously by others) that some of these waves would be reflected, thus propagating back downwards and affecting tropospheric circulation. The reflection occurs when the polar night jet peaks in the high latitude mid-stratosphere, combined with a 'meridional waveguide' which channels the reflected wave to the troposphere. With a lag of about six days, they found a relationship between stratospheric zonal wave 1 and tropospheric zonal wave 1 when the reflecting surface exists.

In addition to reflection of planetary waves, refraction of waves may also be a contributing factor. While refraction is considered more an upward component, this

appears to be influenced by lower stratospheric conditions. This was introduced by Limpasuvan and Hartmann (2000), who were investigating zonal wind associated with the annular modes, which are forced by eddy fluxes. An anomalous zonal wind field can result in an anomalous stationary wave response, implying an anomalous eddy momentum forcing. The propagation of the eddies was then investigated, and a relationship found with refraction of the stationary waves. During the positive NAM phase, waves are less strongly refracted towards the pole, resulting in equatorward wave propagation and poleward eddy momentum flux. In the opposite phase, stationary waves are more strongly refracted toward the pole, resulting in an anomalous equatorward eddy momentum flux. They drew the comparison here between an increase in poleward waves from refraction, and a weak polar vortex, since the vortex is weakened by an increase in upward-propagating waves in the polar region. The refraction of Rossby waves is explained in the investigation by Ambaum and Hoskins (2002) of the varying height of the tropopause as a result of PV anomalies. An increase in the NAO index over Iceland results in a positive PV anomaly in the troposphere, lowering the tropopause in that region. This causes upward-propagating Rossby waves to be refracted towards the equator, reducing the number that break at the edge of the polar vortex. This then leads to a stronger polar vortex and a second positive PV anomaly in the stratosphere, following a lag time of about four days. An illustration can be seen in Figure 2.6 (Ambaum and Hoskins, 2002).

Refraction of EP flux, resulting in a change in eddy momentum flux, is also considered by Simpson et al. (2009), who looked at influence of thermal perturbations in the stratosphere on tropospheric circulations. They noted that a change in the vertical temperature gradient affected the meridional PV gradient, which changes the refractive index influencing the direction of propagation of the eddies. Kushner and Polvani (2004) also looked at the role of eddies, and found that a stratospheric thermal perturbation with eddy feedbacks resulted in a response that penetrates down to the mid-troposphere, while a perturbation without eddy feedbacks induces a response that is confined to the troposphere. Additionally, they found that as the
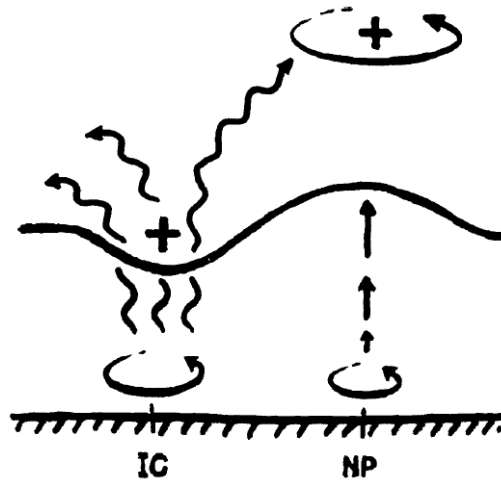
Figure 2.6: The tropopause (thick line) descends due to a positive PV anomaly (+) over Iceland (IC). Upward-propagating Rossby waves (wavy lines) refract more toward the equator. A stronger polar vortex and associated positive PV anomaly (+) cause the tropopause below to rise, which stretches the tropospheric column (vertical arrows) over the North Pole (NP). (From Ambaum and Hoskins, 2002, Fig. 1.)

winter polar stratosphere is cooled, the polar vortex strengthens, the eddy driving is reduced, and the tropospheric jet moves poleward. They questioned the issue of causality, as from their diagnosis using EP flux analysis, it is not possible to see which result is the cause and which is the effect. They concluded that the full response cannot be predicted without a theory for baroclinic eddies, and end with a rather poignant statement; '[the] stratosphere and troposphere could be coupled in ways that might be rather difficult to untangle.'

Song and Robinson (2004) combined a number of these approaches with the 'downward control' principle of Haynes et al. (1991), which involves wave transport of PV being in equilibrium with its creation and destruction, to create the hypothesis of 'downward control with eddy feedback'. This involves tropospheric eddy reinforcement of a weak stratospheric signal transmitted downwards by the secondary circulation associated with 'downward control'. Tested using a model of their own devising, in which they applied a zonally-symmetric torque to the stratosphere of an idealised GCM, the study found a robust response in the troposphere that projects on the annular modes of the model. However, when planetary waves are suppressed, the model did not produce the same result. This implies that while their 'downward control with eddy feedback' can explain part of the downward influence, it does not give the whole picture.

2.8 Review

Research into stratosphere-troposphere coupling has progressed from qualitatively identifying links between the two layers of the atmosphere, to quantitatively investigating the magnitudes and extent of these links and how they can be used to improve the skill of forecasting. Climate models are starting to include more stratospheric processes, and investigation is ongoing into which aspects of stratospheric dynamics can be resolved and need to be parameterised. The field is now moving into increasing understanding of the mechanisms and dynamics involved in stratosphere-troposphere coupling. This will help determine which aspects of the stratosphere need to be represented in a model to identify coupling with the troposphere, with potential vorticity, planetary wave propagation, and synoptic eddies being the prime candidates.

3 Introduction to tropospheric amplification

3.1 Introduction

As mentioned in Section 2.2, breaking waves produce westward drag, and air is directed polewards by the Coriolis force, driving a meridional circulation. It follows that an influx of mass over the 'polar cap' from a stronger-than-normal meridional circulation would cause an increase in pressure in the column of air below, as the recorded pressure at a certain level is a measure of the total atmospheric mass above that level. The polar cap is defined as the area polewards of 65° in either hemisphere, per Baldwin and Thompson (2009). Figure 3.1 illustrates four original theories for how this pressure increase could develop between the injection of mass at around 15 km, and the surface. If the polar cap had a rigid vertical boundary at 65° extending upwards from the surface, through which air could not flow, this pressure increase would be uniform to the surface (Fig. 3.1a). However, the boundary of the polar cap is not rigid, and so the pressure increase is expected to tail off as the extra mass leaks out, either entirely within the stratosphere (Fig. 3.1b), or by the time it reaches the surface (Fig. 3.1c). Reanalysis data shows that neither of these are the case; instead, there is a reduction in the increased pressure down to the tropopause, implying the added mass leaking out of the polar cap. Below this, the pressure increases further, even beyond the initial increase caused by the Rossby wave pump, suggesting a further poleward flow of mass in the troposphere (Fig. 3.1d). This is a *tropospheric amplification* of the stratospheric pressure signal.

If δz is the difference in height between two vertical layers z and $z + \delta z$, the mass of air between those layers is $\rho \, \delta z$ for some air density ρ at height z. The difference in pressure between the layers is $-\delta p$. The downward force of gravity g on the mass of air is $g\rho\delta z$, which is balanced by the pressure gradient force, leading to the hydrostatic assumption

$$\frac{\partial p}{\partial z} = -\rho g \ .$$

By focusing on tropospheric amplification and its related effects, it is hoped that an increased understanding of S-T coupling is achieved. This thesis approaches the problem from a new angle – that being the consideration of mass movement, and to a lesser extent, change in pressure – using vertical height as the altitude measure. The data fields used are raw quantities that are readily available from observational data, reanalysis, and climate models, and as such, they do not require extensive calculation and analysis before they can be considered useful.

Geopotential height Z is a vertical height metric that is proportional to the geopotential Φ of a unit mass at that height, relative to sea level,

$$Z = \frac{\Phi}{g_0},$$

where $g_0 = 9.81$ is globally-averaged gravitational acceleration at the surface. Geopotential itself is the potential energy of the unit mass, defined as the energy required to lift a mass of 1 kg from sea level to a particular height h,

$$\Phi(h) = \int_0^h g \, dz \, .$$

z is the geometric height coordinate, and g is non-averaged gravitational acceleration. Taking the assumption $g \approx g_0$, geopotential height Z is essentially interchangeable with geometric height z.

Another important relationship that will be further investigated in this chapter is that between pressure p and temperature T, which are related through potential temperature θ. Potential temperature describes the temperature that a parcel of dry air would have if moved adiabatically to a standard reference pressure, $p_0 = 1000$ hPa:

$$\theta = T \left(\frac{p_0}{p} \right)^{\kappa},$$

where $\kappa = \frac{R_d}{c_p} = 0.286$ is the ratio of the dry air gas constant R_d to its specific heat capacity c_p. By definition therefore, any adiabatic air movement conserves potential temperature.

Previous research, such as Song and Robinson (2004), has qualitatively investi-

gated the downward influence of the stratosphere on the troposphere. One of their observations, based on work by Hartmann et al. (2000), is that 'the stratospherically forced response is both amplified and modified by tropospheric dynamics', with the direct tropospheric response to an initial stratospheric forcing being amplified and maintained by feedbacks from transient eddies. The baroclinic eddies shift depending on the position of the tropospheric jet, and this results in anomalous fluxes in momentum. However, none of these forces, fluxes or feedbacks are quantified, meaning there is no way to measure the response.

In this thesis, a quantitative approach is developed for a tropospheric response to a measured increase in stratospheric pressure. It should be noted that the mechanism behind this specific tropospheric response, while likely related to the mechanisms discussed in Section 2.7, is not a main focus of the thesis, but will be briefly investigated in later sections. The quantifiable measures can then be used in numerous situations, such as model intercomparisons (such as those in Section 5) and development. For example, by comparing the numerical value of a standard tropospheric amplification event, model developers would be able to use this metric to ensure that their model faithfully represents S-T coupling processes.

(a) Rigid boundary theory

(b) Stratospheric leak theory

(c) Tropspheric leak theory

(d) ERA-interim reanalysis
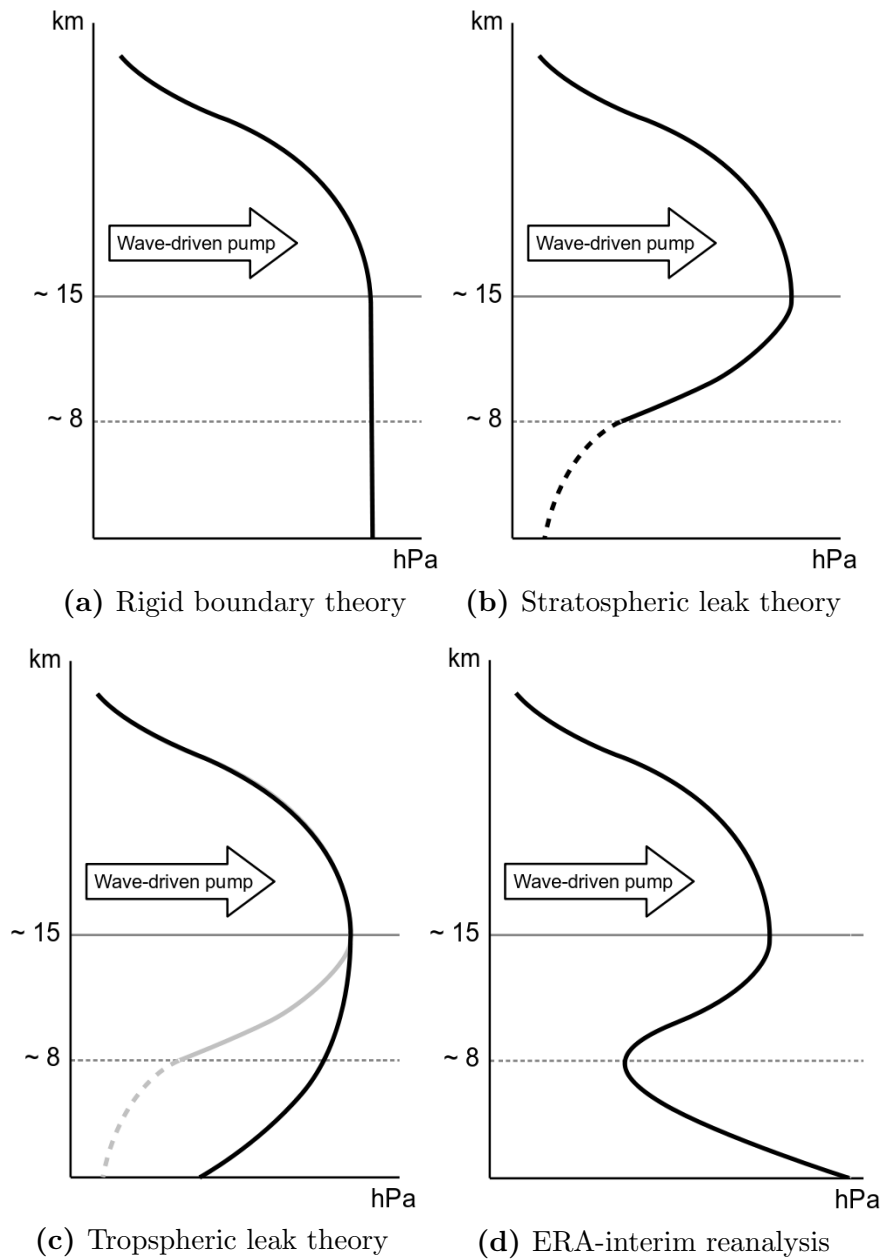
Figure 3.1: Illustration of the Rossby wave pump and associated original theories (see Sec. 3.1) concerning pressure increase over the polar cap.

3.2 Investigation

Geopotential height values from zonally-averaged ERA-interim reanalysis data were interpolated from pressure levels to produce a set of pressure data at defined heights (see Appendix C). After removing the annual cycle from the pressure field to leave the anomalies (Appendix D), and taking the zonal average, a weighted approximation to the area average for the whole of the polar cap pressure field p_{cap} was created for each height Z, with weighting h applied to compensate for the reduction in grid-box size as the data nears the pole:

$$p_{\text{cap},Z} = \frac{\sum_y [p]_{y,Z} h_y}{\sum_y h_y} \tag{1}$$

where

$$h_y = \cos \frac{\pi y}{180}$$

and $p_{y,Z}$ is pressure at latitude y (°N) and geopotential height Z (km). Full details on the construction of p_{cap}, including the zonal average and discretisation of latitude ϕ to y, can be found in Appendix E.

Given that we are looking for anomalously high (or low) pressure, a pressure value p_{cap} exceeding two standard deviations σ at a particular height Z in the stratosphere is a reasonable starting point. Thus p_{cap} is considered anomalous if $p_{\text{cap}} > 2\sigma_Z$ or $p_{\text{cap}} < -2\sigma_Z$, where

$$\sigma_Z = \sqrt{\frac{\sum_n (p_{\text{cap},Z} - \overline{p_Z})^2}{n-1}}$$

Anomalies where $p_{\text{cap}} > 2\sigma_Z$ are classed as positive anomalies, which indicates an influx of mass, while anomalies where $p_{\text{cap}} < -2\sigma_Z$ are negative anomalies, indicating an outflow of mass. p_{cap} therefore has opposite sign to the NAM index. The height Z chosen slightly affects the number of days where $p_{\text{cap}} > 2\sigma_Z$ or $p_{\text{cap}} < -2\sigma_Z$ is satisfied, but since the altitude of the Rossby wave pump itself is assumed constant, this does not have much impact on the results aside from whether or not a few days at the beginning and end of an event are included.

The altitude of 25 km was chosen for the index, as it is the approximate height of
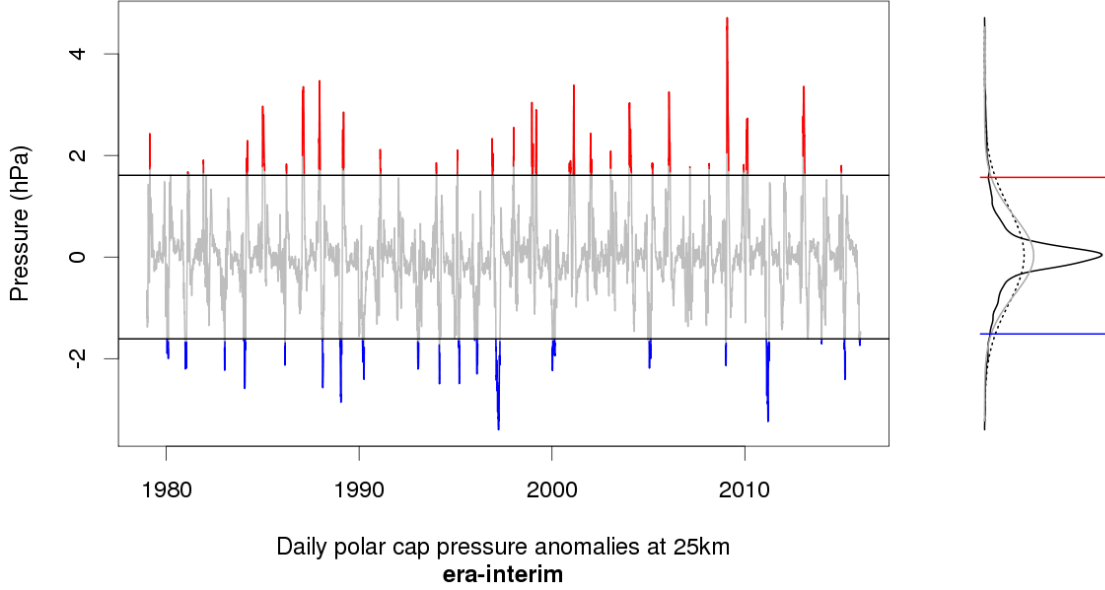
Figure 3.2: Daily polar cap pressure anomalies at 25 km $p_{\mathrm{cap},25}$, Northern Hemisphere, showing pressures above (red) and below (blue) 2 standard deviations, with pressure density distribution on the right. Solid black line is the calculated PDF of $p_{\mathrm{cap},25}$ from binned data, grey line is the estimated PDF $f(x)$, dotted line is standard Gaussian distribution N∼(0,1).

greatest EP flux divergence, most concentrated wave breaking, and the approximate height of the transition between the two-cell diabatic circulation of the lower stratosphere and the single-cell Lagrangian circulation of the upper stratosphere (Yang et al., 1990). If Z was chosen to be any higher up, the measure would be taken beyond the extent of the pump's influence, and a number of results may be missed.

Figure 3.2 shows the time series of Northern Hemisphere polar cap pressure anomalies at 25 km in ERA-interim from 1979 to 2015. The largest pressure anomalies in the Northern Hemisphere, including all those which exceed $\pm 2\sigma$ (red and blue) occur between November and April, and correspond to the different states of the polar vortex. Positive pressure anomalies correspond to weak polar vortex events, much like a negative NAM index is indicative of a weak polar vortex, and negative pressure anomalies correspond to strong polar vortex events, much like a positive NAM index is indicative of a strong polar vortex (Baldwin and Dunkerton, 2001). The probability density curve of polar cap pressure is shown on the right of Figure 3.2. The black curve was calculated by binning the data based on 'Scott's rule', where bin width $W = 3.49\sigma n^{-\frac{1}{3}}$ (Scott, 1979), and plotting the resulting density curve. The grey curve shows an estimation of the PDF using the sample mean μ

(a) Northern Hemisphere   **(b)** Southern Hemisphere
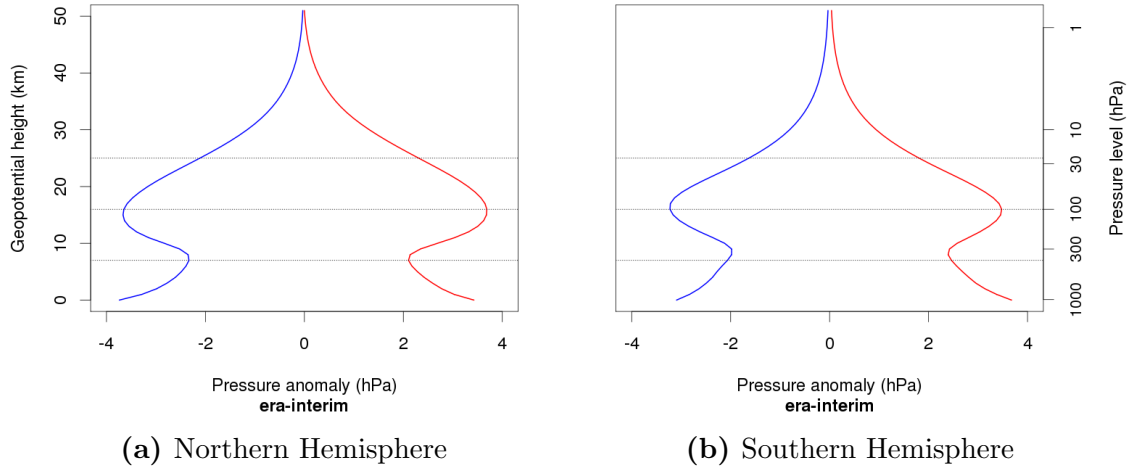
Figure 3.3: Positive (red) and negative (blue) composites of pressure anomalies over the polar cap, defined on 2 standard deviations from the mean at 25 km. Horizontal lines are at 25 km, 16 km, and 7 km.

and sample standard deviation σ of the data,

$$f(x|\mu, \sigma^2) = \frac{1}{\sqrt{2\pi\sigma^2}} e^{-\frac{(x-\mu)^2}{2\sigma^2}} \ .$$

The distribution plot shows that the polar cap pressure is mostly symmetrical, with no skew towards either a positive or negative anomaly situation, although the positive tail could suggest that extreme positive events have a larger magnitude than extreme negative events. The low sample size and near-symmetric distribution however imply this is more likely to be an anomaly that would be smoothed out with more data. The sample distribution is also very similar to the standard Normal distribution superimposed on the plot (dotted), with the most notable difference being a slightly narrower bell deriving from a smaller standard deviation, $\sigma = 0.8048$.

Each of the events shown in red and blue in Figure 3.2 can be combined into one composite plot showing average pressure deviation from the mean during a tropospheric amplification,

$$\overline{p_{\mathrm{cap},Z}} = \frac{\sum_n p_{\mathrm{cap},Z} \mid p_{\mathrm{cap},25} > 2\sigma_{25}}{n_{p_{\mathrm{cap}}} \mid p_{\mathrm{cap},25} > 2\sigma_{25}}$$

plotted against geopotential height (Fig. 3.3a). As mentioned in Section 3.1, it would be expected that the signal above and below the peak pressure would decrease

the further it propagates. Based on Figure 3.3, the chosen altitude of 25 km is approximately 9 km above the maximum flux altitude of the Rossby wave pump, meaning the anomaly is detected at the periphery of the upward extent of the pump's influence. The maximal pressure deviation, of just under 4 hPa, occurs between 15–18 km, implying that this is the height at which the Rossby wave pump is moving mass into the polar cap region. The value is lower (at just over 2 hPa) in the region of 7 km, which is the average polar tropopause height, suggesting that the total mass flux above this height has reduced, which agrees with the expectation. The anomalous increase in pressure also trails off upwards towards 50 km, as expected, with pressure at 50 km itself having hardly any deviation from the mean. However, below the tropopause height, the deviation from the mean increases again, and it is clear more mass enters the polar cap nearer to the surface, where the pressure anomaly is again between 3 and 4 hPa. This is the tropospheric amplification of the stratospheric signal which can be seen at 16 km. As mentioned above, the altitude of the Rossby wave pump itself is assumed constant, so the resulting tropospheric amplification is invariant under the choice of height level Z.

The positive and negative composites are remarkably symmetrical; the amplitude of the anomaly caused by mass leaving the polar cap (blue curve in Fig. 3.3a) is almost identical to the amplitude caused by mass moving into the polar cap (red curve in Fig. 3.3a), despite the fact that there are only two-thirds the number of negative events as positive events being composited (Fig. 3.2, 28 positive (red) peaks as opposed to 18 negative (blue) peaks). It will be shown later (Figs. 3.7a and 3.7b) that the onset and development of positive and negative events differs.

A similar plot can be created using the values for the Southern Hemisphere in ERA-interim. Based on $\pm 2\sigma$ at 25 km, anomalous pressure events in this hemisphere occur primarily between August and November. This is later than the normal winter period but nevertheless coincides with the existence of the austral polar vortex, and is consistent with the literature which states that there is a delay in the breakdown of the vortex as a result of stratospheric cooling caused by the Antarctic ozone hole (Sun et al., 2014; Stolarski et al., 2006). Figure 3.3b of the Southern Hemisphere

anomalies is very similar to Figure 3.3a of the Northern Hemisphere, with similar amplitude, showing that the tropospheric amplification phenomenon is generic in both hemispheres. Given the large differences in topography and orography between the hemispheres, this suggests that the phenomenon is not dependent on land surface features. This appears to counter the result seen in Section 2.2 from Kidston et al. (2015), which suggested that the downward influence of the stratosphere is stronger in the Southern Hemisphere.

As mentioned above, the peak pressure anomaly occurs at around 16 km, which is approximately 100 hPa, suggesting that this is the level of highest wave activity. 100 hPa is therefore likely to be a very important index level, as it could potentially be used as a proxy measure for S-T interactions (see Section 4.3 for further investigation), without the need to go as far into the stratosphere as 25 km. Comparisons between 25 km (the height of most concentrated wave breaking), 16 km (greatest mass movement), 7 km (tropopause) and the surface (amplification) could together form a quantifiable result that directly measures the intensity of S-T coupling at a particular time, with the theory in this section used as a basis for that measure.

3.3   Annular Modes

Song and Robinson (2004) found that the tropospheric annular mode is influenced by variations in the strength of the stratospheric polar vortex. Figure 2.2 (Fig. 1 of Baldwin and Dunkerton, 2001) shows the time-height development of the NAM during the winter of 1998–1999 from data based on NCEP-NCAR. Here, the annular mode is calculated from ERA-interim (see Appendix F), and the Baldwin and Dunkerton (2001) plot is recreated in Figure 3.4. At the 20 hPa level, which is just above 25 km, 74% of Northern Hemisphere variance is accounted for by the first EOF (EOF-1), with another 11% from the second EOF (EOF-2). This is slightly lower in the Southern Hemisphere, with 64% of the variance being accounted for by EOF-1 and 15% from EOF-2. At 100 hPa, the variance is weighted more towards the second EOF, with 56% from EOF-1 and 20% from EOF-2 in the Northern Hemisphere, and 57% from EOF-1 and 18% from EOF-2 in the Southern Hemisphere.
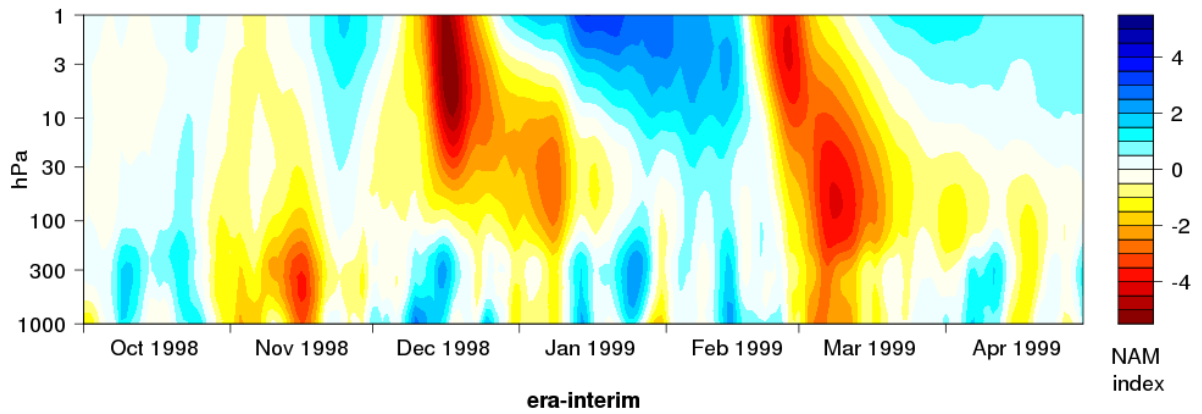
Figure 3.4: Northern Annular Mode, winter 1998–1999, with positive values (strong polar vortex) in blue, and negative values (weak polar vortex) in red.
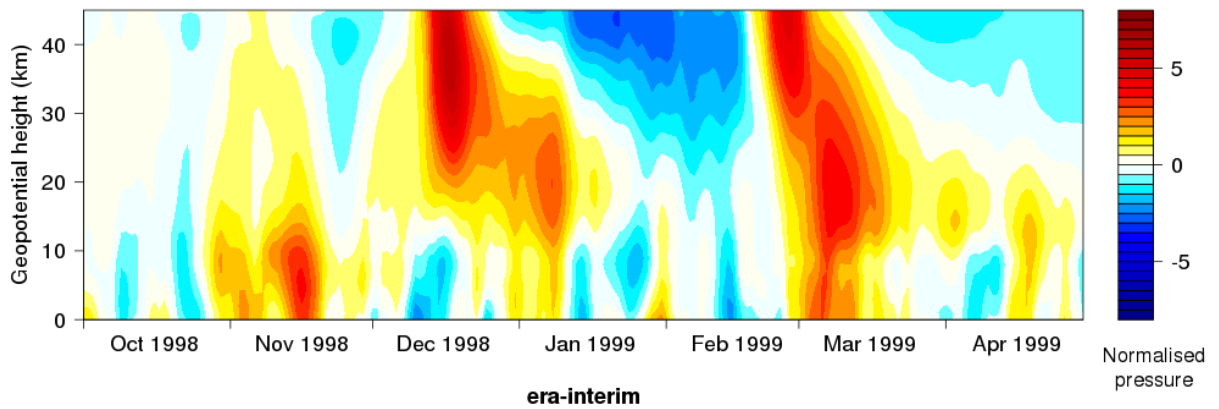
Figure 3.5: Polar cap pressure anomalies, boreal winter 1998–1999, normalised by standard deviation, with negative values (strong polar vortex) in blue, and positive values (weak polar vortex) in red.
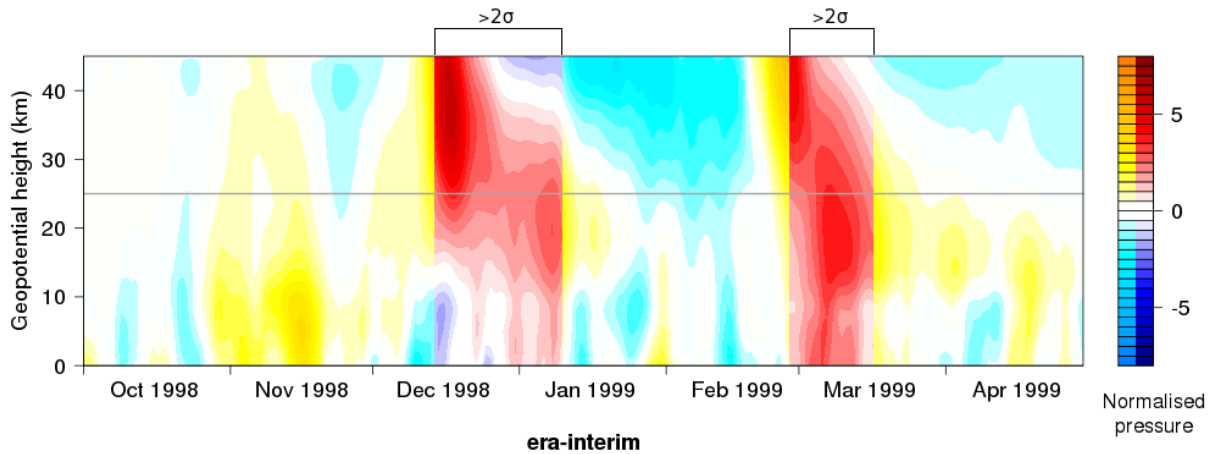
Figure 3.6: As Fig. 3.5, with periods when $p_{25} > 2\sigma$ highlighted in red.

Figure 3.4 can then be compared with a plot of the time-height development of polar cap pressure anomalies, shown in Figure 3.5. The anomalies here are normalised by dividing by the standard deviation of the pressure time series at each height, in order to account for the lower atmospheric pressure at higher altitudes.

It can be noted that the NAM (Fig. 3.4) and normalised pressure anomalies (Fig. 3.5) are very similar. This is of course to be expected, as the root definition of the NAM is from an EOF of geopotential height on pressure surfaces, while the tropospheric amplification is based on pressure anomalies defined on geopotential height levels. However, the pressure averages are easier to physically understand, in terms of mass over the polar region.

Two high amplitude events at 25 km are illustrated in Figure 3.6 – it is apparent in the Feb/Mar event that there is an increase in tropospheric pressure concurrent with the increase in stratospheric pressure, but the Dec/Jan event does not exhibit significant tropospheric amplification until the last few days of the event. This suggests that tropospheric amplification doesn't occur uniformly during *every* high pressure event in the lower stratosphere, which may be an indication that different stratospheric mechanisms (Sec. 2.7) are involved during Dec/Jan to those in Feb/Mar. Both of these events appear to occur within 10–20 days of an increase in pressure in the mid-upper stratosphere, but due to the data being normalised, this feature is likely exaggerated, as the total mass of air in the upper stratosphere is very low.

3.4 Time development of tropospheric amplification

To see the general effects of amplification events, composites of 27 events when $p_{\mathrm{cap},25} > 2\sigma$ (Fig. 3.7a) and 21 events when $p_{\mathrm{cap},25} < -2\sigma$ (Fig. 3.7b) were created from the full ERA-interim dataset. An event is considered separate from a previous one if there are more than 60 days between instances when the value of $p_{\mathrm{cap},25}$ exceeds $\pm 2\sigma$, to give time for the atmosphere to return to a quiescent state, based on the time frame presented by Baldwin and Dunkerton (2001). Events occurring within 60 days of either end of the ERA-interim time period are ignored, as their full onset

and extent may not be included.

Figure 3.7a indicates that on average the positive pressure anomalies persist for at least 30 days, reducing in intensity up to around 50 days, and that the tropospheric amplification of the stratospheric event occurs almost instantaneously. The largest pressure change occurs at 15–18 km, as seen previously in Figure 3.3a. Based on $p_{\text{cap},25}$ exceeding $+2\sigma$, there appears to be an onset period of approximately 10 days in the stratosphere which does not appear to propagate all the way down to the surface. This is similar to the onset period of an SSW, but due to the difference in how SSWs and these pressure anomalies are defined, this method picks up more events.

Figure 3.7b suggests that on average the negative pressure anomalies also persist for up to 50 days, but the tropospheric amplification effect—while still initially occurring instantaneously—does not seem to persist beyond 40 days, and after about 30 days, no longer has an upper-troposphere signal. Additionally, negative events do not have a fast onset period; rather, $p_{\text{cap},25}$ exceeds -2σ approximately in the middle of an anomalously negative period, which began up to 40 days before crossing the 2σ threshold. This agrees with the existing literature, as there is no such thing as a 'sudden stratospheric cooling'. The differences between this and Figure 3.7a imply that the processes that lead to negative events are mechanically different from those that lead to positive events, which is counter to the implication seen in Section 3.2 from Figure 3.3. Taking these together, this could mean that there are similar underlying processes to positive and negative events, but different causes for each.

Figure 3.8 is the normalised version of 3.7 (like Fig. 3.5), which provides an indication of relative mass movement rather than absolute mass movement. This can be directly compared with an equivalent composite of events defined from the NAM, as in Figure 3.9. It should be noted that if an 'event' is defined here using the 10 hPa annular mode crossing -3 and $+1.5$ respectively, as in Baldwin and Dunkerton (2001), then Figure 2.3 (their Fig. 2) can be recreated (not shown). Here instead, a similar definition to that of the $p_{\text{cap},25}$-based 'event' was used: 25 'weak vortex' events from when the 20 hPa annular mode value crosses -2σ (Fig. 3.9a),
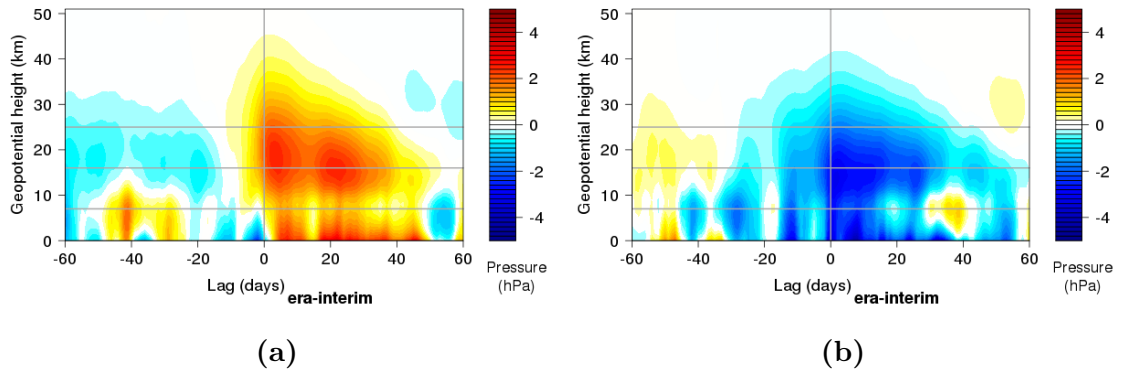
Figure 3.7: Composite of time-height development of **(a)** 27 positive polar cap pressure anomalies; **(b)** 21 negative polar cap pressure anomalies, Northern Hemisphere.
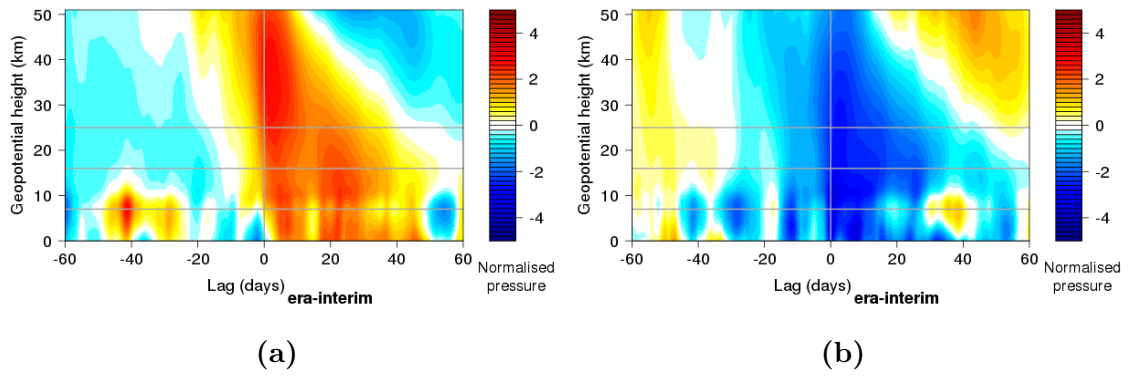
Figure 3.8: As in Fig. 3.7, normalised by standard deviation.
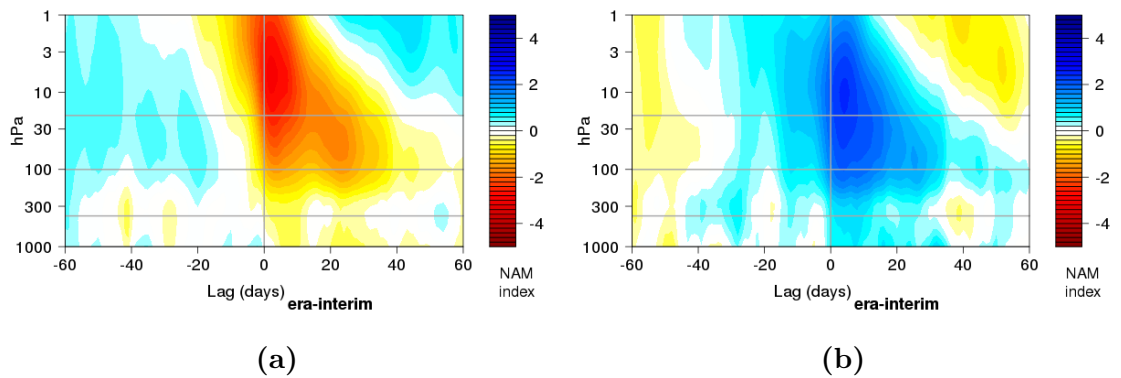
Figure 3.9: Composite of time-height development of the NAM for **(a)** 25 weak vortex events; **(b)** 17 strong vortex events, Northern Hemisphere.
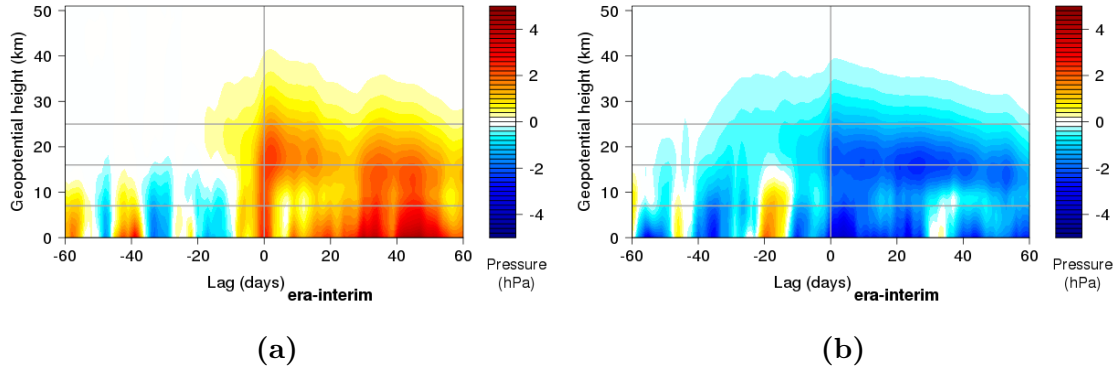
Figure 3.10: Composite of time-height development of **(a)** 20 positive polar cap pressure anomalies; **(b)** 16 negative polar cap pressure anomalies, Southern Hemisphere.
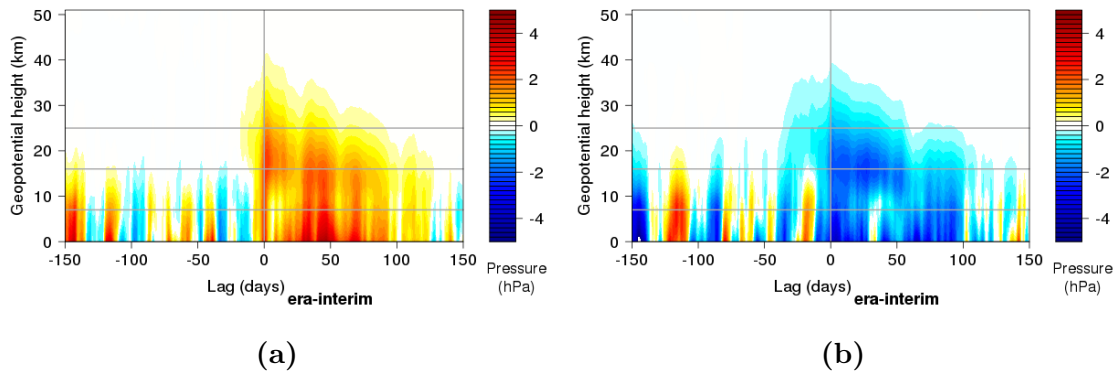
Figure 3.11: Extended composite of time-height development of **(a)** 20 positive polar cap pressure anomalies; **(b)** 15 negative polar cap pressure anomalies, Southern Hemisphere.

and 17 'strong vortex' events from when the 20 hPa annular mode value crosses $+2\sigma$ (Fig. 3.9b). Figures 3.8 and 3.9 are notably similar in the stratosphere region, with the events progressing concurrently across an almost identical time period. There is less similarity in the troposphere, as the NAM plots do not identify the tropospheric connection as prominently as the pressure plots.

Figure 3.10 shows composites of events over the austral polar cap, with 20 events in the positive case, and 16 in the negative. The onset periods of both are slightly longer than their northern counterparts, with up to 20 days onset visible in the stratosphere prior to a positive event, and 50–60 days before a negative event crosses 2σ. This is notable given that under standard definitions, SSWs are not as common in the Southern Hemisphere as they are in the north. While the frequency is indeed less, there are still quite a large number of positive events found here. The events also persist longer in the Southern Hemisphere, with both positive and neg-

ative composites exceeding the end of the 60-day period proposed by Baldwin and Dunkerton (2001), and persisting for up to 130 days (Fig. 3.11). To ensure that the same event was not counted twice, this was re-computed with a 150-day threshold, and as a result, one of the negative events was removed.

3.5 Summary

- Polar cap anomalies look very similar to NAM 'dripping paint' plots of Baldwin and Dunkerton (2001).

- Pressure anomalies have the opposite sign to the NAM index, with positive anomalies correspond to weak polar vortex events ($-$NAM), and negative anomalies corresponding to strong polar vortex events ($+$NAM).

- Composites conditioned on extremes at 25 km show an interesting profile that is symmetric between positive and negative events.

- The anomaly profile in the Southern Hemisphere is very similar to that of the Northern Hemisphere, in both shape and magnitude.

- Tropospheric amplification occurs almost instantaneously following a positive stratospheric event at 25 km, and persists for around 50 days, following a 10-day onset period.

- Negative stratospheric events have a slow onset period, suggesting a different causal mechanism, but a similar persistence of about 50 days.

- In the Southern Hemisphere, anomalous stratospheric events last for considerably longer, persisting for up to 130 days.

4 Representation of polar cap mass movement in reanalysis data

4.1 Introduction

In this chapter, comparisons will be made of tropospheric amplification in ERA-interim and other reanalysis datasets—ERA-40, JRA-55, NCEP-NCAR, and NCEP-DOE. (Details of each dataset can be found in Table B.1.)

4.2 Reanalysis Comparisons

Table 4.1: Number of days included in each reanalysis composite. Numbers in brackets are for the period Jan 1979–Aug 2002.

| Reanalysis | Northern Hemisphere | | |
	$p_{\text{cap},25} > 2\sigma$	$p_{\text{cap},25} < -2\sigma$	Std. dev. σ (hPa)
ERA-40	722 (348)	508 (337)	0.814 (0.803)
ERA-interim	553 (348)	443 (339)	0.805 (0.795)
JRA-55	856 (318)	644 (368)	0.870 (0.858)
NCEP-DOE	514 (334)	415 (332)	0.776 (0.764)
NCEP-NCAR	968 (288)	823 (384)	0.756 (0.764)

| Reanalysis | Southern Hemisphere | | |
	$p_{\text{cap},25} > 2\sigma$	$p_{\text{cap},25} < -2\sigma$	Std. dev. σ (hPa)
ERA-40	492 (438)	679 (152)	0.745 (0.605)
ERA-interim	462 (273)	411 (280)	0.603 (0.555)
JRA-55	657 (228)	659 (367)	0.609 (0.587)
NCEP-DOE	459 (286)	353 (269)	0.590 (0.551)
NCEP-NCAR	723 (512)	843 (148)	0.727 (0.565)

Figure 4.1 shows composites of all Northern Hemisphere anomaly events across the time periods of each reanalysis dataset. Table 4.1 shows the number of days composited into each curve, as well as the standard deviation of $p_{\text{cap},25}$, for each dataset by hemisphere. Overall the curves are qualitatively similar, with JRA-55 (green) having the largest magnitude anomalies, and NCEP-NCAR (red) having
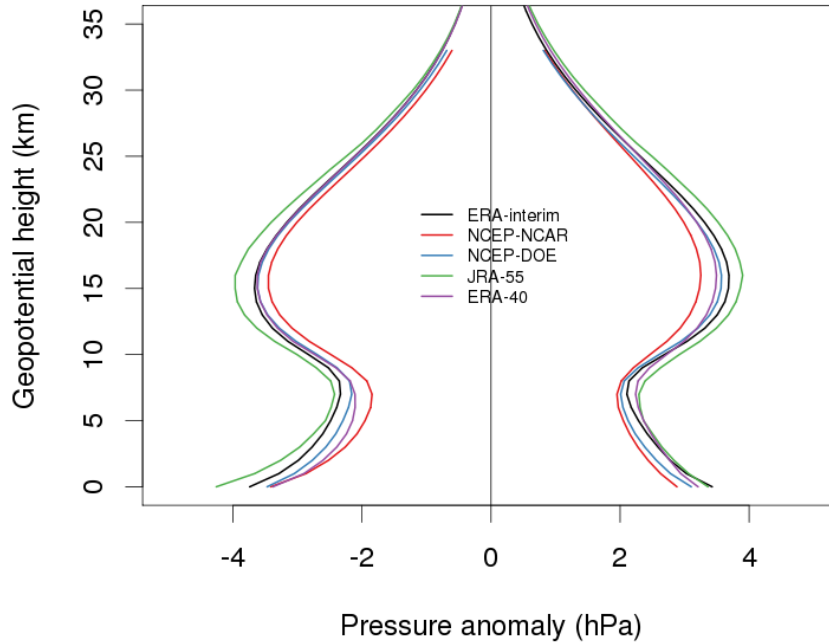
Figure 4.1: Composites of pressure anomalies over the Northern Hemisphere polar cap, defined on 2 standard deviations from the mean at 25 km for five reanalysis datasets. Time period is the whole data as shown in B.1.

the smallest. NCEP-DOE and ERA-interim are updated versions of NCEP-NCAR and ERA-40 respectively, with improved parameterisations and physical processes. NCEP-DOE (blue) and ERA-interim (black) are therefore expected to be more reliable than their predecessors, and their similarity to each other suggests that the representation of the polar cap pressure anomaly is robust.

Satellite observations only became routinely available around 1979, meaning that data from before then is less reliable. A number of reanalyses start in 1979 (and not before) because of this, including ERA-interim and NCEP-DOE. Table 4.1 shows values in brackets for the number of days exceeding $\pm 2\sigma$ between 1979 and 2002, where σ is the standard deviation of the dataset within that period. This is a common period for all datasets, and it can be seen that in the Northern Hemisphere, a similar number of days is recorded for each reanalysis, implying that they are picking up the same events but with different onset and ending dates. The Southern Hemisphere meanwhile is less consistent, with vastly differing numbers for both positive and negative event days. It may be expected that the number of days included when considering $\pm 2\sigma$ would be identical for each reanalysis, given that

(a) Whole reanalysis   **(b)** Reanalysis since 1979
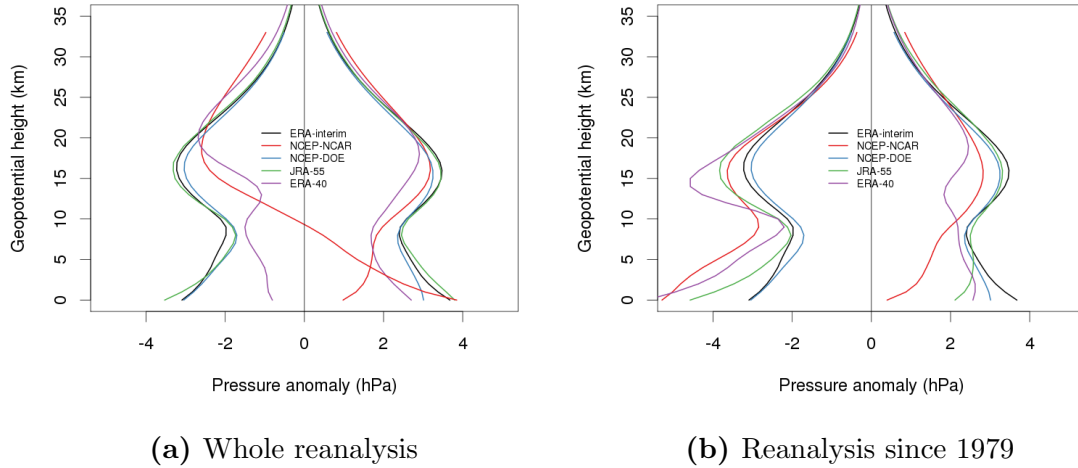
Figure 4.2: Composites of pressure anomalies over the Southern Hemisphere polar cap, defined on 2 standard deviations from the mean at 25 km for five reanalysis datasets.

the standard deviation is being taken across the same number of days in each case. However, the values of σ show that the spread of points in each dataset differs, and it was shown previously in Figure 3.2 that while theoretically symmetrical, the actual distribution of data points is not completely symmetric. Therefore, the number of days included within $\pm 2\sigma$ differs by dataset, even across the same time period.

There is not a notable difference between the Northern Hemisphere anomaly plots using the whole dataset (such as Fig. 4.1), and those using only the data since 1979 (not shown), but there is a more obvious difference between these plots for the Southern Hemisphere (Fig. 4.2), which may be a result of the vastly differing number of days considered.

Figure 4.2a covers the entire time period of the respective reanalysis, and Figure 4.2b covers only the data since 1979. (Since ERA-interim and NCEP-DOE start in 1979, their curves are identical in each plot.) Unexpectedly, JRA-55 (green) is actually closer to ERA-interim (black) and NCEP-DOE (blue) when the whole time series is used, and deviates from them quite significantly both in the troposphere, and for negative anomalies in the stratosphere, when using 1979 onwards. JRA-55 also loses the tropospheric amplification effect near the surface when considering 1979 onwards only. The other reanalyses, NCEP-NCAR (red) and ERA-40 (purple), do not agree with ERA-interim and NCEP-DOE; when using the whole dataset, they do not even reconstruct the expected shape of the composite profile, particularly for

negative pressure events. When using 1979 onwards, NCEP-NCAR and ERA-40 do not recreate the amplification effect in the positive anomalies, and over-exaggerate the negative amplification effect.

Table 4.2 shows the standard deviation σ of the $p_{\text{cap},25}$ time series for each re-analysis dataset for 1979 onwards. It is clear that JRA-55 has a higher standard deviation than the others in the Northern Hemisphere, which explains why the JRA-55 curve in Figure 4.1 has a higher magnitude. In the Southern Hemisphere, the standard deviations are all similar to each other, which implies that the large differences in the curves are not based on drastically different $p_{\text{cap},25}$ time series. This is reaffirmed in Table 4.3, which looks at the correlations between each reanalysis time series. In the Southern Hemisphere, the lowest correlations are between ERA-40 and the other reanalyses, but these are still higher than 0.8. The highest correlations in the Southern Hemisphere are between the three more modern reanalyses, ERA-interim, JRA-55, and NCEP-DOE, with each being above 0.96. In the Northern Hemisphere, every correlation is above 0.98.

Considering how well the reanalyses agree with each other in the Northern Hemisphere, as shown in Figure 4.1 and Table 4.3, more of an agreement between reanalyses in the Southern Hemisphere than what is seen in Figure 4.2 would be expected. Even with the limited number of available middle-atmosphere observations, if each reanalysis is using the same source data, they should produce similar results. It should be noted however that almost the entire austral polar cap region is covered by Antarctica, which has an average thickness of 2 km, and as such, the 0–2 km results are less accurate due to essentially being extrapolated under the surface of the ice sheet.

4.3   Regression model

Since the data is prone to sampling variability, a more robust definition of a pressure anomaly than that used in Section 3.2 should be considered for extended comparisons. Regression analysis can be used to quantify how a response variable is related to one or more explanatory variables. Unlike the composites, which only use a selec-

Table 4.2: Standard deviation σ (hPa) of the pressure time series at 25 km, $p_{\text{cap,25}}$, for each reanalysis since 1979.

	Northern Hemisphere	Southern Hemisphere
ERA-40	0.803	0.605
ERA-interim	0.805	0.603
JRA-55	0.876	0.636
NCEP-DOE	0.776	0.590
NCEP-NCAR	0.780	0.623

Table 4.3: Correlation between each reanalysis of their pressure time series at 25 km, $p_{\text{cap,25}}$, for 1979–2013 (1979–2002 for ERA-40).

Northern Hemisphere					
	ERA-40	ERA-interim	JRA-55	NCEP-DOE	NCEP-NCAR
ERA-40	—	0.990	0.992	0.980	0.981
ERA-interim	0.990	—	0.998	0.995	0.987
JRA-55	0.992	0.998	—	0.993	0.991
NCEP-DOE	0.980	0.995	0.993	—	0.993
NCEP-NCAR	0.981	0.987	0.991	0.993	—

Southern Hemisphere					
	ERA-40	ERA-interim	JRA-55	NCEP-DOE	NCEP-NCAR
ERA-40	—	0.862	0.891	0.806	0.891
ERA-interim	0.862	—	0.980	0.975	0.931
JRA-55	0.891	0.980	—	0.963	0.943
NCEP-DOE	0.806	0.975	0.963	—	0.952
NCEP-NCAR	0.891	0.931	0.943	0.952	—

(a) Whole year   **(b)** Wintertime (DJFM)
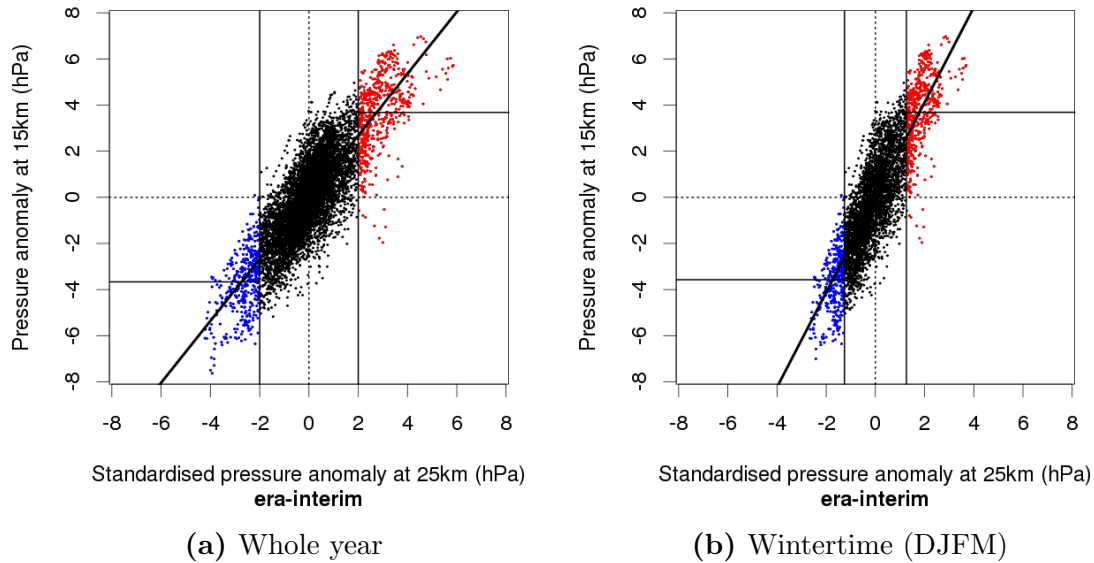
Figure 4.3: Northern Hemisphere pressure at 15 km regressed against pressure at 25 km. Thick line is the regression fit, vertical lines are ± 2 standard deviations. Horizontal line segments are the composite means.

tion of the data over the winter time period, regression analysis uses all the available data, which is more representative of the whole. Figure 4.3 shows the scatter plot for the regression of pressure at 15 km against pressure at 25 km. Parameter β_1 is the slope of the regression fit line, and the points in red and blue show (respectively) the positive and negative wintertime events included in the $\pm 2\sigma$ composite plots (such as Fig. 3.3a), with the horizontal segments showing the composite mean. Figure 4.3a shows the whole year, so is an accurate representation of how much of the data is included in the composites. Figure 4.3b just uses data from 'wintertime', so that the regression is not influenced by unrelated summer conditions. Note that Northern Hemisphere 'wintertime' is defined here as December, January, February *and March* (DJFM), since this is the time period which includes the majority of tropospheric amplification events found in Section 3.2 and shown in Figure 3.2.

Here, the pressure time series at each height, p_Z, is regressed linearly against the pressure at 25 km, p_{25}, according to:

$$p_Z = \beta_0 + \beta_1 p'_{25} + \xi \tag{2}$$

where $\beta_0 \approx 0$ and ξ is a random error term which represents natural variability and

62

(a) Northern Hemisphere (DJFM) **(b)** Southern Hemisphere (ASON)
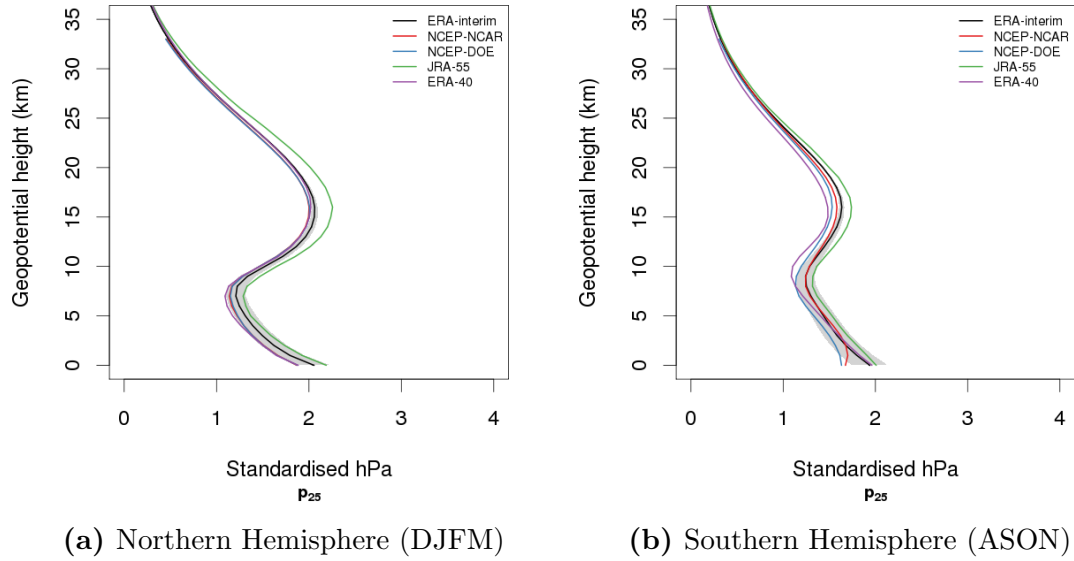
Figure 4.4: Wintertime pressure slope estimates β_1 obtained by regression on standardised pressure at 25 km, 1979 onwards. ERA-interim shows a 95% pointwise confidence band.

'noise'.

The regression slope coefficient β_1 is estimated from the 'sums of squares':

$$\beta_1 = \frac{SS_{xy}}{SS_{xx}} = \frac{\sum \left(p'_{25} - \overline{p'_{25}} \right) \left(p_Z - \overline{p_Z} \right)}{\sum \left(p'_{25} - \overline{p'_{25}} \right)^2}$$

β_1 is standardised to units of hPa by

$$p'_{25} = \frac{p_{25}}{\mathrm{sd}(p_{25})} \ ,$$

where the standard deviation $\mathrm{sd}(p_{25})$ is an estimate of σ. The regression is calculated separately for each height Z, but it should be noted that this method means there is no longer a measurable distinction between positive and negative events. The estimates of β_1 at each geopotential height Z are combined into one curve, shown for each reanalysis dataset in Figure 4.4a.

Figure 4.4a shows the same general shape as Figure 4.1, with a peak stratospheric effect at 15–18 km indicating the Rossby wave pump, a minimum at 7 km indicating the tropopause, and a tropospheric amplification effect near the surface which has a similar magnitude to the stratospheric peak. In the troposphere, each reanalysis curve is located within the 95% pointwise confidence band of ERA-interim, sug-

(a) Northern Hemisphere (DJFM) **(b)** Southern Hemisphere (ASON)
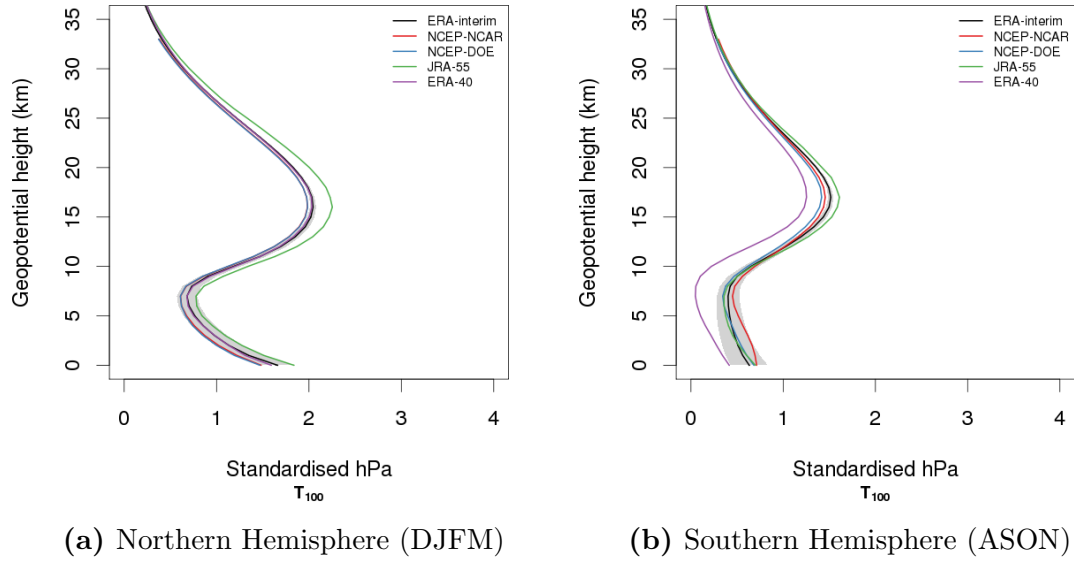
Figure 4.5: Wintertime pressure slope estimates β_1 obtained by regression on standardised temperature at 100 hPa, 1979 onwards. ERA-interim shows a 95% pointwise confidence band.

gesting that the reanalyses are significantly similar under a 95% confidence test. Details on the confidence interval definition can be found in Appendix G. This is as expected, since the data are based on shared observations, and as such are not independent of each other. The confidence band is narrower in the stratosphere, due to there being less variability, but the curves are still very close together. As noted earlier, JRA-55 (green) has a larger stratospheric variability, while ERA-40 (purple) has a slightly lower variability; this is more noticeable in the Southern Hemisphere plot (Fig. 4.4b).

In the Southern Hemisphere, the active period is defined as August, September, October and November (ASON). While this is not the standard 'winter' period, this is the period which includes the majority of stratospheric variability tropospheric amplification events. This is likely due to the delay in the polar vortex spinup caused by stratospheric ozone loss (Keeble et al., 2014). Unlike Figure 4.2b, it is not only the more recent reanalyses ERA-interim, NCEP-DOE and JRA-55 which produce the expected regression curve shape in Figure 4.4b. Rather, all the curves seem to show the general shape, but not with as large a range between minimum and maximum as the Northern Hemisphere plot (Fig. 4.4a). The regression on p_{25} (Fig. 4.4b) does not show the tropopause minimum at 7 km as clearly as it is in

the Northern Hemisphere, and the stratospheric peak at 15–18 km is also not as pronounced. This may be an indication of the effect being weaker overall in the Southern Hemisphere, but that is countered by the similarity shown previously for the Southern Hemisphere in Figure 3.3.

p_{25} is only one possible metric to use for regression; depending on available data, temperature at 100 hPa, T_{100}, as used by Baldwin et al. (submitted 2017), can also be considered. They chose 100 hPa as it has the highest correlation with PV anomalies, specifically on the 550 K isentropic surface, and is the lowest standard surface in the 'overworld' of Holton et al. (1995), above 380 K. Using T_{100} avoids the situation of a perfect fit regression when $z = 25$ that is seen using p_{25}.

Table 4.4: Correlation between wintertime T_{100} and p_{25} for each reanalysis since 1979.

	Northern Hemisphere Wintertime (DJFM)	Southern Hemisphere Wintertime (ASON)
ERA-40	0.950	0.779
ERA-interim	0.952	0.876
JRA-55	0.954	0.868
NCEP-DOE	0.949	0.889
NCEP-NCAR	0.949	0.870

Table 4.4 shows the wintertime correlation between p_{25} and T_{100} for each reanalysis. In the Northern Hemisphere, this is around 0.95 for every reanalysis, while in the Southern Hemisphere, it is slightly lower, with ERA-40 at 0.78 and the others around 0.87. This implies that T_{100} is a valid alternative to p_{25}.

Figure 4.5 shows regressions of pressure p_Z against the time series of T_{100}, according to:

$$p_Z = \beta_0 + \beta_1 \frac{T_{100}}{\mathrm{sd}(T_{100})} + \xi \ . \tag{3}$$

Figure 4.5a also shows the same shape as Figure 4.1, including the height of the Rossby wave pump, the tropopause, and a tropospheric amplification effect. Notably, both the regression on p_{25} in Figure 4.4a and the regression on T_{100} in Figure 4.5a suggest that the tropospheric amplification has a magnitude of approximately 1 hPa, adding to the 1 hPa anomaly at the tropopause (~ 7 km) for a total surface

pressure anomaly of 2 hPa. All the reanalyses concur with this value.

Figures 4.4 and 4.5 only use data from 1979 onwards; if the full time period is used (not shown), the curves for all Southern Hemisphere reanalysis datasets are similar to their positive anomaly equivalent in Figure 4.2b, reinforcing the proposal that the regression method is a suitable equivalent to the composites, and also reinforcing the findings that the data since 1979 is more reliable than prior data, even in the older models NCEP-NCAR and ERA-40.

Another Southern Hemisphere discrepancy is present in the regression on T_{100} (Fig. 4.5b), which fails to register much tropospheric amplification at all, aside from a small amount in JRA-55 (green). Given how similar the T_{100} regression is to the anomaly composite in the Northern Hemisphere (Figs. 4.5a and 4.1), it is more likely an issue with the Southern Hemisphere data rather than the use of T_{100} as a metric, and may again stem from the different methods of data assimilation and forecasting that each reanalysis uses, and the lack of Southern Hemisphere observations, as mentioned previously.

To further reduce the inter-reanalysis variability, each dataset can be regressed on *the same* p_{25} or T_{100} time series instead of *their own* p_{25} or T_{100} time series. The common time period used for this regression is 1979–2001, since all five reanalyses have data within this period. This was studied on both ERA-interim's time series and JRA-55's time series, but since there is very little observable difference between them (ERA-interim is slightly tighter in the Southern Hemisphere stratosphere), only regressions on JRA-55 are shown (Fig. 4.6). There is little difference between the Northern Hemisphere regressions on JRA-55 (Figs. 4.6a and 4.6b) and the regressions on themselves (Figs. 4.4a and 4.5a). Figure 4.6 shows the curves of each reanalysis are closer together than in Figures 4.4 and 4.5, implying a larger variance between reanalysis datasets when they are regressed on themselves, but this difference is negligible.

There is also not much of a difference in the Southern Hemisphere regressions. When regressing on JRA-55 (Figs. 4.6c and 4.6d), all of the datasets are slightly closer together, and follow the same general shape as JRA-55 in Figures 4.4b and
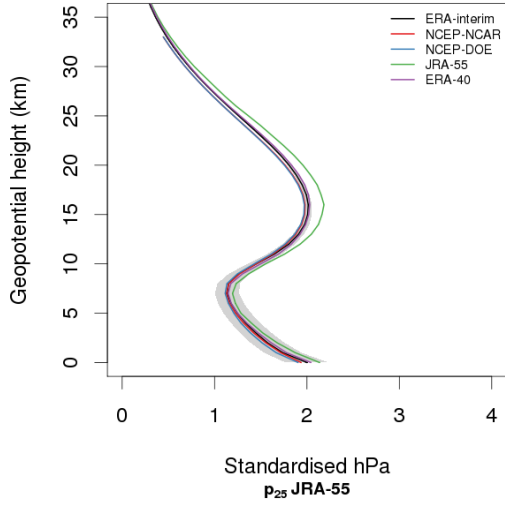
(a) Northern Hemisphere, p_{25}
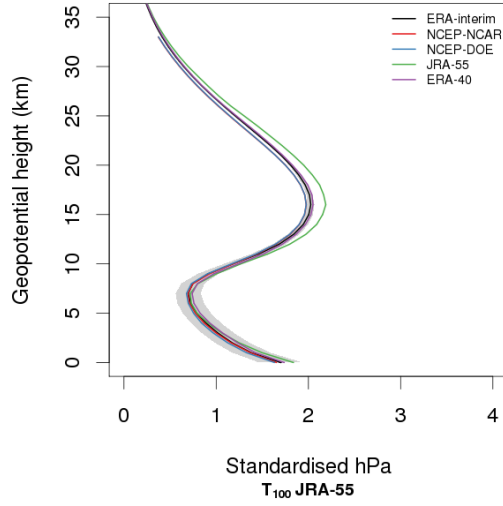
(b) Northern Hemisphere, T_{100}
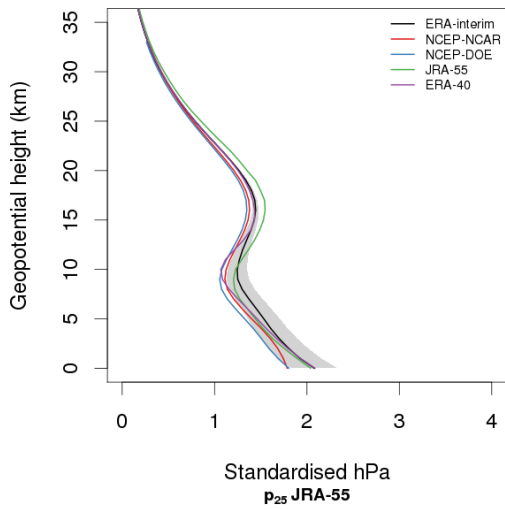
(c) Southern Hemisphere, p_{25}
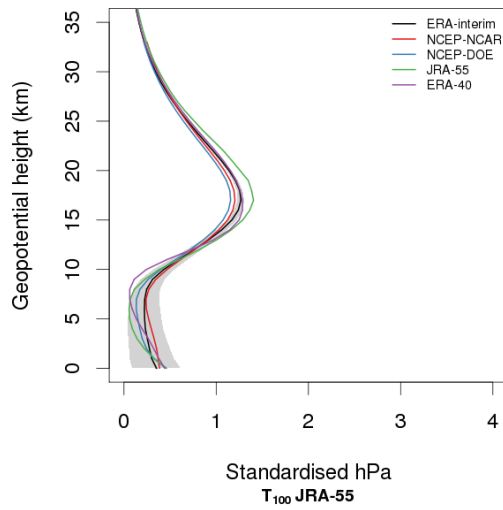
(d) Southern Hemisphere, T_{100}

Figure 4.6: **(top)** Northern Hemisphere wintertime (DJFM); **(bottom)** Southern Hemisphere wintertime (ASON), pressure slope estimates β_1 obtained by regression on JRA-55's **(left)** standardised pressure at 25 km; **(right)** standardised temperature at 100 hPa. ERA-interim shows a 95% pointwise confidence band.

4.5b respectively. It turns out that there is little difference between regressions of the reanalysis datasets on JRA-55's p_{25} and T_{100} and regressions of the data on their own p_{25} and T_{100} *if only the data beginning in 1979 are considered*. Therefore the method here does not significantly reduce the inter-reanalysis variability.

Because it remains the most consistent in comparison with the composite plots, p_{25} will be the explanatory variable used hereinafter. Since ERA-interim remains consistent in both hemispheres, and sits mostly in the middle of the more modern reanalyses (itself, NCEP-DOE, and JRA-55), this will be the reanalysis used throughout the rest of the thesis, and considered a good representation of the 'true' atmosphere.

4.4   Summary

- In the Northern Hemisphere, there is very little difference between the pressure anomaly profiles of each reanalysis dataset.

- In the Southern Hemisphere, similarity between the datasets improves after 1979, when observation methods moved towards satellite data.

- The regression method gives similar profiles to composites, and allows uncertainly to be qualified in addition to using the whole dataset rather than just $\pm 2\sigma$.

- Both p_{25} and T_{100} can be used as a regression metric, producing similar results, so the choice of which to use in any given situation can be made based on the data and intended outcomes, rather than the method, to ensure robust results.

- There is no inherent benefit to using one reanalysis dataset over another, and no significant improvement in using one dataset as the metric to regress all others against.

5 Representation of polar cap mass movement in historical and future CMIP5 model simulations

5.1 Introduction

Designed as state-of-the-art models to advance our understanding of climate variability, the models which participated in CMIP5 are a group of atmosphere-ocean GCMs (AOGCMs) with interactive representations of the atmosphere, land, ocean, and sea ice, usually coupled to earth system models (ESMs) which include carbon cycle components, and occasionally interactive aerosol, chemistry, and vegetation as well (Taylor et al., 2012).

Simulations from the CMIP5 multi-model ensemble archive were investigated to see how well they recreate the phenomenon seen in the reanalysis data. The models were selected based on the following criteria:

- available daily data (events are unlikely to show up at lower temporal resolution)

- available Geopotential Height (Z or zg) field (for interpolation)

- available data at the 1000 hPa level on all longitudes and latitudes (for interpolation)

- an upper model lid of at least 10 hPa ($\sim$ 30 km), to include the lower stratosphere

A list of the selected models is shown in Table A.1. Some models had multiple runs of different scenarios (e.g., six 'historical' runs or three 'RCP 4.5' runs); where these runs all included the necessary data, only the run numbered "r1" was used.

5.2 CMIP5 Historical Runs

Each historical simulation was initialised from an arbitrary point of a pre-industrial control, and forced by observed atmospheric composition changes (Taylor et al.,

2012). The historical runs cover the industrial period to the present (1850–2005), with most models' available output data starting in 1950 after a 100-year spin-up. Following the criteria outlined in Section 5.1, eleven CMIP5 models, detailed in Table A.1, were selected. Of those eleven models, the three CMCC models are derived from the same base, and as such are not entirely independent of each other; they have the same atmosphere and ocean components, just with different resolutions, and CMCC-CESM complements these with additional land surface and ocean bio-geochemistry components. The three MPI-ESM 'models' are also based on the same components, just with different resolutions. MPI-ESM-P is the same configuration as MPI-ESM-LR, but with prescribed vegetation. This means that from the eleven models, there are seven completely distinct, independent models considered, with the remaining four being used to determine differences that arise from within similar configurations. From the regression model in Equation 2, each model can be plotted as 'Geopotential height' Z (in km), against 'Standardised hPa' β_1 (similar to Figs. 4.4–4.6). This plot can be seen in Figure 5.1.

The anomaly definition from Section 3.2, $|p| > 2\sigma_Z$, was used again to produce Figure 5.2 (directly comparable with Fig. 4.1). The shape and magnitude of each curve in Figure 5.1 is similar to the positive curve of the same model in Figure 5.2, again showing how the regression can be used as a metric to represent the pressure anomalies and tropospheric amplification. Most noticeable are the positions of the CanESM2 model curve, which has the lowest tropospheric amplification; the CMCC-CESM model curve, which has the largest stratospheric component, and a higher stratospheric peak to the other models; and the curve of MPI-ESM-MR, which is consistently the closest to ERA-interim.

As indicated in Table A.1, Figure 5.1 shows six 'high-top' models (Fig. 5.1a) and five 'low-top' models (Fig. 5.1b), a distinction which indicates the height of the model 'lid', which is the vertical extent of the model's calculations. A 'low-top' model has a lid below 1 hPa ($\sim$48 km), while a 'high-top' model has a lid above that level. An important difference between the two is that high-top models have a fully-resolved stratosphere, while low-top models do not even include the
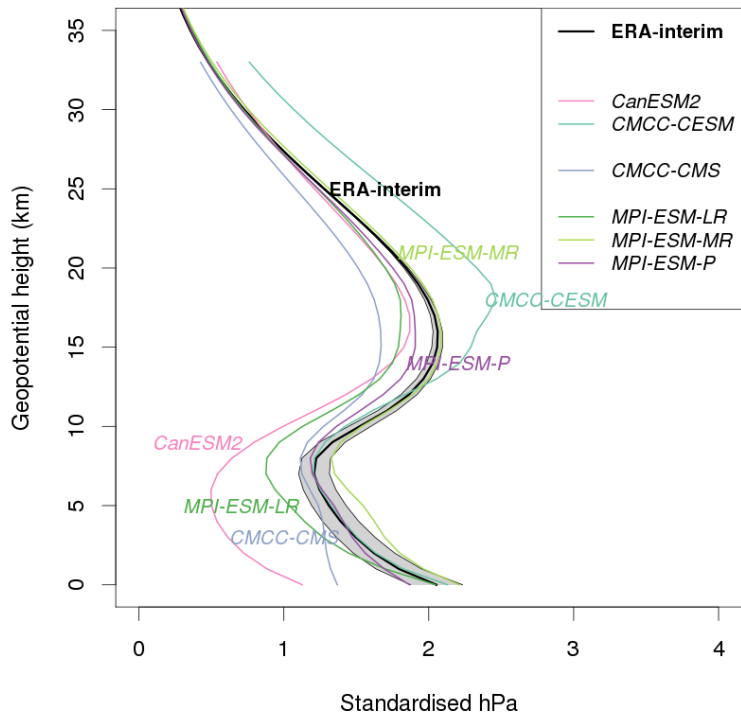
(a) High-top models
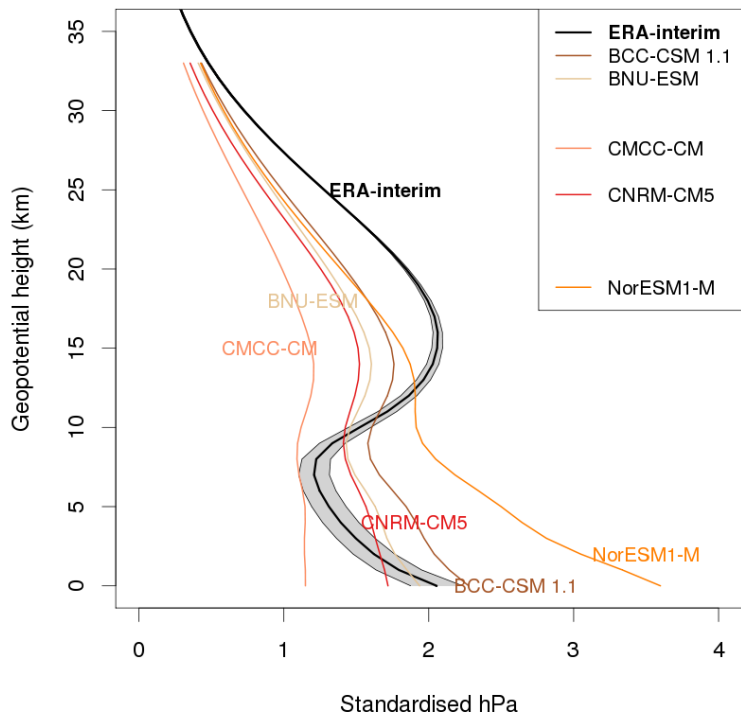
(b) Low-top models

Figure 5.1: Northern Hemisphere wintertime (DJFM) pressure slope estimates β_1 obtained by regression on standardised pressure at 25 km. ERA-interim shows a 95% pointwise confidence band.

(a) High-top models   **(b)** Low-top models
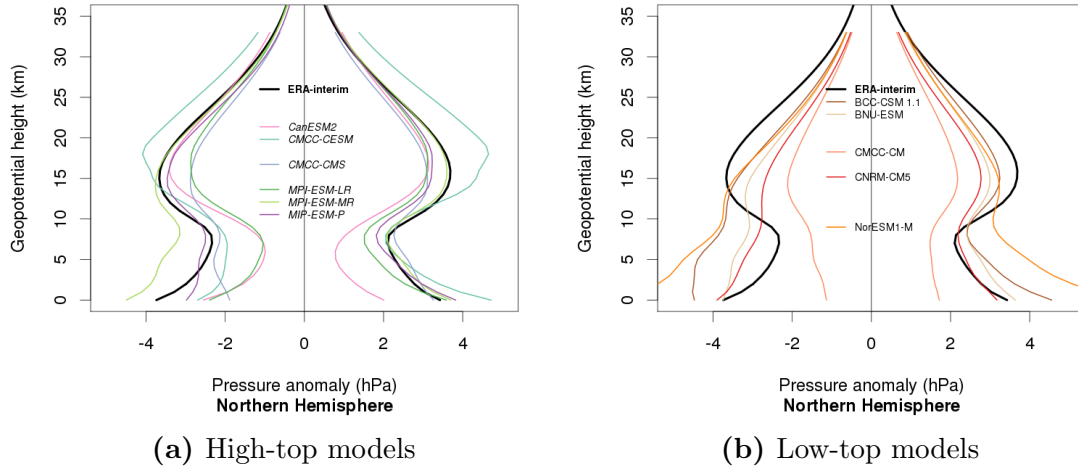
Figure 5.2: Composites of pressure anomalies over the Northern Hemisphere polar cap, defined on 2 standard deviations from the mean at 25 km for eleven CMIP5 models and ERA-interim.

whole stratosphere. It is also important to note however that both classes of models have different vertical resolutions themselves, with some being finer than others; for example, in the 5–15 km region, CanESM2 has a vertical resolution of 1.137 km, MPI-ESM-MR has a vertical resolution of 0.646 km, and CNRM-CM5 has a vertical resolution of 0.874 km (Anstey et al., 2013). As discussed in Charlton-Perez et al. (2013), low-top models have very weak stratospheric variability, underestimate the frequency of SSWs, and do not produce the long-lasting S-T coupling effects that have been seen in observations.

Each high-top model has successfully reproduced the general qualitative shape of the tropospheric amplification curve of ERA-interim, showing a stratospheric peak between 15–18 km, the tropopause height at around 7 km, and the tropospheric amplification at the surface. Conversely, the low-top models do not effectively recreate the phenomenon at all; there is a very small stratospheric peak below 15 km and hardly any indication of the tropopause. There is also little indication of much tropospheric amplification, but what there is does mirror the stratospheric peak, except in NorESM1-M, where the amplification at the surface is significantly higher than both its own stratospheric peak and the other models' surface features. Within the high-top models, the three MPI-ESM configurations are the closest to recreating ERA-interim, with MPI-ESM-MR being the best, as it only deviates from the ERA-interim confidence band in the mid-troposphere. MPI-ESM-P is the closest of

72

the three to ERA-interim in the troposphere, but has a lower value throughout the stratosphere; comparing this directly with MPI-ESM-LR shows that the inclusion of prescribed vegetation in the model improves the output. CMCC-CESM clearly has the largest stratospheric component, but is consistently the closest model to ERA-interim in the troposphere. The models CMCC-CM and CMCC-CMS are the best for directly comparing the difference between high-top and low-top, as they are essentially the same model, just with a different lid height and vertical resolution (CMCC-CMS is also more coarse horizontally, with a T63 spectral resolution [1.875° × 1.875°] compared to T159 [0.75° × 0.75°] for CMCC-CM). While CMCC-CMS is not the best high-top model at recreating the profile of ERA-interim – the values are consistently lower, and the troposphere region does not show sufficient amplification – it is clear that this model follows the general shape of the profile more closely than CMCC-CM.

It is clear from Figure 5.1 overall that models which fully resolve the stratosphere are much better at representing this aspect of S-T coupling than those which do not. In addition to simply having a higher model lid, such models also have a greater number of sophisticated stratospheric parameterisations included (as mentioned in Section 2.5), which allow them to more accurately account for stratospheric processes. Given that high-top models include these, whereas the low-top models do not, it can be concluded that some of these stratospheric processes are indeed directly related to the formation of tropospheric amplification features.

Figure 5.3 shows the same models in a regression of the Southern Hemisphere. As with the Northern Hemisphere, the high-top models (Fig. 5.3a) represent the phenomenon more accurately than the low-top models (Fig. 5.3b). MPI-ESM-MR is once again the closest to ERA-interim, but CMCC-CESM is considerably less accurate, as it does not show either a stratospheric peak, or the tropopause. Two of the low-top models, BNU-ESM and NorESM1-M, perform better than they did in the Northern Hemisphere, in that the general shape of the phenomenon is much clearer, but the magnitudes of the event are not as accurate as those of the high-top models. It was mentioned in Section 2.5 that certain climate models had systematic

(a) High-top models   **(b)** Low-top models
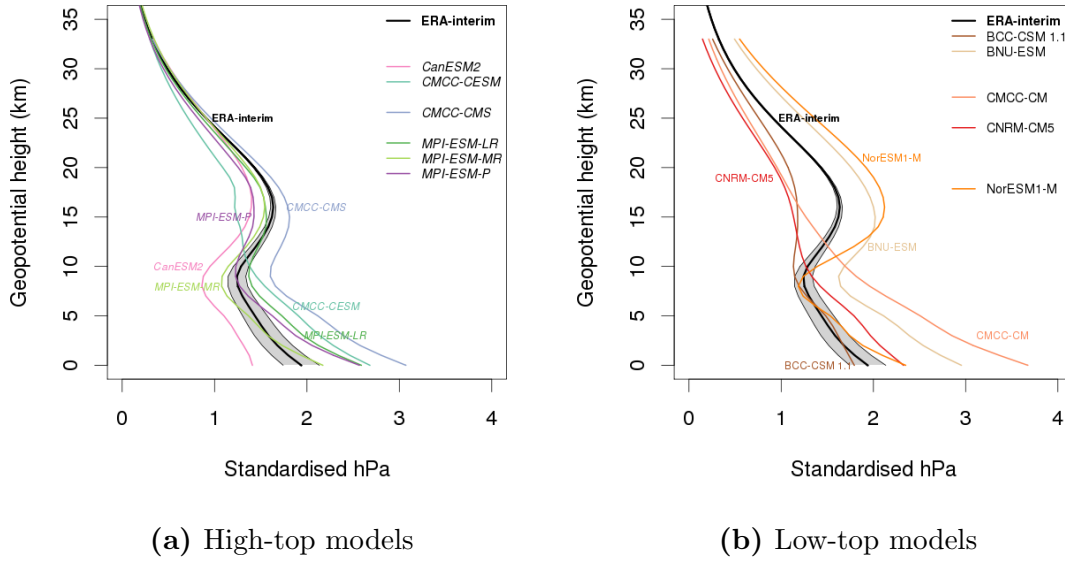
Figure 5.3: Southern Hemisphere wintertime (ASON) pressure slope estimates β_1 obtained by regression on standardised pressure at 25 km. ERA-interim shows a 95% pointwise confidence band.

biases in the Southern Hemisphere, which may explain some of the differences between each hemisphere's results. However, the overall difference doesn't seem to be that great, which may suggest an improvement in model construction between the models mentioned in previous literature and the CMIP5 models used here.

Figure 5.4 shows the time series of Northern Hemisphere polar cap pressure anomalies at 25 km, calculated as in Section 3.2 by removing the annual cycle, for the eleven CMIP5 models and ERA-interim. It is directly comparable to Figure 3.2. The five low-top models are shown above the plot of ERA-interim, and the six high-top models are below. It can be seen that each of the models generates a number of tropospheric amplification events based on the $\pm 2\sigma$ definition, but that there is a vast difference in standard deviation between models. The values of σ can be seen in Table 5.1 (comparable to Table 4.1), which also shows the number of days composited into Figure 5.2. The standard deviation is lower than ERA-interim in all low-top models, while that of high-top models is much closer. In general, the low-top models do not simulate past historical trends of anomalies as well as the high-top models; the high-top models meanwhile do not simulate the specifics of the past climate, but are much closer at the general trends in anomalies. For example, the total number of $\pm 2\sigma$ events in the high-top models for 1979–2005 is closer to
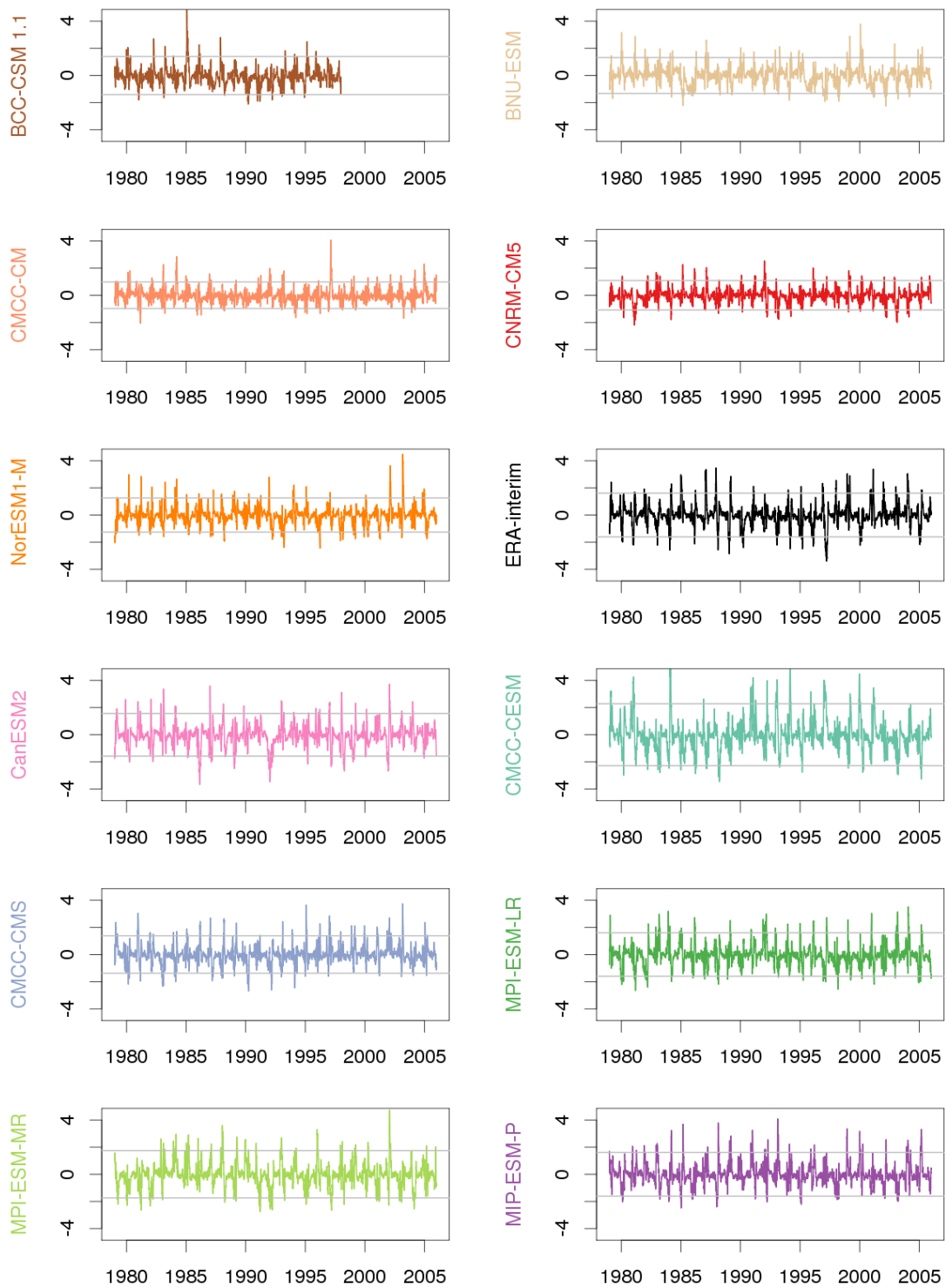
Figure 5.4: Daily polar cap pressure anomalies (hPa) at 25 km $p_{\mathrm{cap,25}}$ for 1979–2005, Northern Hemisphere. Grey lines show ± 2 standard deviations.
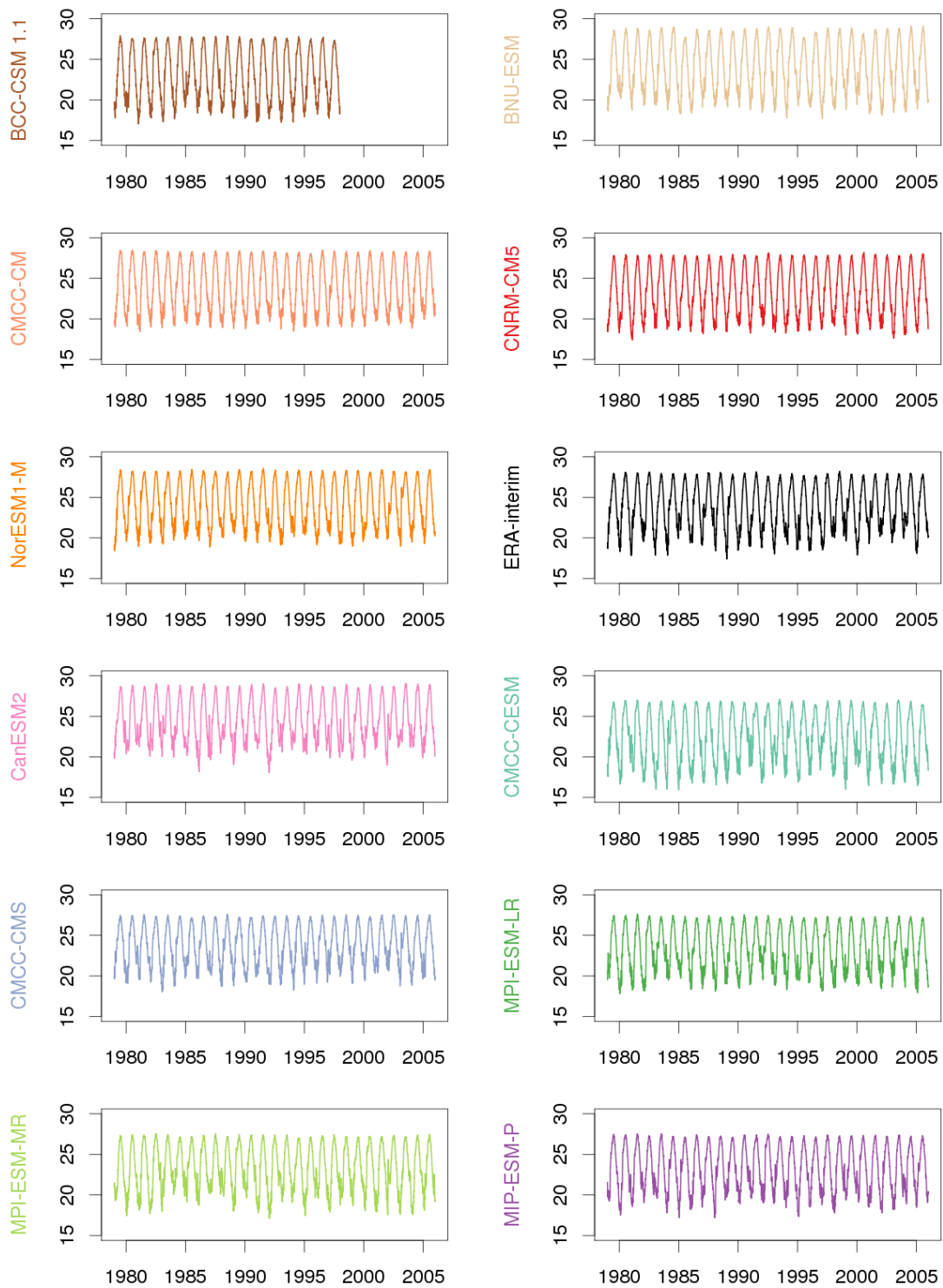
Figure 5.5: Absolute polar cap pressure (hPa) at 25 km for 1979–2005, Northern Hemisphere.

Table 5.1: Number of days included in each model composite. Numbers in brackets are for the period Jan 1979–Dec 2005 (*Dec 1997 for BCC-CSM1.1).

Model	Northern Hemisphere		
	$p_{\text{cap},25} > 2\sigma$	$p_{\text{cap},25} < -2\sigma$	Std. dev. σ (hPa)
BCC-CSM1.1	735 (219*)	356 (169*)	0.703 (0.646*)
BNU-ESM	758 (345)	492 (287)	0.661 (0.651)
CMCC-CM	690 (351)	541 (183)	0.488 (0.504)
CNRM-CM5	719 (331)	567 (423)	0.543 (0.503)
NorESM1-M	735 (288)	589 (339)	0.627 (0.647)
ERA-interim	553 (411)	443 (363)	0.805 (0.791)
CanESM2	898 (318)	828 (385)	0.786 (0.810)
CMCC-CESM	967 (460)	458 (221)	1.140 (1.112)
CMCC-CMS	882 (430)	570 (277)	0.690 (0.698)
MPI-ESM-LR	926 (388)	601 (323)	0.800 (0.776)
MPI-ESM-MR	893 (399)	639 (336)	0.870 (0.866)
MPI-ESM-P	875 (440)	595 (242)	0.806 (0.782)

that of ERA-interim, even if they are not occurring at the same points in time.

Figure 5.5 shows the absolute polar cap pressure over the same time period, without the removal of the annual cycle. The plots are all very similar to each other, with each model having an absolute pressure range of between 15 and 30 hPa at 25 km; this shows that the annual cycles in the models are similar, but the amplitudes and means vary by up to 2 hPa. While the models all have a realistic amplitude of the annual cycle, as well as mean absolute pressure, the models differ in the amplitude of the wintertime anomalies (Fig. 5.4). This reinforces findings in previous studies, where the CMIP5 models are able to reproduce the main features, particularly in temperature fields, but not the finer details (Flato et al., 2013). In the stratosphere, the models generally underestimate the historic cooling trend, with models that have interactive chemistry performing better than those with prescribed ozone (Eyring et al., 2013). Of the models considered here, CNRM-CM5 is the only one with fully interactive chemistry; BNU-ESM and NorESM1-M have semi-offline chemistry, where the prescribed ozone dataset has been calculated with the underlying model using prescribed SSTs but with their stratospheric ozone responding to changes in

(a) BCC-CSM 1.1 (low-top) **(b)** MPI-ESM-MR (high-top)
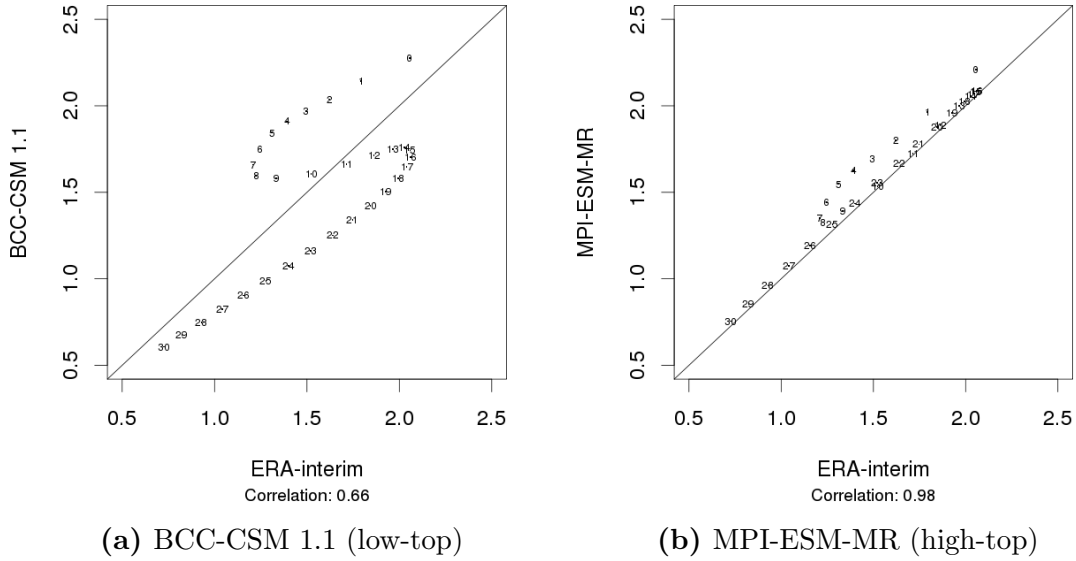
Figure 5.6: Scatter plot of β_1 from different models against β_1 from ERA-interim, Northern Hemisphere. Numbers indicate the corresponding height in km of each point.

GHG concentrations in the RCPs. The remaining models have completely prescribed ozone. Note that there is a mix of both high-top and low-top models in both categories, meaning the analysis of Eyring et al. (2013) cannot be compared directly with the high-top and low-top model investigation here.

The profile of β_1 from each model can be compared to that from ERA-interim by using scatter plots at each height. A model which gets a similar regression curve shape but a different magnitude is likely to be more accurate than a model which coincidentally hits some of the same values without recreating the expected vertical profile, as it shows that the atmospheric structure of that model is simulating the necessary systems even if it cannot get the correct magnitude. Figure 5.6 shows a scatter plot of one low-top model (BCC-CSM 1.1) and one high-top model (MPI-ESM-MR) against ERA-interim for the Northern Hemisphere, with the numbers in the plot referring to the height in km that each point corresponds to. It is clear that the high-top model has a significantly higher correlation, at 0.98, albeit with a slight overestimation specifically in the troposphere (points 0 to 8). The low-top model, conversely, has a rather low correlation, at 0.66, and it is clear that this model overestimates values in the troposphere (points 0 to 10) and underestimates values in the stratosphere (points 11 to 30). Table 5.2 gives the correlation coefficient for each model, which is summarised in Figure 5.7. As inferred above from the anomaly

Table 5.2: Correlation of β_1 from CMIP5 Models to β_1 from ERA-interim

Type	Model	Northern Hemisphere Correlation	Southern Hemisphere Correlation
High-top	CanESM2	0.73	0.92
	CMCC-CESM	0.88	0.80
	CMCC-CMS	0.97	0.91
	MPI-ESM-LR	0.95	0.93
	MPI-ESM-MR	0.98	0.97
	MPI-ESM-P	0.99	0.91
Low-top	BCC-CSM1.1	0.66	0.90
	BNU-ESM	0.69	0.95
	CMCC-CM	0.73	0.71
	CNRM-CM5	0.68	0.80
	NorESM1-M	0.42	0.89

composite and regression plots, high-top models generally have a higher correlation than low-top models, particularly in the Northern Hemisphere, which is indicated by the cluster of high-top models in the top-right of Figure 5.7. There is less variation in Southern Hemisphere correlation values, with most low-top model values falling close to the range of the high-top models. The low-top models in Figure 5.7 are scattered around the middle and left of the plot, and there is a fairly obvious split between high-top and low-top models.

Section 2.5 mentioned that some models do not accurately distinguish the asymmetry between the Northern and Southern Hemispheres, and that some models have a poorer performance or produce rather extreme results in the Southern Hemisphere. While the highest correlation value in the Southern Hemisphere is indeed lower than that of the Northern Hemisphere, it also appears that some models seem to perform better in the Southern Hemisphere than in the north; most of the low-top models have a higher correlation with ERA-interim in the south, as shown in Table 5.2, and Figure 5.3 also suggests that some of the low-top models follow the shape of the curve of ERA-interim (if not the magnitude) reasonably well. Therefore in this particular investigation, it does not appear to be the case that models have
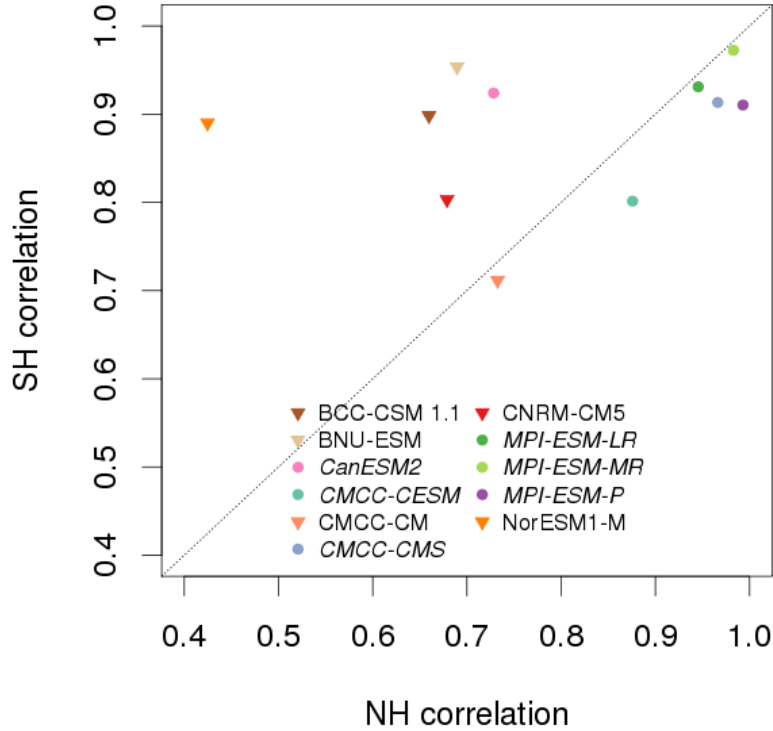
Figure 5.7: Northern Hemisphere model β_1 correlations to ERA-interim vs Southern Hemisphere β_1 correlations to ERA-interim. High-top models are in *italics*.

a significantly poorer performance in the Southern Hemisphere; indeed, for some models, performance actually improves over the Northern Hemisphere. It should be noted however that the ERA-interim profile in the Southern Hemisphere is overall 'straighter' than in the Northern Hemisphere, meaning that achieving a high linear correlation between the models and ERA-interim is easier. This means that while performance appears to be better in the Southern Hemisphere, this may be a result of the diagnostic used, rather than the models themselves.

5.3 Representative Concentration Pathways

Given that the high-top CMIP5 models are able to qualitatively recreate the tropospheric amplification seen in the reanalysis, it is of interest to see how these models predict changes in tropospheric amplification under future climate scenarios. In the stratosphere, there are two primary considerations for future climate development – the impact of greenhouse gases, such as CO_2, and the impacts of, and effects on, stratospheric ozone, O_3. In the troposphere, increased CO_2 leads to a warm-

ing effect, while in the stratosphere, this is reversed, with increased CO_2 leading to a cooling effect. Meanwhile, the historical loss of ozone due to ozone-depleting substances has led to the cooling effect of greenhouse gases being amplified, but as ozone recovers over the next century, this effect will be reversed, with increased ozone reducing, and in some cases even overturning, the stratospheric cooling effect (Maycock, 2016).

The CMIP5 multi-model ensemble archive contains four Representative Concentration Pathway (RCP) scenarios, based on possible increases in radiative forcing (Wm^{-2}) by 2100: RCP 2.6, RCP 4.5, RCP 6.0, and RCP 8.5. (RCP 2.6 is based on a radiative forcing increase of 2.6 Wm^{-2}, etc.) The time period covered is 1 January 2006 to 31 December 2100 for each model run. For this study, RCP 4.5 and RCP 8.5 are used, as these are the scenarios which are available from the majority of models. See Table A.1 for details of which models provided each dataset.

Scenario RCP 4.5 assumes a radiative forcing increase of 4.5 Wm^{-2} by 2100, requiring a decline in greenhouse gas emissions by 2040. The regression analysis for this in the Northern Hemisphere is shown in Figures 5.8a and 5.8c, and for the Southern Hemisphere in Figures 5.8b and 5.8d. Results from the ERA-interim reanalysis are shown as a baseline, along with each model's historical simulation. As with the historical curve, the curve of MPI-ESM-MR lies closest to ERA-interim in the Northern Hemisphere. The magnitude of the difference between each model's RCP 4.5 and its historical curve at the surface in the Northern Hemisphere varies by model from around 0.1 hPa for MPI-ESM-MR to more than 0.5 hPa for BNU-ESM and NorESM1-M (Fig. 5.8e). At the surface, the RCP curve of five models is lower than that of the historical, while it is higher for the other four. In the Southern Hemisphere (Fig. 5.8f), the curves exhibit a pattern of similarity which nearly all (except for MPI-ESM-MR) suggest an increasingly negative difference between RCP 4.5 and the historical simulation the closer it gets to the surface. As indicated by the narrower confidence band of ERA-interim, there is less variation in the stratosphere, which is replicated by the models as their RCP 4.5 and historical curves become closer together as height increases.
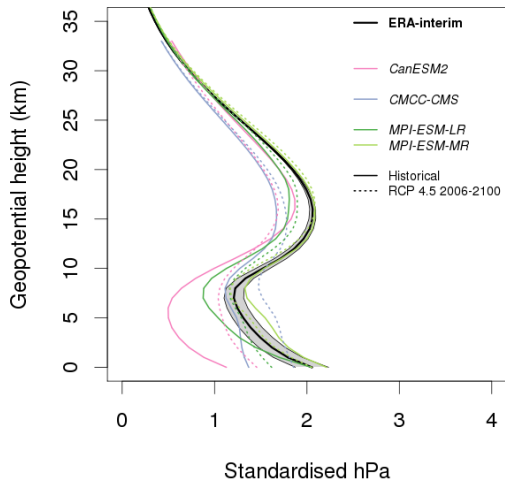
(a) High-top models, NH (DJFM)
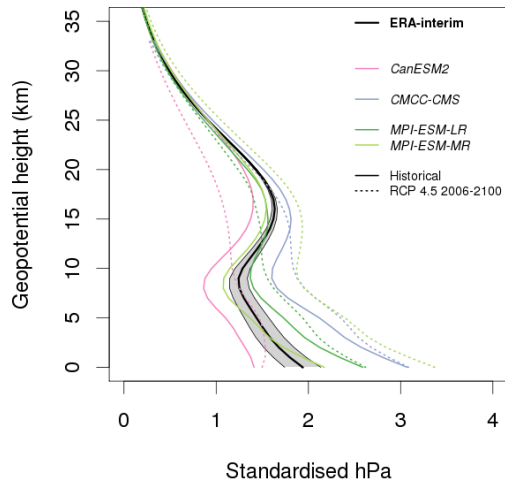
(b) High-top models, SH (ASON)
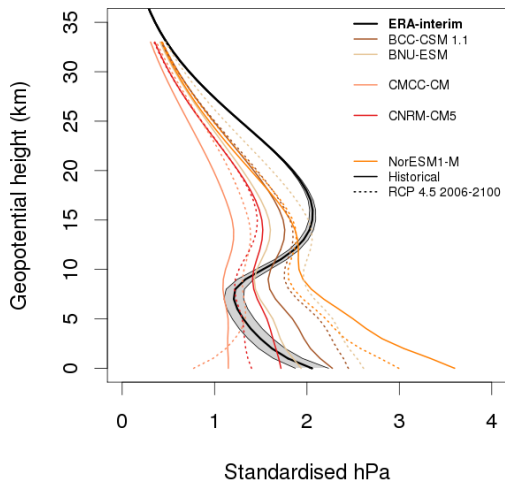
(c) Low-top models, NH (DJFM)
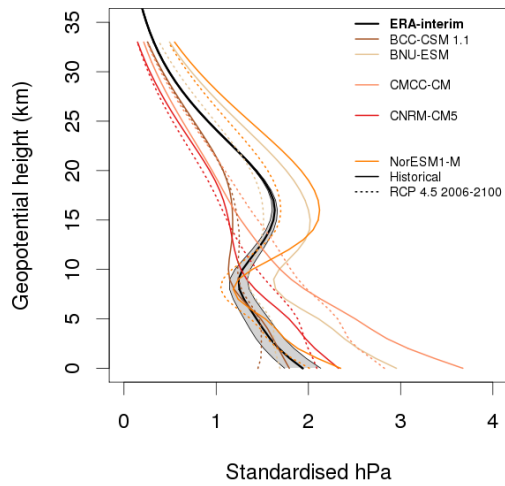
(d) Low-top models, SH (ASON)
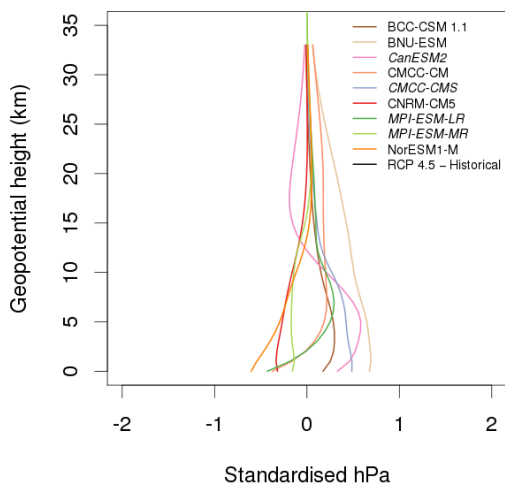
(e) RCP 4.5−Historical, NH (DJFM)
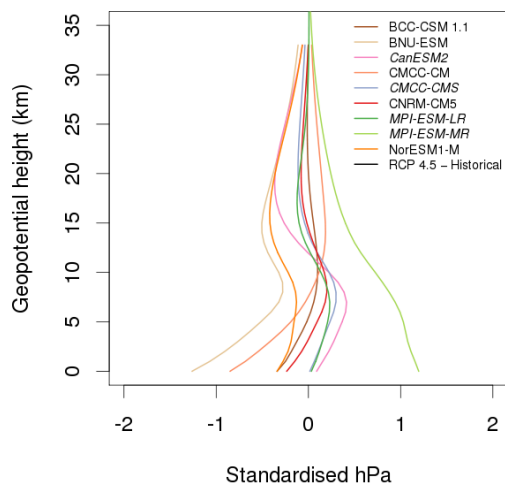
(f) RCP 4.5−Historical, SH (ASON)

Figure 5.8: **(a,b,c,d)** Wintertime pressure slope estimates β_1 obtained by regression on standardised pressure at 25 km, showing curves for ERA-interim (thick black), 9 CMIP5 historical simulations (solid colour), and 9 RCP 4.5 simulations (dotted colour). ERA-interim shows a 95% pointwise confidence band. **(e,f)** Difference between RCP 4.5 and historical curves for each of the 9 models. 82

(a) Northern Hemisphere (DJFM)   **(b)** Southern Hemisphere (ASON)
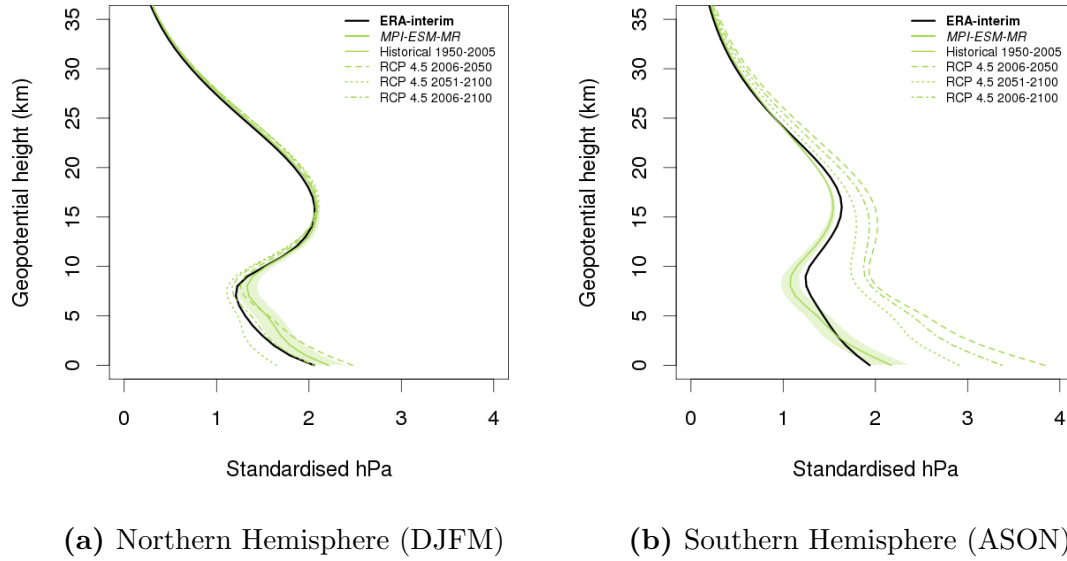
Figure 5.9: Wintertime pressure slope estimates β_1 obtained by regression on standardised pressure at 25 km for MPI-ESM-MR, showing ERA-interim (thick black), CMIP5 historical (solid colour), RCP 4.5 for the first half-century (dashed colour), RCP 4.5 for the second half-century (dotted colour), and RCP 4.5 for the whole century (dot-dash colour). The historical curve shows a 95% pointwise confidence band.

A notable model to look at in further detail is MPI-ESM-MR, being the model that was consistently the closest to ERA-interim when recreating the phenomenon in Section 5.2. As shown in Figure 5.9a, this model in the Northern Hemisphere does not suggest substantial changes to the tropospheric amplification phenomenon up to 2100, as all curves are very close to ERA-interim, but two of the three RCP 4.5 curves do lie mostly outside of the 95% confidence band of the historical curve. The 2006–2100 RCP 4.5 curve follows ERA-interim very closely, much like the historical curve. The first half-century 2006–2050 lies just to the right, and the latter half-century 2051–2100 lies just to the left. The majority of both half-century curves would lie just outside the 95% confidence band of ERA-interim (not shown). In the Southern Hemisphere (Fig. 5.9b), all three curves for RCP 4.5 are located significantly further to the right than both ERA-interim and the model's own historical simulation. Tropospheric amplification in the Southern Hemisphere for the model increases, by roughly 50% from 1950–2005 to 2051–2100. However, as indicated in Figure 5.8f, it is the only high-top model which shows such a striking difference between its RCP 4.5 curve and its historical simulation. It shows a large increase in the anomalous pressure in the troposphere and lower stratosphere.

Considering each of the other models individually (not shown), the four curves of RCP 4.5 2006–2050, 2051–2100, 2006–2100, and the historical simulation, are all consistently much closer to each other than they are to the curves of the other models or ERA-interim. This suggests that there is much more variability between models than there is between different simulations using the same model. When considering half a century (not shown), there is a similar variation in the location of the curves, with 2006–2050 sitting a bit further to the right of the historical curve, and 2051–2100 sitting closer to it. This may be indicative of the proposed reduction in greenhouse gas emissions after 2040, which would result in a reduction in stratospheric cooling.

Scenario RCP 8.5 assumes a radiative forcing increase of 8.5 Wm^{-2} by 2100, which implies no changes in policy to reduce greenhouse gas emissions, resulting in three times today's CO_2 emissions. The regression plots for both the northern and Southern Hemisphere are shown in Figure 5.10. As with RCP 4.5, there is more of a difference between the results from different models than there is between a single model's historical simulation and that model under RCP 8.5 forcing.

Comparing the curves of RCP 4.5 and RCP 8.5, there is a general trend in both high-top and low-top models for the Northern Hemisphere in which the pressure anomalies in RCP 8.5 have a higher magnitude at all altitudes than they do in RCP 4.5. This might suggest that a higher radiative forcing is consistent with a stronger tropospheric amplification effect, but for that to be more certain, natural variability would need to be eliminated. Additional simulations could be run to investigate specific changes in radiative forcing, such as to stratospheric ozone, which would further refine the conclusion here by studying the different components which can cause higher radiative forcing. Maycock (2016) noted that with the decline in ozone-depleting substances, ozone levels are expected to return to pre-1980 levels, with this increase offsetting some of the stratospheric cooling due to increasing CO_2 during the next century. (In models with interactive chemistry, ozone recovery offsets 50% of cooling in RCP 4.5, and 20% of cooling in RCP 8.5.) Maycock (2016) also discovered that models which do not include interactive chemistry have ozone trends imposed
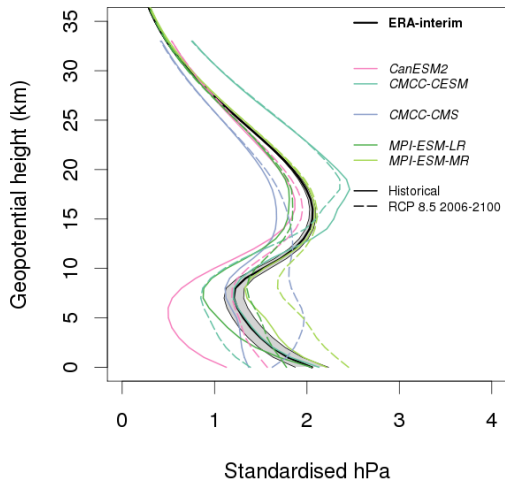
(a) Northern Hemisphere (DJFM)
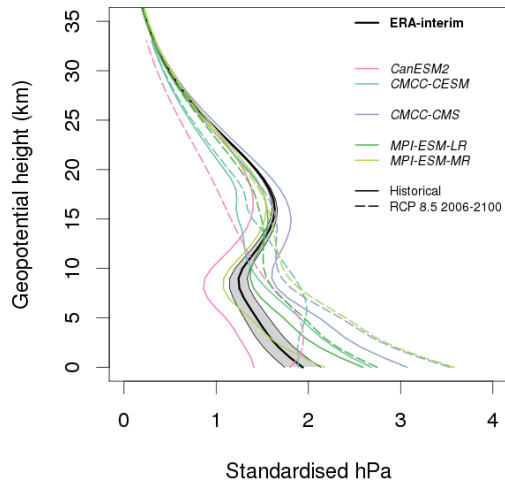
(b) Southern Hemisphere (ASON)
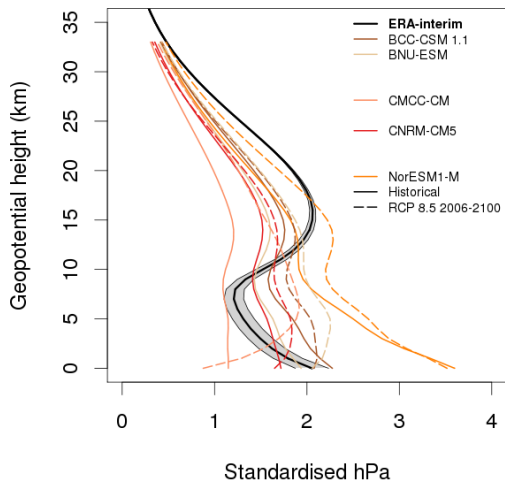
(c) Northern Hemisphere (DJFM)
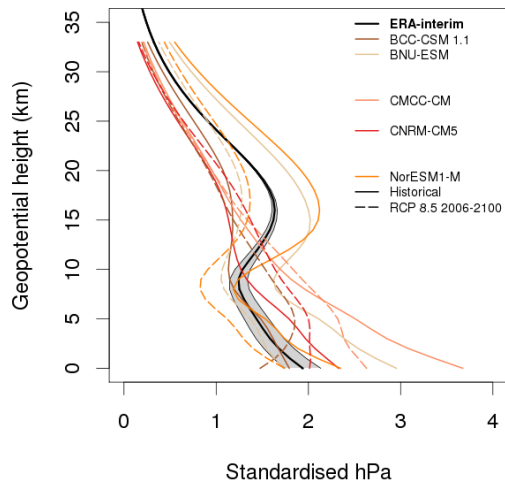
(d) Southern Hemisphere (ASON)
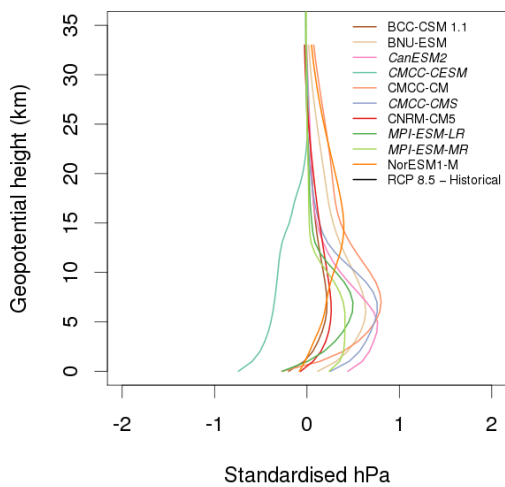
(e) Northern Hemisphere (DJFM)
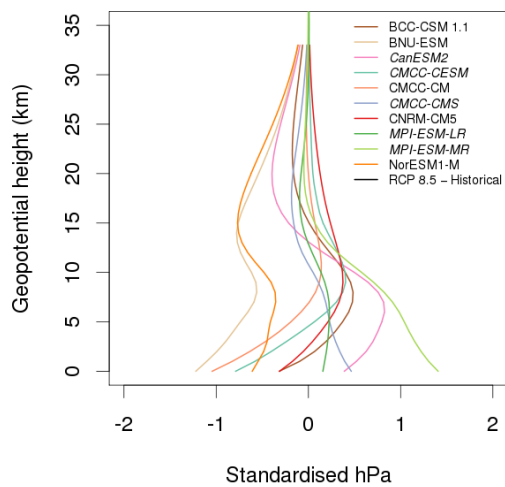
(f) Southern Hemisphere (ASON)

Figure 5.10: **(a,b,c,d)** Wintertime pressure slope estimates β_1 obtained by regression on standardised pressure at 25 km, showing curves for ERA-interim (thick black), 9 CMIP5 historical simulations (solid colour), and 9 RCP 8.5 simulations (dashed colour). ERA-interim shows a 95% pointwise confidence band. **(e,f)** Difference between RCP 8.5 and historical curves for each of the 9 models. 85
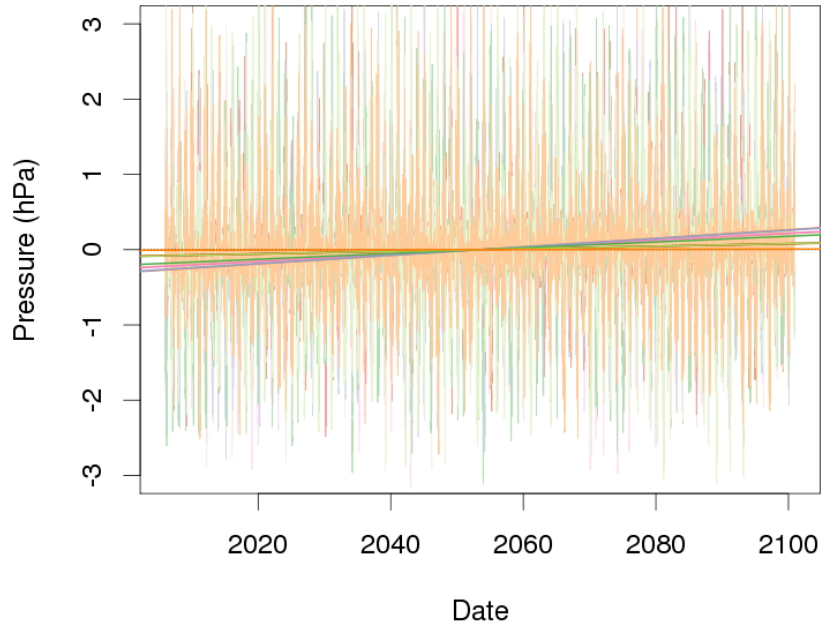
Figure 5.11: Long-term trend of each model, taken over the Northern Hemisphere polar cap at 25 km, RCP 4.5. Faded curves are the time series of each model; solid lines are the averaged trend of those time series.

which cause anomalous warming in the upper stratosphere and cooling in the lower stratosphere in RCP 4.5 experiments. Since that includes the majority of models here, and the ones which do include interactive chemistry are all low-top models, any additional simulations designed to investigate other radiative forcings, particularly those involving ozone, would need to use different models.

While they do all recreate the tropospheric amplification effect quite well in their historical simulations (Section 5.2), none of the high-top models show the 16 km peak or the 7 km tropopause in the Southern Hemisphere in their RCP simulations (Figs. 5.8b, 5.8d, 5.10b, 5.10d). However they do have points at around 15 km and 9 km where the gradient of the curve changes. This could indicate a change in the atmospheric system in which the phenomenon will no longer occur in the Southern Hemisphere with the same effects, or it could be an indication that the models themselves do not have sufficient information to project future S-T coupling efficiently.

Per Section 3.2, the annual cycle is removed before any further investigations take place. Since this is taken as an average over the entire data set, any long-term
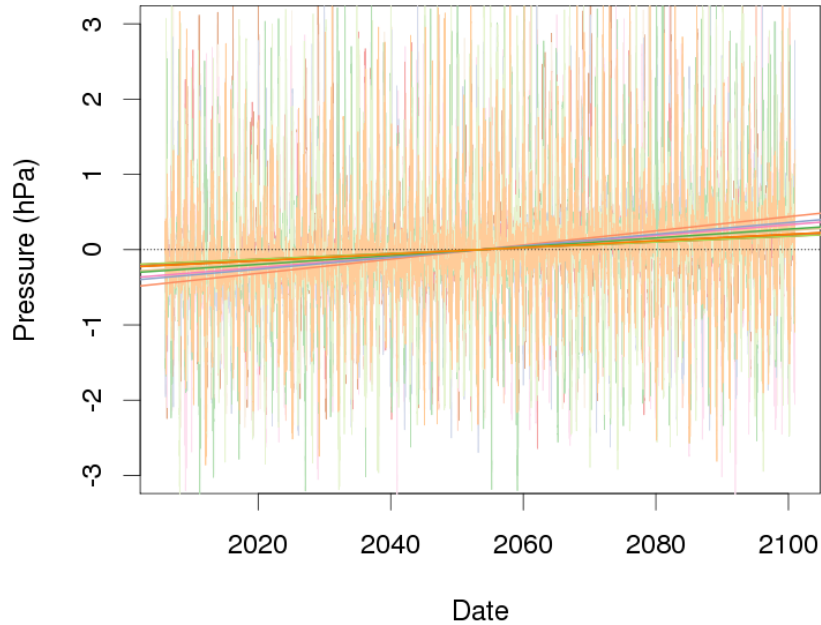
Figure 5.12: Long-term trend of each model, taken over the Northern Hemisphere polar cap at 25 km, RCP 8.5. Faded curves are the time series of each model; solid lines are the averaged trend of those time series.

trend in the data will be left behind, and can be plotted as a 'best-fit' line on the time series of the anomalies. Figure 5.11 shows the long-term (100 year) trend of polar cap pressure for each model in RCP 4.5, taken at 25 km. There is a slight positive trend across all models except NorESM1-M, but it appears too small to be significant. Figure 5.12 is the same plot but for the RCP 8.5 simulations, and suggests a more significant trend towards increased polar cap pressure across all the models over the next 100 years. Together, these plots imply that there is a general trend towards higher pressures, at least at this level, which is increased with a stronger radiative forcing difference. If this trend is removed from the regressions that produce Figures 5.8, 5.9 and 5.10, the plots of the RCP simulations move slightly closer to that of the model's historical curve, but the difference overall is not reduced by much. The only exception is for the Northern Hemisphere RCP 8.5 simulations, where the difference between RCP 8.5 and the historical simulations is much smaller after the trend is removed (Fig. 5.13). This implies that the majority of the difference shown in Figure 5.10e could be a direct result of the upward trend, but that this is not necessarily the case for the other simulations.
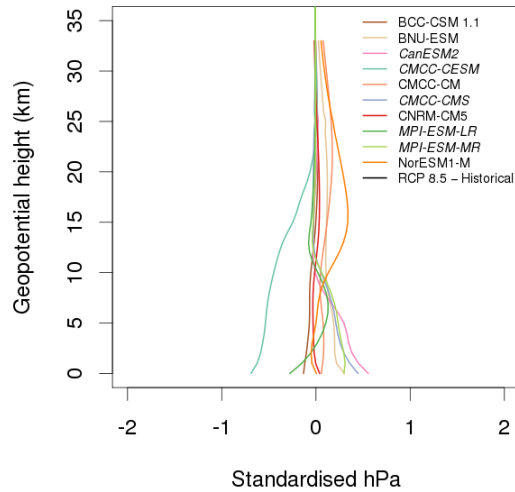
Figure 5.13: Difference between RCP 8.5 and historical curves for each of the models after the long-term trend (Fig. 5.12) is removed, Northern Hemisphere.

5.4 Summary

- High-top models, with a fully-resolved stratosphere, are better at recreating the tropospheric amplification phenomenon than low-top models.

- In the Northern Hemisphere, there is not much difference in magnitude between historical simulations from CMIP5 models and the future projections from RCP simulations in the same models.

- In the Southern Hemisphere, a number of models which recreated tropospheric amplification in their historical simulations do not develop a tropospheric amplification profile of a similar shape to that historical curve in their RCP simulations.

6 Climate models of varying complexity

6.1 Introduction

Taking any of the components of CMIP5 models, and either simplifying the calculation to reduce computing time, or completely parameterising its effects, results in a climate model which is faster to run, but less complex. These less-complex models are therefore less accurate, as certain atmospheric processes are ignored. This chapter investigates models of varying complexity, from a simple dynamical core model to a complex GCM, in an effort to determine which physical processes need to be resolved by the model in order to recreate tropospheric amplification. The aim is to infer which specific dynamical mechanisms are the drivers of tropospheric amplification in the atmosphere.

6.2 Dry Dynamical Core Model: GFDL-SDC

The effects of different model setups, involving different parameterisations, radiative cooling systems, and other factors, have been investigated in 35 perpetual January simulations (Jucker et al., 2014) from a version of the GFDL spectral dynamical core model (GFDL-SDC, Polvani and Kushner, 2002), which is forced by Newtonian cooling towards a prescribed temperature distribution. Newtonian cooling is an idealised radiative forcing scheme which represents the thermodynamics of the climate system as a relaxation of the temperature field back to the prescribed equilibrium, T_e, where T_e is a function of latitude and pressure. The Newtonian cooling term is defined as

$$Q = \frac{T - T_e}{\tau} \, ,$$

with equilibrium temperature T_e, absolute temperature T, and relaxation time τ, where T_e and τ are zonally symmetric (Polvani and Kushner, 2002; Jucker et al., 2013). The degree of cooling is therefore proportional to how far the temperature is from the equilibrium state. The model has a T42 spectral resolution (64 latitude measurements and 128 longitude measurements), and 40 vertical levels up to about
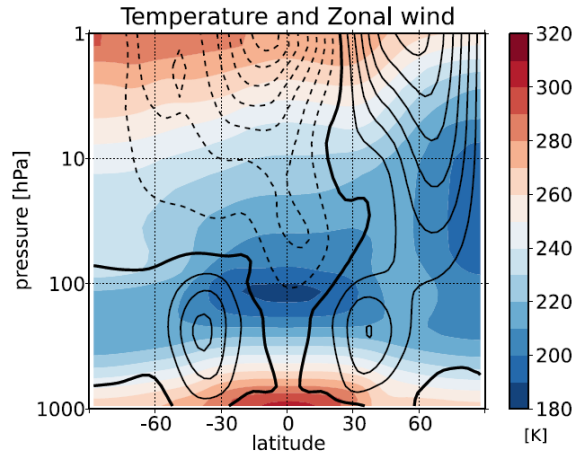
Figure 6.1: Dynamic temperature (colour) and zonal mean zonal wind (contours) for the GFDL-SDC perpetual January configuration. Contour interval is 10 ms^{-1}, solid lines denote positive, dashed lines denote negative, and thick lines denote zero values. (From Jucker et al., 2013, Fig. 6.)

0.01 hPa ($\sim$80 km). In this investigation, T_e and τ are determined by radiative transfer calculations above 100 hPa. For further details on the model setup, refer to Jucker et al. (2013).

The 'perpetual January' setup is used in order to get a higher number of winter stratospheric events, such as SSWs, than those which exist in the observational archives. As a result, these simulations have no annual cycle. Each run was configured with a different setup for: the height h and wave number N of 'topography' in the model, centred on 45°N, which provides orographic forcing; the amplitude A of the polar vortex, calculated as the difference in relaxation temperature between the winter pole and equinox conditions at 1 hPa; the relaxation time at the equator at 100 hPa, τ_t; and the relaxation time at high latitudes at 100 hPa, τ_p. The full details of each model run are summarised in Table H.1 and described in detail in Jucker et al. (2014). Each of the simulations was run for 10,000 days, following a spin-up of 2000 days. Jucker et al. (2014) state that the simulation with no orographic forcing is similar to Earth's Southern Hemisphere, while the simulations which do have orographic forcing are similar to the Northern Hemisphere. Figure 6.1 shows the zonal mean temperature (K, colour shading) and zonal mean zonal wind (contours, interval 10 ms^{-1}) for the perpetual January configuration. Jucker et al. (2013) noted the close similarity between this and the equivalent plot for ERA-interim (their Fig. 1, not shown here).

Figure 6.2: Profile of estimated β_1 for 35 dry dynamical core model perpetual January runs (detailed in Table H.1). ERA-interim is Northern Hemisphere wintertime with a 95% pointwise confidence band.

Figure 6.2 shows the β_1 profile for these 35 runs for the model's Northern Hemisphere. Apart from Run 1 (red), which is the simulation with no topography, the curves all have a similar shape to each other, none of which resemble the tropospheric amplification profile from ERA-interim. However, the shape is similar to the Northern Hemisphere 'summer' pattern of ERA-interim (Fig. 6.3), suggesting that there is a lack of a particular wintertime system or feature in this dry core model that is needed for tropospheric amplification. This is corroborated by the simulation with no topography; it alone does show a strong tropospheric signal, but at the same time does not show the stratospheric maximum or the tropopause minimum. In this respect, it is rather similar to the Southern Hemisphere 'summer' pattern of ERA-interim (Fig. 6.3). Figure 6.4 shows the estimates of β_1 for the model's Southern Hemisphere, which would be summertime given the model's configuration of perpetual January. The curves here are all very similar to each other, and are also similar to the curve of Southern Hemisphere summer in Figure 6.3. In summary, the curves of the GFDL-SDC runs are very similar to that of the summer plot in ERA-interim of the hemisphere that the run is designed to represent.

Table 6.1 shows the standard deviation σ of the p_{25} time series for each configuration of the model, and Table 6.2 shows the same for the four different seasonal patterns of ERA-interim (these are different from the values for σ shown in Table 4.2—0.805 and 0.603 hPa—as those are for the whole year, and not split by season). The Northern Hemisphere model runs have a lower standard deviation than Northern Hemisphere winter in ERA-interim, suggesting that there is a lack of variability in the model's stratosphere. The Southern Hemisphere model runs suggest a similar lack of variability, as the standard deviation is lower than Southern Hemisphere summer in ERA-interim. Model Run 1 in the Northern Hemisphere, which is stated to be similar to Earth's Southern Hemisphere in winter, also has a lower standard deviation than ERA-interim's Southern Hemisphere winter, and a higher one than Southern Hemisphere summer. This again suggests the model is lacking a particular system or feature that is needed to provide sufficient wintertime variability.

The polar vortex is an obvious choice for a missing system, and it is certainly
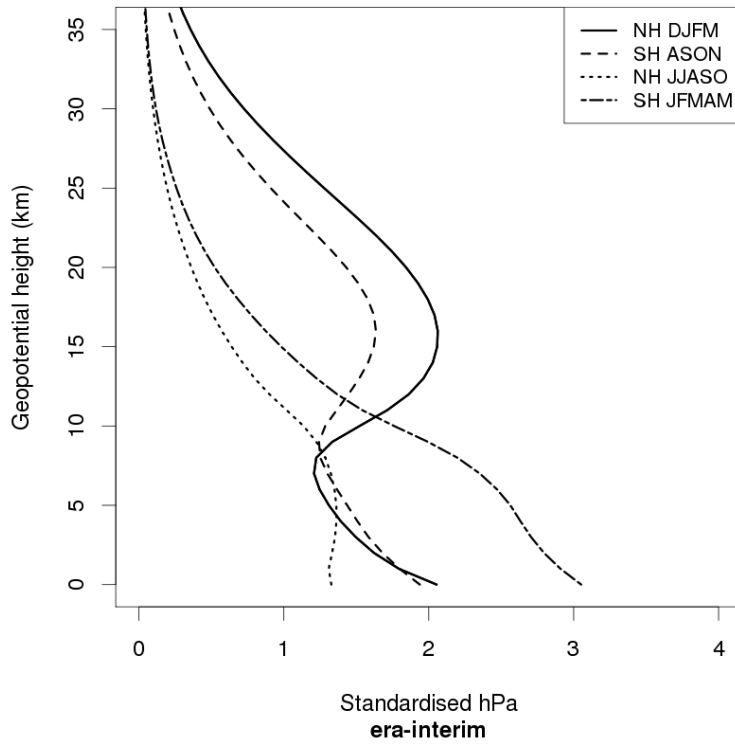
Figure 6.3: ERA-interim seasonal pressure slope estimates β_1 obtained by regression on standardised pressure at 25 km, showing NH winter, SH winter, NH summer, and SH summer.
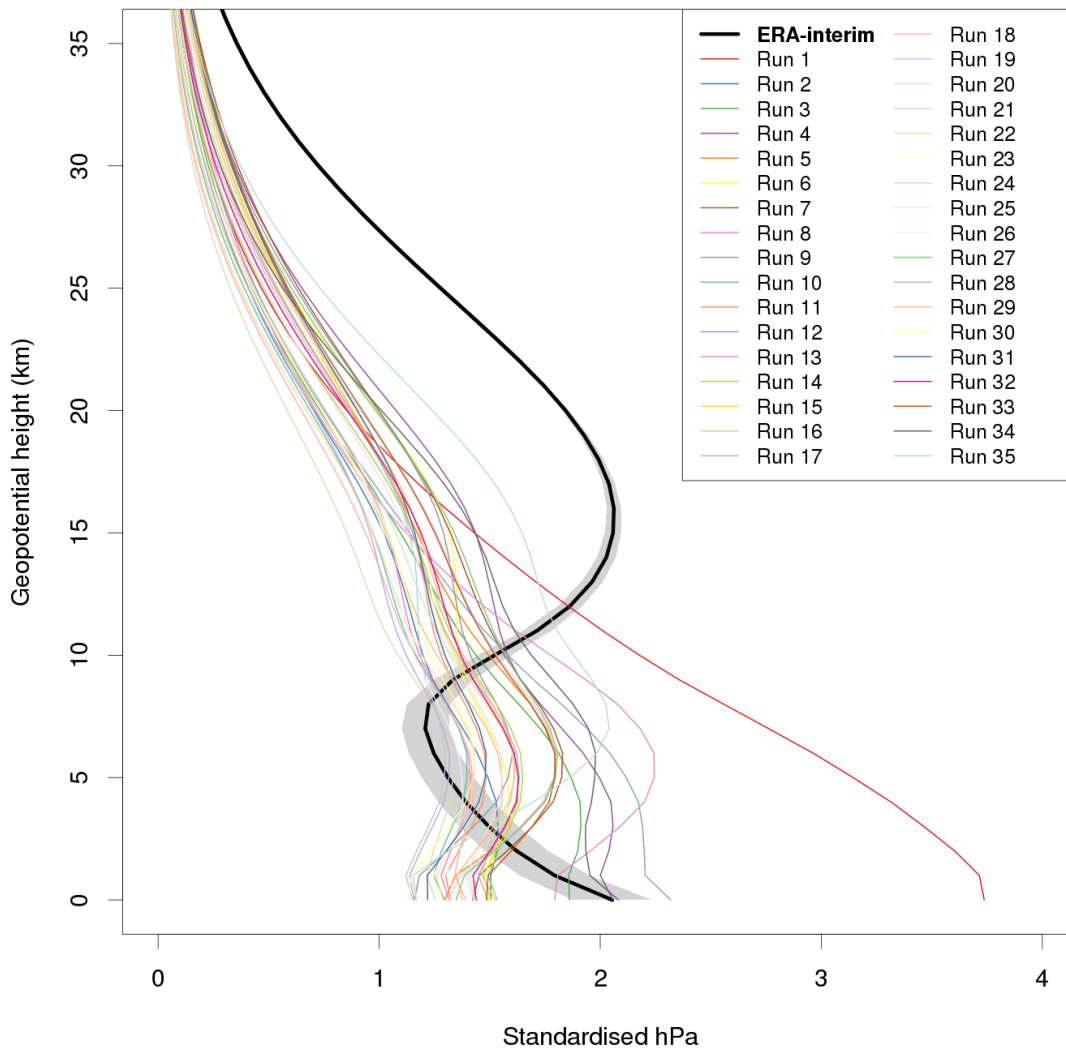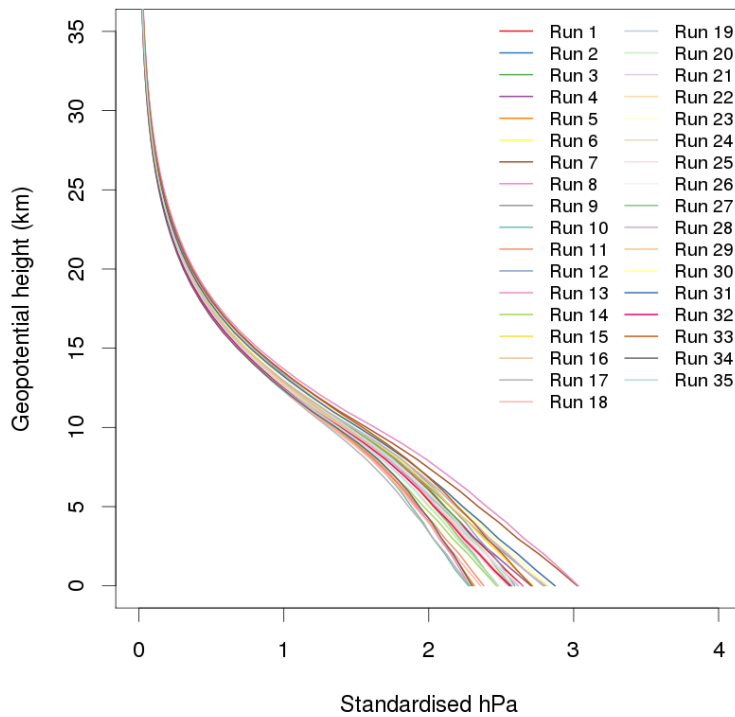

Figure 6.4: Profile of estimated β_1 for 35 dry dynamical core model perpetual January runs (detailed in Table H.1), Southern Hemisphere.

Table 6.1: Standard deviation σ (hPa) of the pressure time series at 25 km for 35 dry dynamical core model runs (detailed in Table H.1).

	Northern Hemisphere	Southern Hemisphere		Northern Hemisphere	Southern Hemisphere
Run 1	0.467	0.149	Run 19	0.519	0.140
Run 2	0.407	0.145	Run 20	0.434	0.151
Run 3	0.426	0.147	Run 21	0.557	0.148
Run 4	0.650	0.157	Run 22	0.369	0.141
Run 5	0.574	0.159	Run 23	0.552	0.150
Run 6	0.583	0.157	Run 24	0.326	0.143
Run 7	0.635	0.169	Run 25	0.480	0.137
Run 8	0.438	0.145	Run 26	0.428	0.145
Run 9	0.622	0.156	Run 27	0.603	0.150
Run 10	0.390	0.139	Run 28	0.412	0.151
Run 11	0.531	0.147	Run 29	0.569	0.155
Run 12	0.442	0.165	Run 30	0.430	0.158
Run 13	0.435	0.173	Run 31	0.580	0.157
Run 14	0.476	0.148	Run 32	0.503	0.141
Run 15	0.560	0.157	Run 33	0.587	0.164
Run 16	0.406	0.140	Run 34	0.565	0.138
Run 17	0.539	0.147	Run 35	0.732	0.150
Run 18	0.359	0.142			

Table 6.2: Standard deviation σ (hPa) of seasonal ERA-interim pressure time series at 25 km.

	Northern Hemisphere		Southern Hemisphere	
Winter	(DJFM)	1.278	(ASON)	0.909
Summer	(JJASO)	0.194	(JFMAM)	0.259

the case that many of these model runs have no polar vortex. However, even the simulations where the polar vortex exists (Runs 26–33, where $A > 0$) do not have a notable difference in the shape of the regression curve. The standard deviation of those runs is also similar to all the other runs. This implies that there are other factors not included in GFDL-SDC which would be needed for the curve profile to become closer to the tropospheric amplification profile of ERA-interim.

6.3 Model with Intermediate Complexity: MiMA

MiMA (Model of an idealised Moist Atmosphere, Jucker and Gerber, 2017) is a more complex model than GFDL-SDC which has a comprehensive radiation scheme (MiMA uses the Rapid Radiative Transfer Model, instead of Newtonian cooling; see Section 6.4), and includes prognostic moisture and an annual cycle. As with GFDL-SDC, its code is based on GFDL's Flexible Modelling System (FMS). MiMA is still considerably less complex than CMIP5-class models, and serves as a model of intermediate complexity.

Unfortunately the original data available from MiMA does not have daily data or geopotential height on each pressure level, immediately failing two of the four required criteria listed in Section 5.1. However, 5-day data was available, run for ten 360-day years, which included surface temperature T_s, surface pressure p_s, and geopotential height at the surface Z_s, as well as specific humidity q and temperature T on 80 vertical levels p up to 0.01 hPa ($\sim$80 km). After interpolating the data over time to generate daily values, the geopotential height field Z can be reconstructed from the available data and the hypsometric equation (4):

$$Z_2 - Z_1 = \frac{R_d \overline{T_v}}{g_0} \ln\left(\frac{p_1}{p_2}\right) \tag{4}$$

Here, $R_d = 287$ Jkg^{-1}K^{-1} is the dry air gas constant, $g \approx g_0 = 9.81$ ms^{-2}, and $\overline{T_v} = \dfrac{T_v(p_1) + T_v(p_2)}{2}$ is the mean virtual temperature T_v between layers p_1 and p_2, with $T_v = T(1 + q(\frac{1}{\epsilon} - 1)) = T(1 + 0.61q)$ where q is specific humidity.

Data from eighteen different model configurations were available, with each one having a different setup for: number ($\mathbf{M}$) and height ($\mathbf{O}$) of Northern Hemisphere
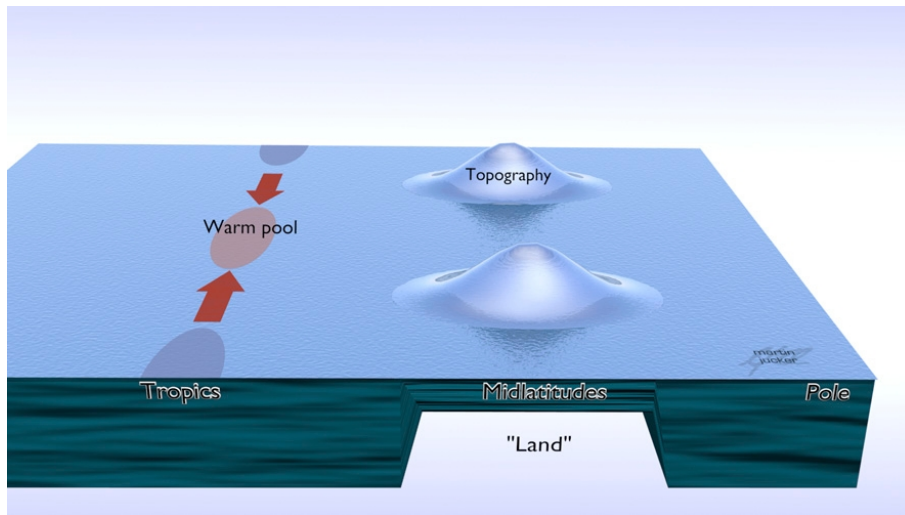
Figure 6.5: Illustration of the MiMA model setup, showing the warm pool, Gaussian topography, and 1 m 'land' region. (From Jucker and Gerber, 2017, Fig. 3.)

midlatitude Gaussian 'mountains', centred on 45°N latitude; depth of a Northern Hemisphere midlatitude 'land-like' shallow layer **L** between 40°N and 50°N; and amplitude of tropical zonal heat flux, generating a 'warm pool' region **W** of maximal sea surface temperatures. This setup is illustrated in Figure 6.5. The control run (CTRL) has a 100 m mixed layer 'slab ocean' with no topography, no land area, and no warm pool. When present, the midlatitude 'land' region simulates a land-sea contrast by using a significantly shallower mixed layer ocean region with a reduced heat capacity, rather than any actual land features. Figure 6.6 shows the DJF climatology of zonal mean temperature (K, colour shading) and zonal mean zonal wind (contours, interval 10 ms^{-1}) for the control run (CTRL) and a simulation with 4 km wave-1 topography and 1 m midlatitude 'land' (L01.O4M1). The control simulation has no annual cycle in the tropical tropopause layer, while the L01.O4M1 simulation is much more 'Earth-like', with an annual cycle comparable to that of the observed atmosphere. As with GFDL-SDC, these profiles are both similar to that of ERA-interim (not shown). Full details on the model setup are provided in Jucker and Gerber (2017).

Figure 6.7 is the regression plot of β_1 for the eighteen configurations of MiMA. There are four configurations which are much more similar to ERA-interim than the others – L01.O4M1 (blue), W30.L01.O4M1 (blue-grey), L01.O4M2 (green), and W30.L01.O4M2 (dark pink). A few of the remaining configurations, such
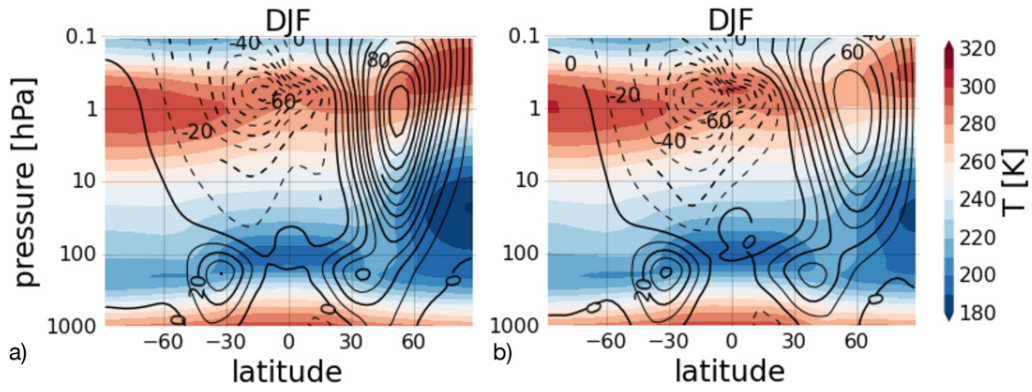
Figure 6.6: DJF dynamic temperature (colour) and zonal mean zonal wind (contours) for two MiMA configurations: **(a)** uniform slab ocean with mixed layer depth 100 m (CTRL); **(b)** simulation with 4 km wave-1 Gaussian topography and 1 m midlatitude 'land' (L01.O4M1). Contour interval is 10 ms^{-1}. (From Jucker and Gerber, 2017, Fig. 1.)

as L01 (purple) and W30.L01 (olive green), bear a resemblance to the Northern-Hemisphere-like curves of Figure 6.2, which makes sense as the models have the same basis in GFDL-FMS.

Figure 6.8 shows three panels with a subset of the curves from Figure 6.7, where each panel represents a single unchanged variable. 6.8a (**L01**) shows all the simulations with a midlatitude 'land' shallow layer of 1 m (the rest of the ocean remains at 100 m); 6.8b (**O4Mx**) shows all the runs with a Gaussian mountain height of 4 km (with x being 1 or 2 mountains, corresponding to topography wave number 1 or 2); and 6.8c (**W30**) shows all the simulations with a 'warm pool' zonal heat flux of 30 W/m^2.

Figure 6.8a shows four curves which are similar in profile to ERA-interim, and two which are not. Those curves which are similar all come from model configurations which include at least one Gaussian 'mountain' with height 4 km.

Figure 6.8b then shows *all* the curves from runs which include at least one Gaussian 'mountain' with height 4 km. The same four curves from 6.8a are present, alongside four other curves which are less similar to ERA-interim. Those curves which are less similar come from simulations which do not include a shallow 'land' feature. These two plots suggest that the presence of a Gaussian 'mountain' is a necessary but not sufficient factor to recreate the ERA-interim profile of tropospheric amplification.

Figure 6.8c shows six curves which each come from a model configuration includ-
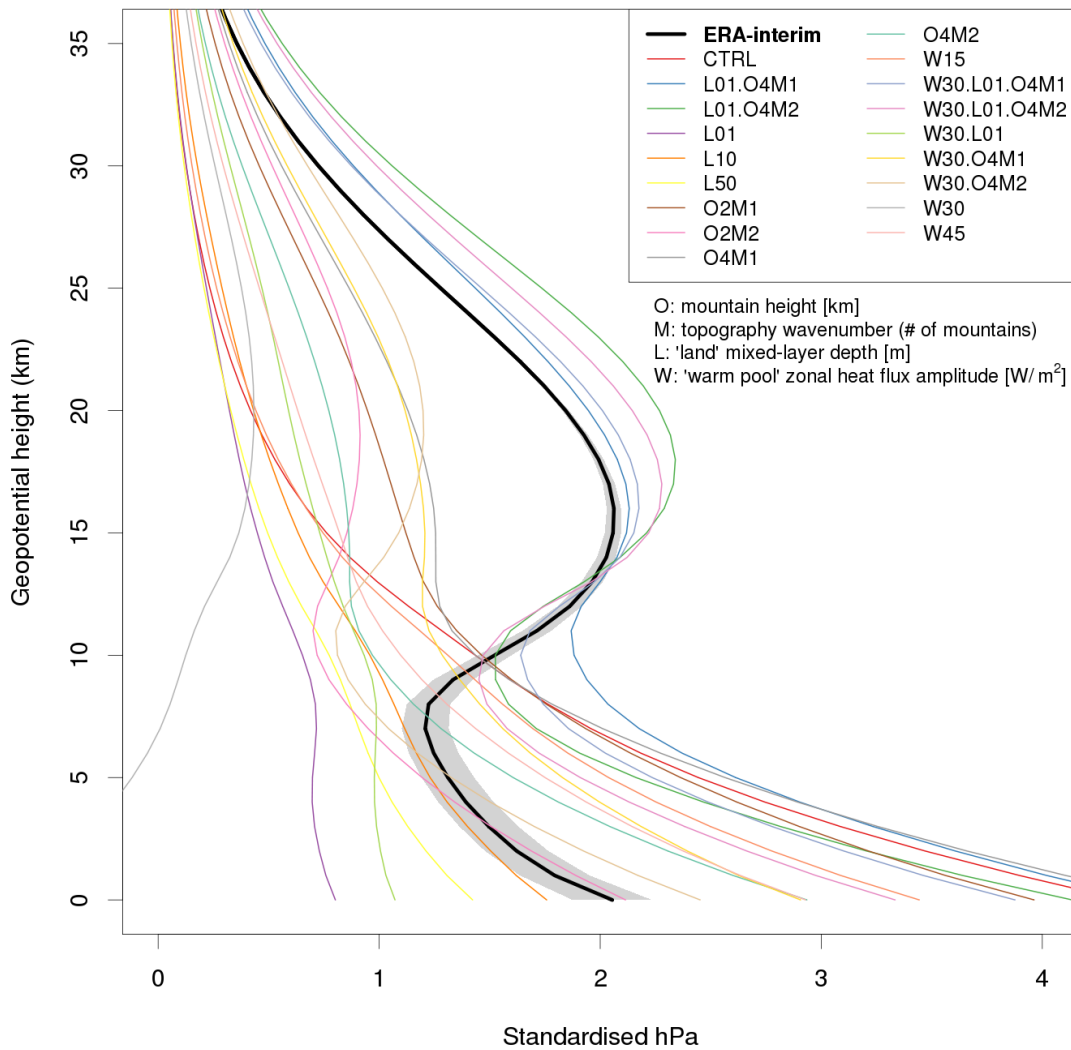
Figure 6.7: Profile of estimated β_1 for 18 MiMA model runs with varying configurations, showing Northern Hemisphere wintertime. ERA-interim is Northern Hemisphere wintertime with a 95% pointwise confidence band.
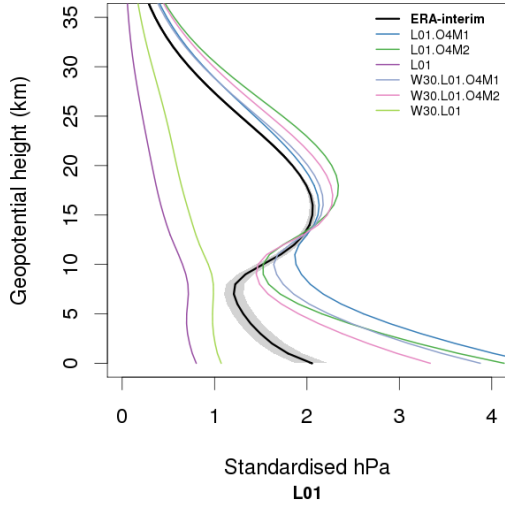
(a) 1 m 'land' section
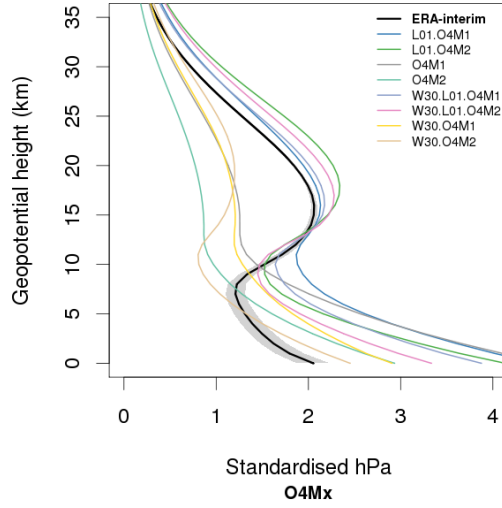
(b) 4 km Gaussian mountain topography
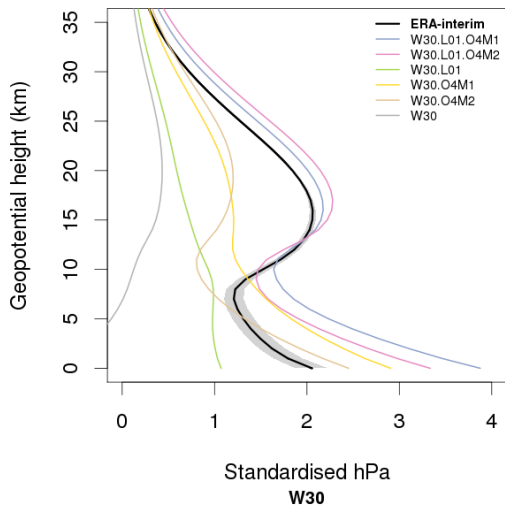
(c) 30 W/m² warm pool heat flux
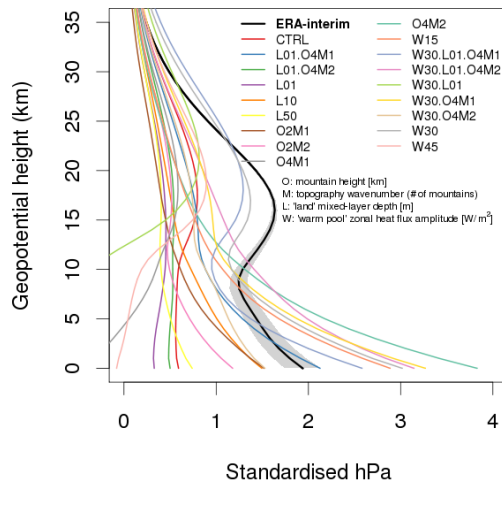
(d) Southern Hemisphere

Figure 6.8: Profile of estimated β_1 for: **(a,b,c)** MiMA model runs with specific configurations and ERA-interim, showing Northern Hemisphere wintertime; **(d)** all MiMA model runs and ERA-interim, showing Southern Hemisphere wintertime.

ing a 'warm pool' with zonal heat flux 30 W/m². The two curves which are most similar to ERA-interim have both a shallow 'land' region and at least one Gaussian 'mountain'. The curve with only a 'land' feature, W30.L01 (olive green), is more similar in profile shape to the majority of plots in Figure 6.2. The curve with two Gaussian 'mountains' and no land, W30.O4M2 (light brown), is similar in shape to ERA-interim, but does not have a similar magnitude; notably, the stratospheric maximum is much lower. Combined with the previous two plots, this implies that the presence of a shallow 'land' region and at least one Gaussian 'mountain' is sufficient to recreate the profile of tropospheric amplification in MiMA. Is is probable that the presence (or absence) of a 'land' feature alters the stationary wave pattern, thus affecting stratospheric driving through the wave-driven pump.

Each of the four curves which are similar to ERA-interim has a higher stratospheric peak, at around 18–20 km, and also a higher tropopause, around 10 km. This suggests that MiMA's troposphere is a bit too thick, and has pushed the stratospheric processes upwards. The amplification at the surface is also between 1.5 and 2.5 hPa higher than expected, which may be another indicator of a troposphere that is too active, or one that is too thick.

Figure 6.8d is the regression plot of β_1 for the eighteen configurations of MiMA in the Southern Hemisphere. Here, only one of the four simulations that was similar to ERA-interim in the Northern Hemisphere is also similar in the Southern Hemisphere; W30.L01.O4M1 (steel blue), which is the configuration with a 'warm pool' with zonal heat flux 30 W/m², a 'land' region, and one 4 km Gaussian 'mountain'. There is one other similar curve, W30 (light grey), which has a 'warm pool' but no land or topography. It can be inferred from this that while the model can reasonably recreate the profile of tropospheric amplification in the Northern Hemisphere, which can be attributed to topographical features, there is no obvious causal processes in the Southern Hemisphere. This may be a result of the fact that the 'land' region and Gaussian 'mountains' are both applied solely to the model's Northern Hemisphere, and the fact that circulation in the Southern Hemisphere is much more zonally symmetric.

Table 6.3: Standard deviation σ (hPa) of the pressure time series at 25 km for 18 MiMA model runs (wintertime).

	Northern Hemisphere	Southern Hemisphere		Northern Hemisphere	Southern Hemisphere
CTRL	0.234	0.604	O4M2	0.593	0.404
L01.O4M1	1.435	0.528	W15	0.265	0.418
L01.O4M2	1.736	0.428	W30.L01.O4M1	1.463	1.024
L01	0.219	0.329	W30.L01.O4M2	1.599	0.624
L10	0.289	0.357	W30.L01	0.470	0.743
L50	0.207	0.321	W30.O4M1	0.886	0.654
O2M1	0.719	0.272	W30.O4M2	1.014	0.550
O2M2	0.766	0.403	W30	0.377	0.970
O4M1	0.864	0.474	W45	0.458	0.695

Table 6.3 shows the standard deviation σ of the p_{25} time series for each configuration of the model, which can be compared with Table 6.2 for ERA-interim. Many of the Northern Hemisphere model configurations do not have sufficient stratospheric variability, but it is clear again that those which are closest to ERA-interim's Northern Hemisphere winter standard deviation of 1.278 are those which include a 'land' feature and a Gaussian 'mountain'. This therefore suggests that these features are required specifically to introduce sufficient stratospheric variability which can then lead to tropospheric amplification. In the Southern Hemisphere, it is again configurations W30.L01.O4M1 and W30 which are closest to ERA-interim's Southern Hemisphere winter standard deviation of 0.909, reinforcing the findings from Figure 6.8d.

6.4 Discussion and Extension

It has been shown that the presence of topography and land are very important factors in the development of tropospheric amplification in the Northern Hemisphere. It is prudent to note here that all but three of the GFDL-SDC configurations in Figure 6.2 also have wave 1 or 2 mountain(s) (at 3 km height), and that model does not recreate tropospheric amplification, so while topography is an essential component,

(a) Northern Hemisphere (DJFM) **(b)** Southern Hemisphere (ASON)
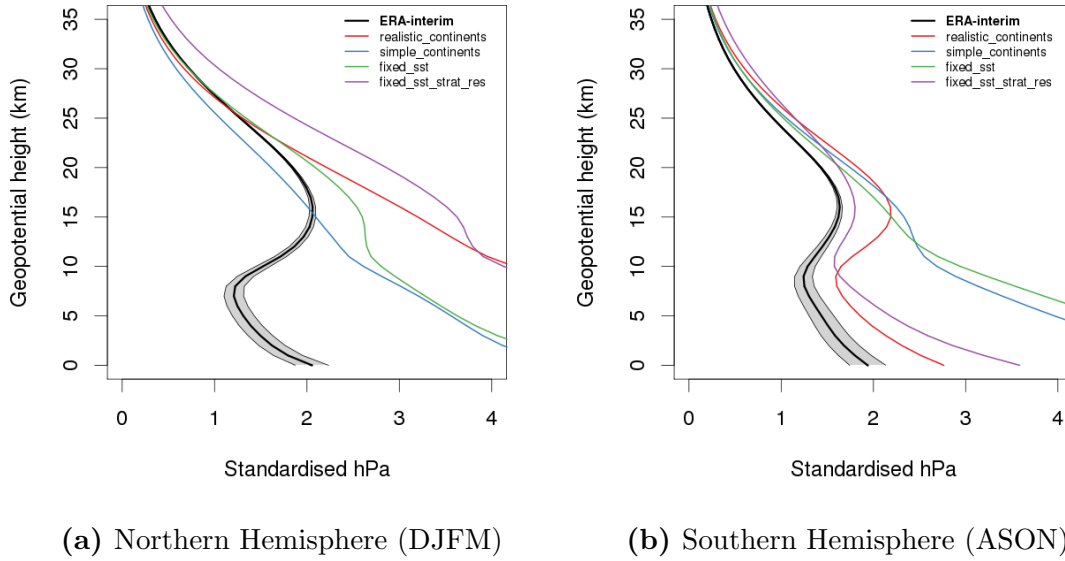
Figure 6.9: Profile of estimated β_1 for four MiMA model runs with different configurations for continent shape, sea surface temperature, and stratospheric resolution, showing Northern Hemisphere wintertime. ERA-interim is Northern Hemisphere wintertime with a 95% pointwise confidence band.

other aspects of MiMA that are not present in GFDL-SDC are also important. The primary difference here is the use of the Rapid Radiative Transfer Model (RRTM) for radiative cooling (Mlawer et al., 1997) instead of Newtonian cooling (Jucker et al., 2013). This includes parameterisations for carbon dioxide, ozone, and water vapour (among other factors), with ozone of particular importance here. The absorption of shortwave UV by ozone induces a meridional temperature gradient, which is one of the primary processes behind the formation of the winter polar vortex, and as discussed in Chapter 3, tropospheric amplification only happens when the polar vortex is present. While GFDL-SDC does include polar vortex parameterisations as well, those based on Newtonian cooling are insufficient to reproduce tropospheric amplification. This may imply the relevance of another factor of RRTM – the inclusion of moisture in the model, in the form of water vapour. GFDL-SDC, conversely, has a dry atmosphere.

Figure 6.9 shows the β_1 profiles for four model runs from an extended version of MiMA, which has numerous additional configuration options, including continents, evaporative resistance over land (which simulates the effect of a limited water supply), and q-flux-based sea surface temperatures. 'Realistic continents' (9720 days)

has a topographical setup that is similar to the real-world continent distribution, including a higher polar albedo; 'simple continents' (7200 days) has a simplified continental shape and topographical distribution that exists to introduce topography to the model, but is only somewhat comparable to the real world; 'fixed sst' (7200 days) is the same simple continent layout, but with sea surface temperatures prescribed rather than variable; and 'fixed sst strat res' (7200 days) is the same again, but with a higher resolution in the stratosphere (and, consequently, a lower resolution in the troposphere).

Some of these configurations do appear to recreate the expected shape of the tropospheric amplification anomaly for the Southern Hemisphere; most notable is the curve of the realistic continents run. However, in the Northern Hemisphere, there's no indication that the realistic continents setup has helped recreate the phenomenon. Overall, these extended simulations seem to be able to produce the expected shape in the Southern Hemisphere, to some degree, in all four configurations. After realistic continents, the high-res stratosphere 'fixed sst strat res' curve is closest, and is much more so than the standard 'fixed sst' curve. This again reinforces the theory that a better-resolved stratosphere is needed to identify S-T coupling events.

The other curves in the Southern Hemisphere, and all of the configurations for the Northern Hemisphere, do not seem to have been able to recreate the *expected* shape of tropospheric amplification at all, but they do all suggest a major increase in pressure at the surface, but of more than double the standard 2 hPa and without a drop-off at the tropopause. This is different to the slight drop in pressure seen in the Northern Hemisphere summer (Fig. 6.3, dotted) and the GFDL-SDC model (Fig. 6.2), and also very different to the base theories of the Rossby wave pump (Fig. 3.1a–c). There is a slight similarity between these curves and the regression for ERA-interim's Southern Hemisphere summer (Fig. 6.3, dot-dash), and they are also reminiscent of the plots produced when the regression is taken from lower down in the atmosphere (∼15 km or below, not shown). This could suggest that the tropospheric processes in this configuration are extending too high into the atmosphere, or that the tropopause itself may be too high. Alternatively, it could

be an indication that the effects of the polar vortex in the model are too strong, but given that there is no exploration of the polar vortex available here, this cannot be confirmed. To investigate polar vortex amplitude further, runs would be needed from configurations of MiMA which *do* show the full profile of tropospheric amplification, on which the polar vortex amplitude could be adjusted.

Table 6.4: Standard deviation σ (hPa) of the pressure time series at 25 km for four extended MiMA model runs (wintertime).

	Northern Hemisphere	Southern Hemisphere
realistic continents	1.303	1.142
simple continents	1.058	1.057
fixed sst	1.342	1.022
fixed sst strat res	1.863	1.149

Table 6.4 shows the standard deviation σ of the p_{25} time series for each configuration of the extended MiMA model. The stratospheric variability in these configurations is higher than ERA-interim for the Southern Hemisphere, and also for three of the four configurations in the Northern Hemisphere. Variability in the simple continents configuration is slightly lower, while variation in the high-res stratosphere configuration is much higher, which could be another indication of an over-active troposphere.

Overall, MiMA appears to be able to reproduce the tropospheric amplification profile, but it is very dependent on the configuration used. The extended version of MiMA does not appear to be consistent; with additional runs and additional configurations tested, a more stable conclusion could be developed, and it would be interesting to vary the topography of the extended version back towards the configuration in L01.O4M2 to see where the extended version falls short.

6.5   Summary

- The dry dynamical core model GFDL-SDC is not able to recreate the profile of tropospheric amplification; even though ostensibly designed to represent winter, the profiles look like the equivalent summer in ERA-interim.

- Certain configurations of the intermediate-complexity model MiMA are able to recreate the tropospheric amplification profile, but this is very dependent on the setup used.

- It can therefore be inferred that moisture is required in the model in order for tropospheric amplification to be observed.

- The presence of land and topography in the model setup are important in the development of the tropospheric amplification profile in the Northern Hemisphere, as they result in increased stratospheric variability.

7 Contribution of the zonal mean and baroclinic eddy components of meridional polar cap mass flux

7.1 Introduction

In this chapter, the mass fluxes will be further investigated in order to assess the contribution of the zonal mean and eddy components of the meridional flow, and the contribution of both vertical and horizontal mass flux on the resulting change in pressure.

The equations of hydrostatic balance and mass continuity will be used to better indicate what the pressure plots of Chapters 4–5 are showing. Based on quasi-geostrophic (QG) theory, the zonal mean meridional wind $[v] \sim 0$, so it should also be possible to determine whether tropospheric amplification follows the QG theory, or is partially ageostrophic. The last section then describes regional mass changes instead of zonal mean flow. This should give a clear indication of where on the 65° parallel mass is flowing into the polar cap, and where it is flowing out.

7.2 Relationship between mass flux and pressure tendency

The relationship between mass flux and pressure change can be derived from the equations of hydrostatic balance,

$$\frac{\partial p}{\partial z} = -\rho g \ , \tag{5}$$

and mass continuity,

$$\frac{\partial \rho}{\partial t} + \nabla_H \cdot (\underline{\mathbf{u}}\rho) + \frac{\partial}{\partial z}(w\rho) = 0 \ . \tag{6}$$

By rearranging Equation 5,

$$\rho = -\frac{1}{g}\frac{\partial p}{\partial z} \ ,$$

and therefore, assuming constant g and using the shallow atmosphere approximations (Thuburn and White, 2012),

$$\frac{\partial \rho}{\partial t} = \frac{\partial}{\partial t}\left(-\frac{1}{g}\frac{\partial p}{\partial z}\right) = -\frac{1}{g}\frac{\partial^2 p}{\partial t \partial z} \ . \tag{7}$$

By substituting (7) into (6),

$$-\frac{1}{g}\frac{\partial^2 p}{\partial t \partial z} = -\nabla \cdot (\rho \underline{\mathbf{u}}) - \frac{\partial}{\partial z}(\rho w) \ . \tag{8}$$

Let $A = \int_A \mathrm{d}A$ be the area of the polar cap,

$$A = \int_A \mathrm{d}A = \int_{\phi_0}^{\frac{\pi}{2}} a \ \mathrm{d}\phi \int_0^{2\pi} \mathrm{d}\lambda \ a \cos(\phi) = 2\pi a^2 (1 - \sin(\phi_0)) \ , \tag{9}$$

where $a = 6371$ km is the mean radius of the Earth, and $\phi_0 = 65°$ is the latitude of the edge of the polar cap. Then let $\hat{p}$ be average polar cap pressure at a fixed height,

$$\hat{p} = \frac{\int p \ \mathrm{d}A}{A} \ . \tag{10}$$

Integrating Equation 8 with respect to z and A,

$$\left[\frac{\partial}{\partial t}\int_A p \ \mathrm{d}A\right]_{z_1}^{z_2} = \int_{z_1}^{z_2}\int_A \mathrm{d}A \left(g\nabla \cdot (\rho\underline{\mathbf{u}}) + g\frac{\partial}{\partial z}(\rho w)\right) \mathrm{d}z \ ,$$

then using (9) and (10),

$$\left[\frac{\partial}{\partial t}\hat{p}A\right]_{z_1}^{z_2} = \int_{z_1}^{z_2}\int_A \mathrm{d}A \left(g\nabla \cdot (\rho\underline{\mathbf{u}}) + g\frac{\partial}{\partial z}(\rho w)\right) \mathrm{d}z \ . \tag{11}$$

Using the divergence theorem,

$$\int_A (\nabla \cdot \underline{\mathbf{F}}) \ \mathrm{d}A = \oint \underline{\mathbf{F}} \cdot \underline{\mathbf{n}} \ \mathrm{d}s \ , \tag{12}$$

with $\underline{\mathbf{F}} = \rho\underline{\mathbf{u}}$, and substituting in Equation 11,

$$\left[\frac{\partial}{\partial t}\hat{p}A\right]_{z_1}^{z_2} = \int_{z_1}^{z_2}\left(\oint g\rho\underline{\mathbf{u}} \cdot \underline{\mathbf{n}} \ \mathrm{d}s\right) \mathrm{d}z + g\int_A \mathrm{d}A \ [\rho w]_{z_1}^{z_2} \ .$$
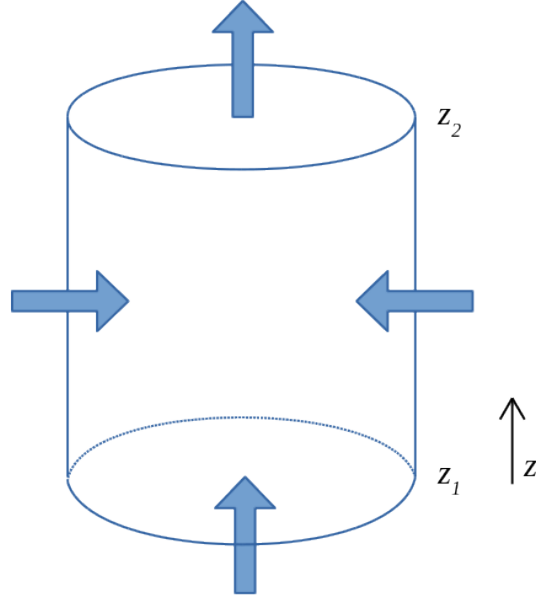
Figure 7.1: Diagram of horizontal and vertical mass movement into the column of air above the 'polar cap'.

This can be simplified to

$$\left[\frac{\partial \hat{p}}{\partial t}\right]_{z_1}^{z_2} = \frac{F}{A} + \frac{W}{A} \; , \tag{13}$$

where the horizontal mass flux

$$F = - \int_{z_1}^{z_2} \left(\int_0^{2\pi} g\rho va \cos(\phi)\mathrm{d}\lambda \right) \mathrm{d}z \; , \tag{14}$$

and the vertical mass flux

$$W = g \int_A \mathrm{d}A \; [\rho w]_{z_1}^{z_2} \; . \tag{15}$$

Equation 13 is the relationship between pressure and mass flux, showing that the change in polar cap pressure $\hat{p}$ over time is equal to the sum of the horizontal and vertical mass fluxes into the polar cap, $\frac{F}{A} + \frac{W}{A}$. This is illustrated in Figure 7.1.

From (14), F can be defined in terms of geopotential height z. The approximation $g \approx g_0 = 9.81$ assumes gravitational acceleration is constant with height from z_1 to z_2.

$$F = -\int_{z_1}^{z_2} dz \; 2\pi a g \cos(\phi)[\rho v]$$

$$= -a\cos(\phi) \int_{z_1}^{z_2} dz \int_0^{2\pi} d\lambda \; (\rho g v)$$

$$= -a\cos(\phi) \int_0^{2\pi} d\lambda \int_{z_1}^{z_2} dz \; (\rho g v)$$

$$g \approx g_0 \Rightarrow \int g \; dz \approx g \int dz$$

$$\Rightarrow F = -ag\cos(\phi) \int_0^{2\pi} d\lambda \int_{z_1}^{z_2} (\rho v) dz$$

$$\approx -ag\cos(\phi) \int_0^{2\pi} d\lambda \sum_{k=z_1}^{z_2} (\rho v)_k \, \Delta z_k$$

$$= -2\pi a g \cos(\phi) \sum_{k=z_1}^{z_2} [\rho v]_k \, \Delta z_k$$

The integrals are approximated as summations using the available data grid points.

From (15), W can be defined using a polar cap average, similar to polar cap pressure $\hat{p}$:

$$W = g \int_{\phi_0}^{\frac{\pi}{2}} a \; d\phi \int_0^{2\pi} d\lambda \; a \cos \phi \left(\rho w|_{z_2} - \rho w|_{z_1} \right)$$

$$= g \int_{\phi_0}^{\frac{\pi}{2}} a \; d\phi \; 2\pi a \cos(\phi) \left([\rho w]_{z_2} - [\rho w]_{z_1} \right)$$

$$= 2\pi a^2 g (1 - \sin(\phi_0)) \left([\hat{\rho w}]_{z_2} - [\hat{\rho w}]_{z_1} \right)$$

Equation 13 could be integrated over time, to reduce some of the natural variability in the data, or the pressure change over time could be found using finite differences; either way, an equation exists where change in polar cap pressure $\hat{p}$ is theoretically proportional to mass flux, $\frac{F+W}{A}$. Using data from ERA-interim, an investigation can be done to see how closely these values agree.

Figure 7.2 shows $\frac{\partial \hat{p}}{\partial t}$ and $\frac{F}{A}$ at the surface for the winter of 1998–1999. The vertical integral is taken over the entire atmospheric column, and as such, $W \approx 0$ and $\left[\frac{\partial \hat{p}}{\partial t}\right] \approx \frac{F}{A}$. This is reflected in the plot, which shows that the two curves have a similar magnitude, and many of the peaks and troughs coincide.
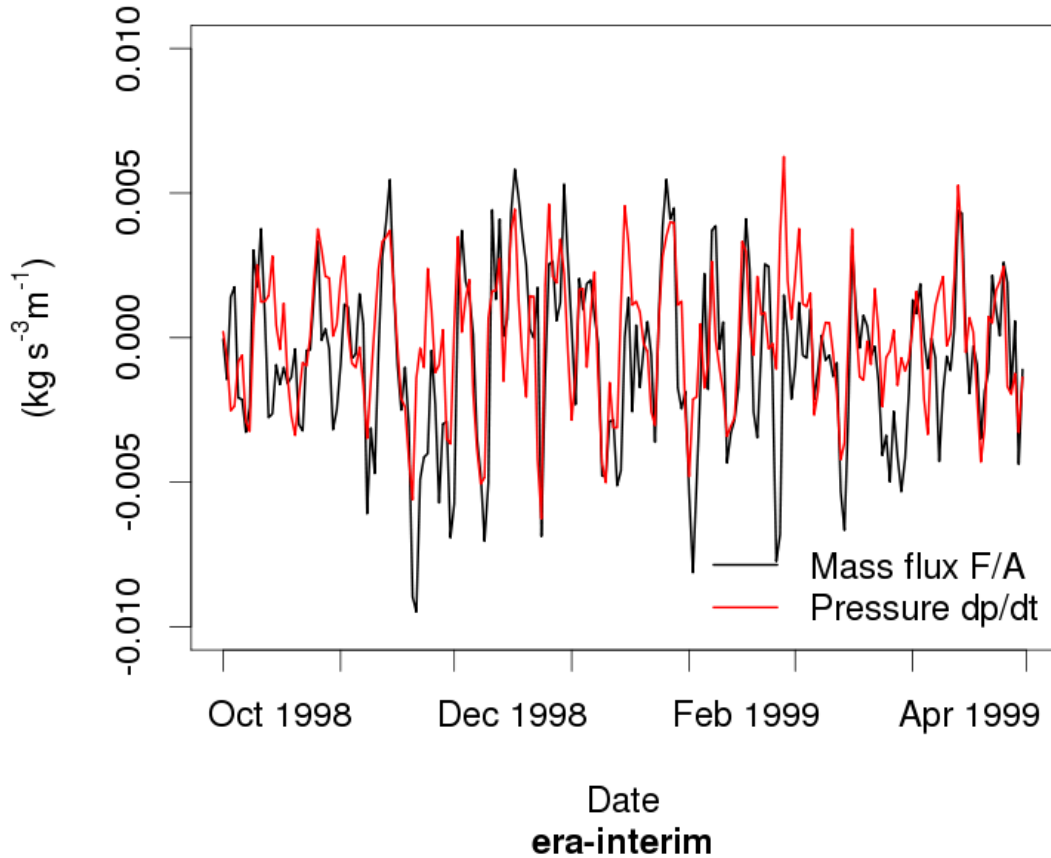
Figure 7.2: Surface mass flux at $\phi = 66°$N, boreal winter 1998–1999. Vertical integral taken over the entire atmospheric column.

Figure 7.3 shows $\frac{\partial \hat{p}}{\partial t}$ (7.3a), $\frac{F+W}{A}$ (7.3b), and $\frac{F}{A}$ and $\frac{W}{A}$ (7.3c) integrated over 12–25 km for the winter of 1998–1999. It is clear that $\frac{F+W}{A}$ does not closely follow $\frac{\partial \hat{p}}{\partial t}$, but the magnitudes of the two curves are comparable, and certain peaks and troughs do occur in similar places. A notable effect in Figure 7.3c is that the horizontal component F is almost completely cancelled by the vertical component W, which implies that mass flux in and out of the polar cap region across the 66° parallel is mostly balanced by the vertical mass flux into and out of the 12–25 km chunk from above and below. This also explains why $\frac{F+W}{A}$, being the difference of two large values, does not match $\frac{\partial \hat{p}}{\partial t}$ very closely.

Figure 3.5 previously showed two periods of anomalously positive stratospheric pressure in this time period; one running from mid-December to early January, and the other encompassing the first half of March. There are no clear mass flux peaks in Figures 7.3a or 7.3b that these events correspond to, and a large positive mass

flux would be needed to generate the positive pressure change seen in Figure 3.5.

The comparison can be repeated for the Southern Hemisphere, although in this case, the sign of F is reversed. Figure 7.4 shows the mass flux and pressure change for the 2002 winter, which is known for having a major SSW occur, and thus a large positive pressure anomaly. This period does have a notable continued high magnitude of $\frac{F}{A}$, but it is also opposed by $\frac{W}{A}$. Figure 7.4b shows a large negative value of $\frac{F+W}{A}$ at the start of September, and is generally more negative than positive throughout the winter period.

It is clear through both of these winter periods that the magnitude of the mass flux throughout the 12–25 km region is very small, at less than $|0.002|\ \mathrm{kg \cdot s^{-3} \cdot m^{-1}}$, or $|0.002|\ \mathrm{Pa \cdot s^{-1}}$. This makes it difficult to distinguish any influential mass flux, which leads to tropospheric amplification, from the natural variability of the system and other anomalies. This suggests that another approach may be needed, or that a different dataset should be used; notably, mass conservation within ERA-interim is not very good, which may affect the outcome.

Figures 7.5 and 7.6 show the same as Figures 7.3 and 7.4, but for the NCEP-DOE reanalysis instead of ERA-interim. Immediately noticeable in Figures 7.5c and 7.6c are the major peaks and troughs in the curves of NCEP-DOE which match those of ERA-interim; a positive $\frac{F}{A}$ mirroring a negative $\frac{W}{A}$ in early December 1998, immediately preceding an opposite state which persists until mid-January (Figs. 7.3c and 7.5c), and a low, wide peak/trough pair in December 2002 (Figs. 7.4c and 7.6c) are just two examples. It was show previously in Chapter 4 that ERA-interim and NCEP-DOE are very similar when pressure is considered, and this is reinforced by Figures 7.5a and 7.6a, which are themselves very similar to Figures 7.3a and 7.4a respectively, which show $\frac{\partial \hat{p}}{\partial t}$. The remaining plots, of $\frac{F+W}{A}$, are also similar to each other, but not as closely as $\frac{\partial \hat{p}}{\partial t}$, as while the major peaks and troughs coincide, the intermediate variability does not. This reinforces the conclusion above, that the influential mass flux is difficult to distinguish given that its magnitude is small, but does suggest that major events can still be identified.
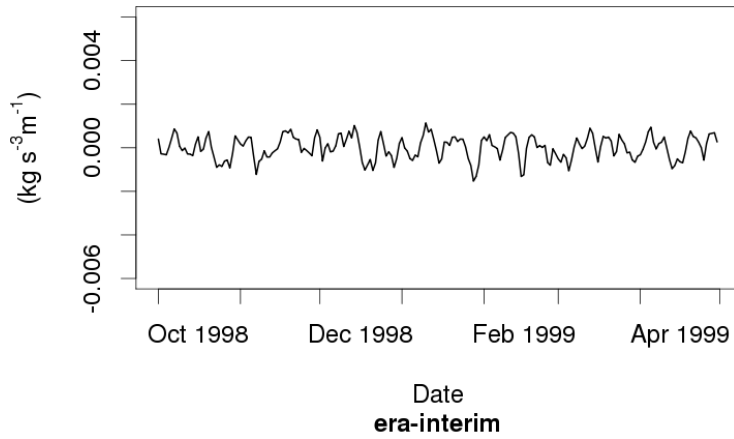
(a) Polar cap pressure change $\frac{\partial \hat{p}}{\partial t}$
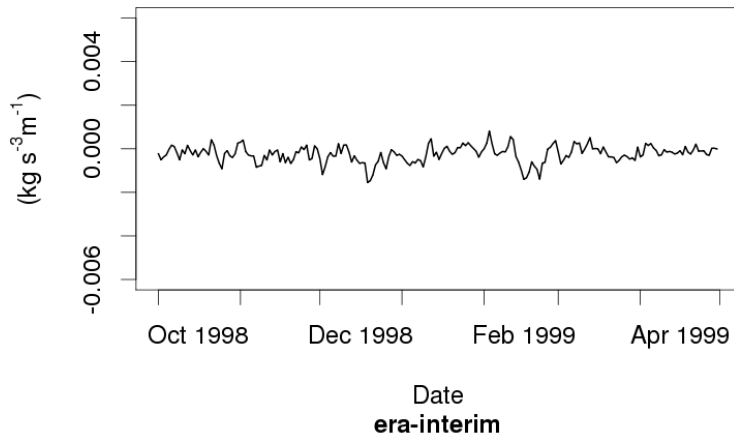
(b) Total mass flux $\frac{F+W}{A}$
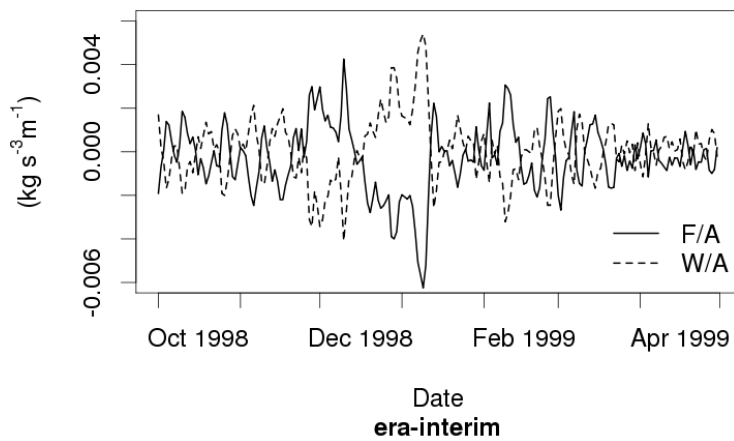
(c) Horizontal mass flux $\frac{F}{A}$ and vertical mass flux $\frac{W}{A}$

Figure 7.3: Mass flux in the 12–25 km region at $\phi = 66°N$, boreal winter 1998–1999 (ERA-interim).

(a) Polar cap pressure change $\frac{\partial \hat{p}}{\partial t}$

(b) Total mass flux $\frac{F+W}{A}$

(c) Horizontal mass flux $\frac{F}{A}$ and vertical mass flux $\frac{W}{A}$

Figure 7.4: Mass flux in the 12–25 km region at $\phi = 66°$N, austral winter 2002 (ERA-interim).

(a) Polar cap pressure change $\frac{\partial \hat{p}}{\partial t}$

(b) Total mass flux $\frac{F+W}{A}$
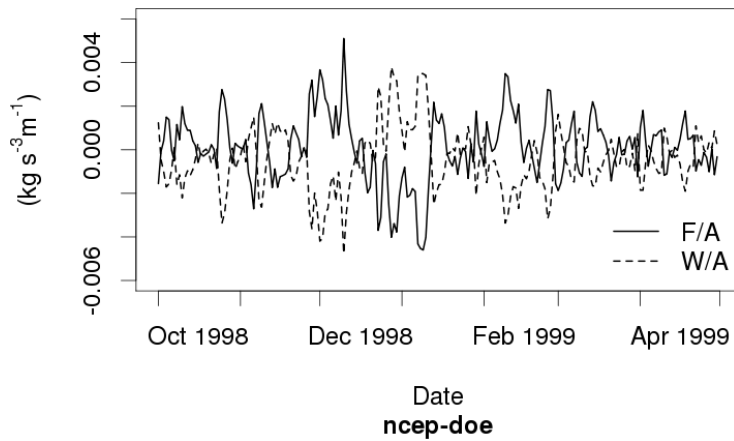
(c) Horizontal mass flux $\frac{F}{A}$ and vertical mass flux $\frac{W}{A}$

Figure 7.5: Mass flux in the 12–25 km region at $\phi = 66°$N, boreal winter 1998–1999 (NCEP-DOE).
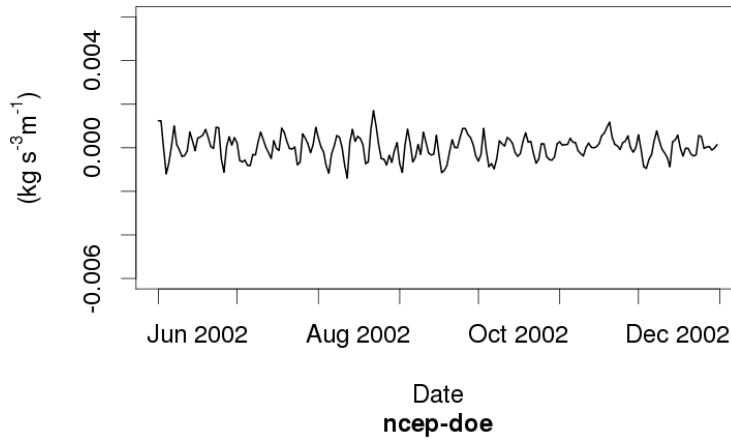
(a) Polar cap pressure change $\frac{\partial \hat{p}}{\partial t}$
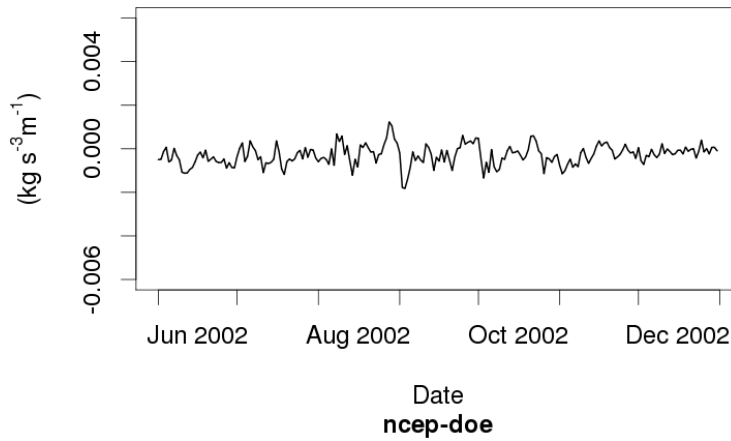
(b) Total mass flux $\frac{F+W}{A}$
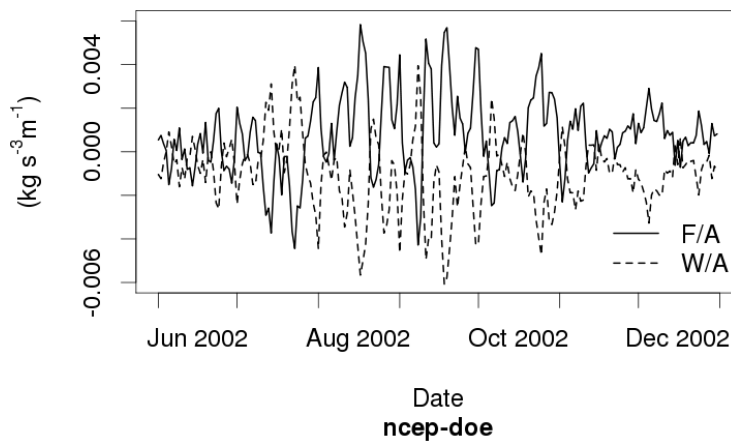
(c) Horizontal mass flux $\frac{F}{A}$ and vertical mass flux $\frac{W}{A}$

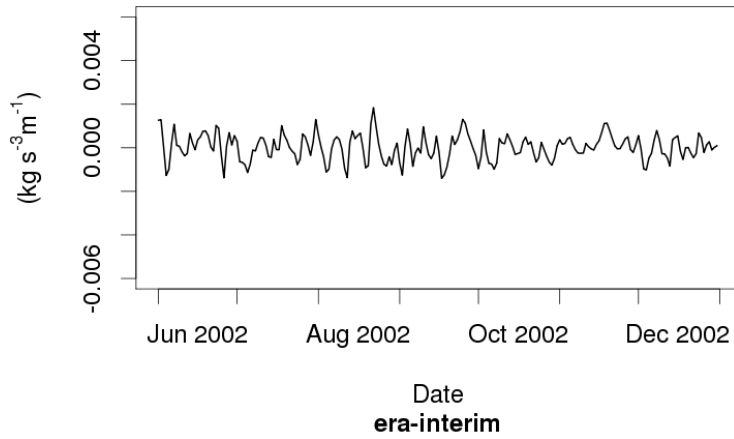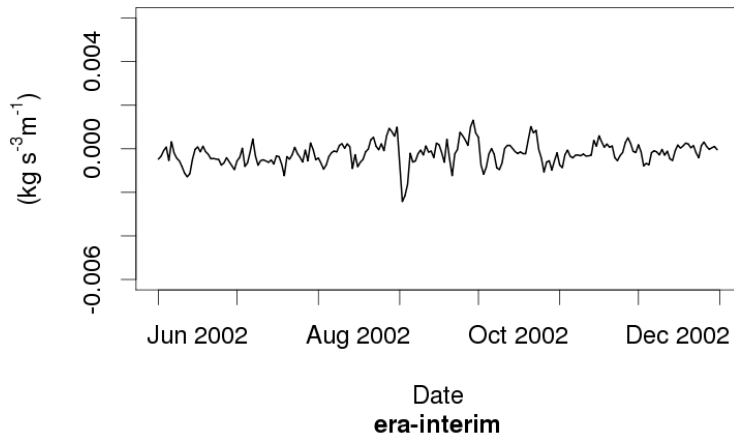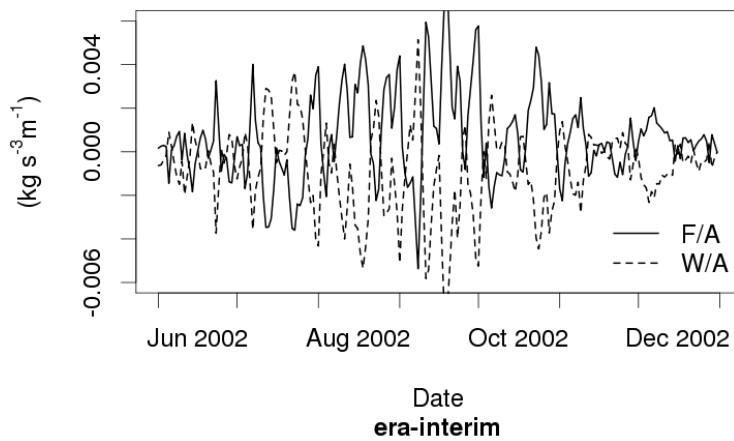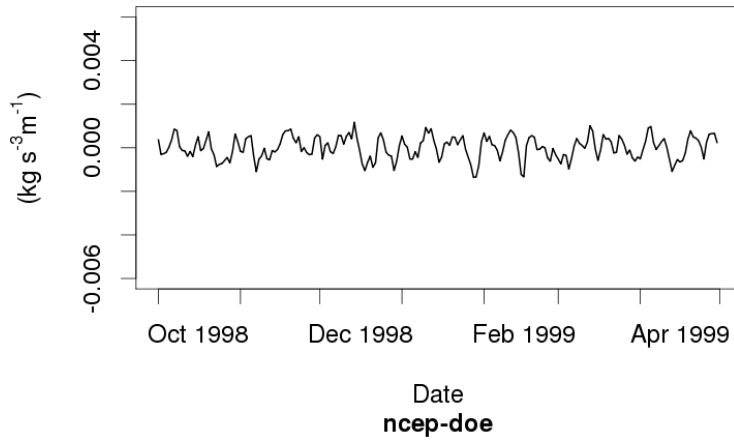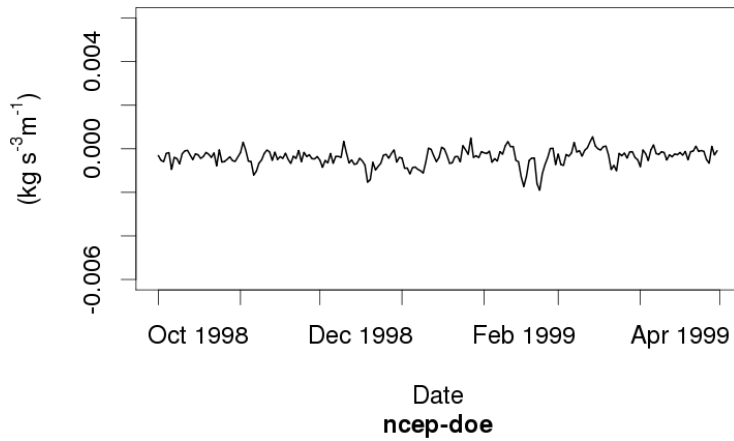**Figure 7.6:** Mass flux in the 12–25 km region at $\phi = 66°$N, austral winter 2002 (NCEP-DOE).

7.3   Horizontal Mass Flux

In this section, the longitudinal dependence of meridional mass flux will be considered, in an effort to determine whether there are particular regions with a recurring flow of mass in a particular direction, and examine whether polar cap mass flux as a whole is geostrophic in nature. This in turn could inform whether mass flux into and out of the polar cap occurs in regions with particular topography or a particular persistent atmospheric phenomenon. In order to see the greatest regional effect of mass flux, it is useful to identify days where that mass flux has the largest magnitude. In other words, maximal values of the total mass flux on the 66° parallel, $F_{66} = \rho\mathbf{v}$, with density ρ_{66} at 66°, and meridional velocity $\mathbf{v}_{66}$ across 66°.

Figure 7.7a shows the total meridional mass flux $[\rho v]$ at 66°N integrated vertically between 12 and 25 km for the 1998–1999 winter. A 10-day low-pass filter (see Appendix I) was applied to the data to smooth out the most extreme peaks and filter out anomalous short-term extremes, the inclusion of which would not be conducive to determining an ongoing regional trend. Afterwards, the date with the largest positive mass flux was identified as 8 January 1999, and the date with the largest negative mass flux was identified as 30 November 1998. These events are explored further in Figures 7.8 and 7.9, which show the density ρ (in kg/m^3), the meridional velocity v (in ms^{-2}), and the meridional mass flux F (in kg m^{-2} s^{-2}).

Figures 7.8c, 7.8d, 7.9c, and 7.9d show the total meridional velocity v and the eddy mean meridional velocity v^* across the 65°N parallel, where $v = [v] + v^*$ with $[v]$ as the zonal mean. Given that the plots for v and v^* for each day are almost identical, $v \approx v^*$, and thus it could be assumed that $[v] \sim 0$, in agreement with the QG theory mentioned above. Figures 7.8a, 7.8b, 7.9a, and 7.9b show the absolute density ρ, and density relative to the mean ρ^*, over the polar region. Density is almost uniform over the polar region, with polar values slightly lower than at lower latitudes, and as such ρ acts as a scalar multiplier to v in the ρv term. Figures 7.8e and 7.9e show ρv, which are similar in wave pattern but at a lower magnitude than v.

Given that $v^* \gg [v]$,

$$\rho v = ([\rho] + \rho^*)([v] + v^*) \approx [\rho]v^* + \rho^*v^* \ ,$$

and therefore

$$[\rho v] \approx [\rho][v^*] + [\rho^*v^*]$$
$$\approx [\rho] \cdot 0 + [\rho^*v^*] = [\rho^*v^*] \ .$$

Figure 7.7b shows the eddy meridional mass flux $[\rho^*v^*]$ at 66°N over the same vertical region and time period as Figure 7.7a, while Figure 7.7c shows the multiplied zonal means of density and velocity, $[\rho][v]$. It is clear from Figure 7.7 as a whole that $[\rho v] \not\approx [\rho^*v^*]$, which means that $[v] \not\sim 0$ and the earlier assumption of a fully quasi-geostrophic system should not hold. This in turn suggests that, while $v \approx v^*$, given that the values of ρ and ρ^* are also small, $[v]$ is not negligible when calculating $[\rho v]$, and therefore anomalous mass flux into and out of the polar cap has both QG-like and ageostrophic components:

$$[\rho v] = [\rho][v] + [\rho^*v^*] \ .$$

There is a clear wave-2 pattern in meridional velocity for both days, as well as a wave-2 pattern in the density anomalies of 8 January (Fig. 7.8b), and a wave-1 pattern in the density anomalies of 30 November (Fig. 7.9b). With more dates investigated (not shown), there are notable wave-1 and wave-2 patterns in both the density anomalies and the meridional velocity, and depending on how they interact, this can result in either a wave-1, wave-2, or wave-4 pattern in the ρ^*v^* term (Figs. 7.8f, 7.9f). It is reasonable to conclude from this therefore that there is no systematic preference to tropospheric amplification events occurring specifically in wave-1 or wave-2 states. In other words, there is no wave state that is typical of these events. This supports the similarity between wave-1 and wave-2 plots in Chapter 6, where there is no major difference between curves where the configuration has one or two

Gaussian mountains in either GFDL-SDC or MiMA.

Comparing Figure 7.7a with the pressure anomalies over the same time period in Figure 3.5 shows that the positive mass flux in December does seem to coincide with the positive pressure change, and there is also a small peak in mass flux at the beginning of March, where there is another peak in pressure. However, there are also a number of peaks and troughs in mass flux that do not correspond to any clear pressure events, which may suggest that there are other processes acting to counter meridional mass flux, potentially including vertical mass flux.

As in previous chapters, the analysis here can be repeated in the Southern Hemisphere. Figure 7.10 shows a day with a high positive austral cap mass flux (thus, mass leaving the polar cap). Unlike the Northern Hemisphere examples, it is noticeable in Figure 7.10f that there is larger-scale wave pattern, resulting in more positive mass flux (yellow) across the 65° parallel than negative.
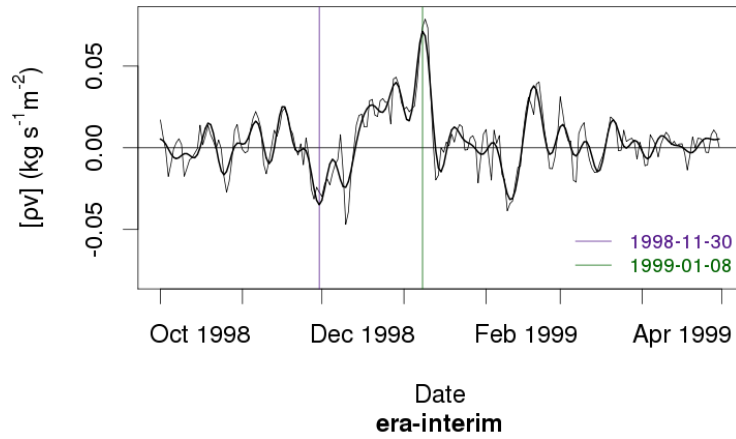
(a) $[\rho v]$
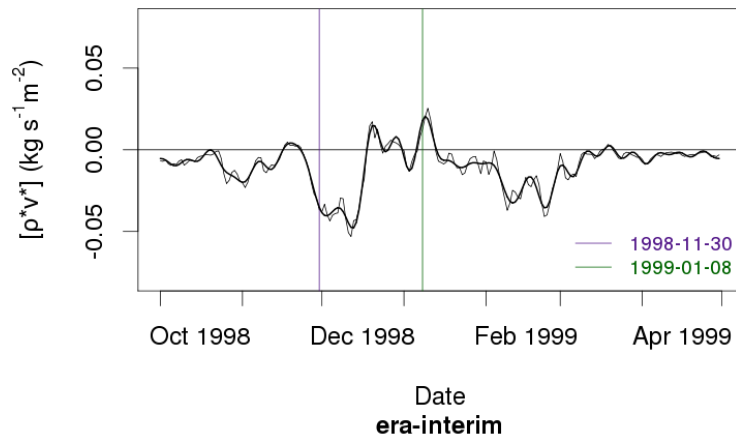
(b) $[\rho^* v^*]$
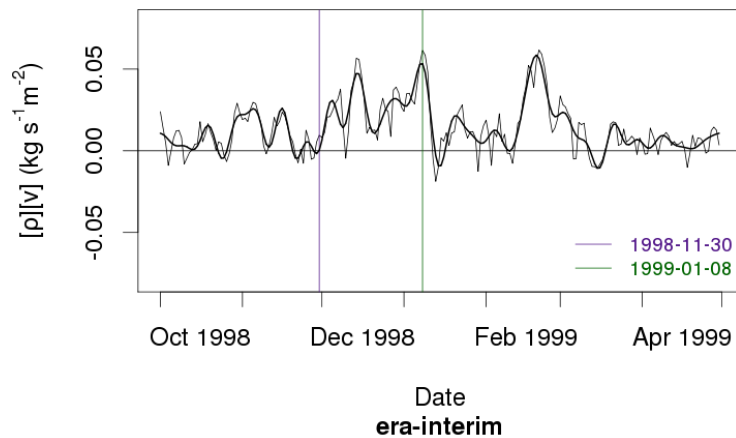
(c) $[\rho][v]$

Figure 7.7: Zonal mean meridional mass flux integrated vertically over 12–25 km at $\phi = 66°N$, winter 1998–1999. The bold curve shows a 10-day low-pass filter.
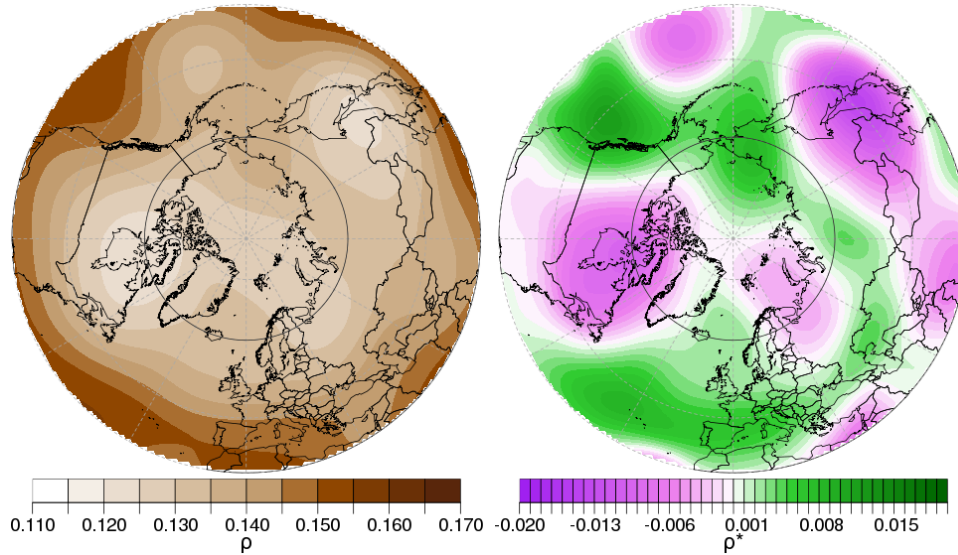
(a) Total air density ρ
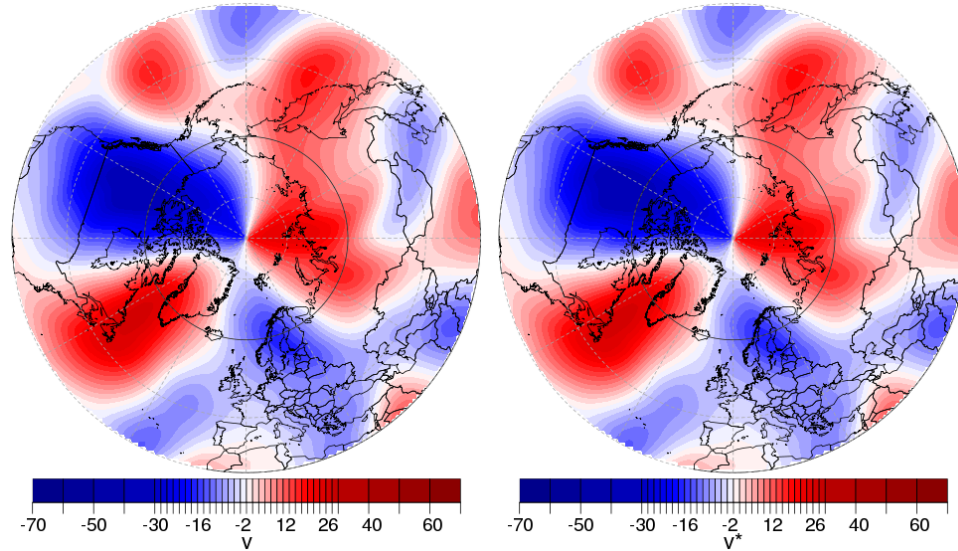
(b) Air density eddy ρ^*

(c) Total meridional wind v

(d) Meridional wind eddy v^*
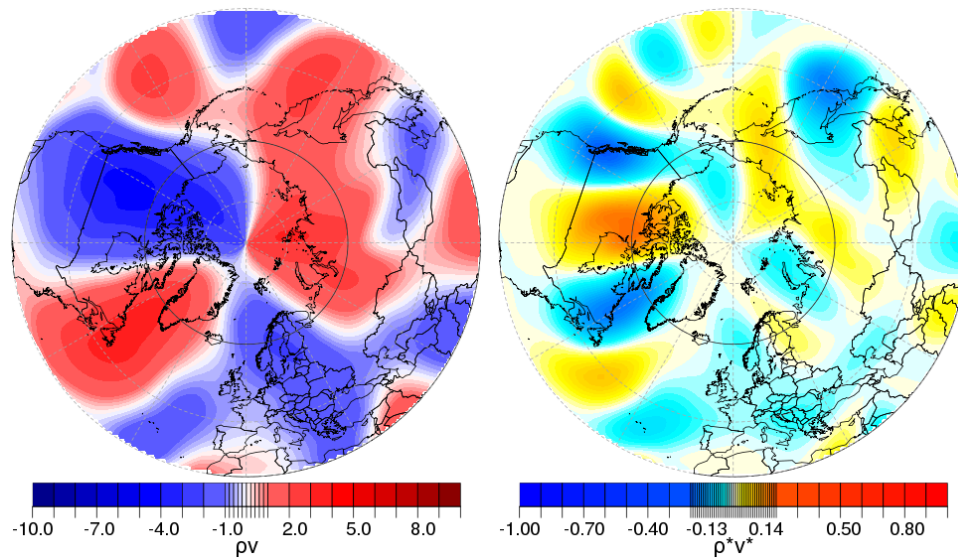
(e) Total mass flux $F = \rho v$

(f) Mass flux eddy $F_E = \rho^* v^*$

Figure 7.8: Vertical averages over 12-25 km for 8th January 1999, Northern Hemisphere. The 65° parallel is shown as a grey line.
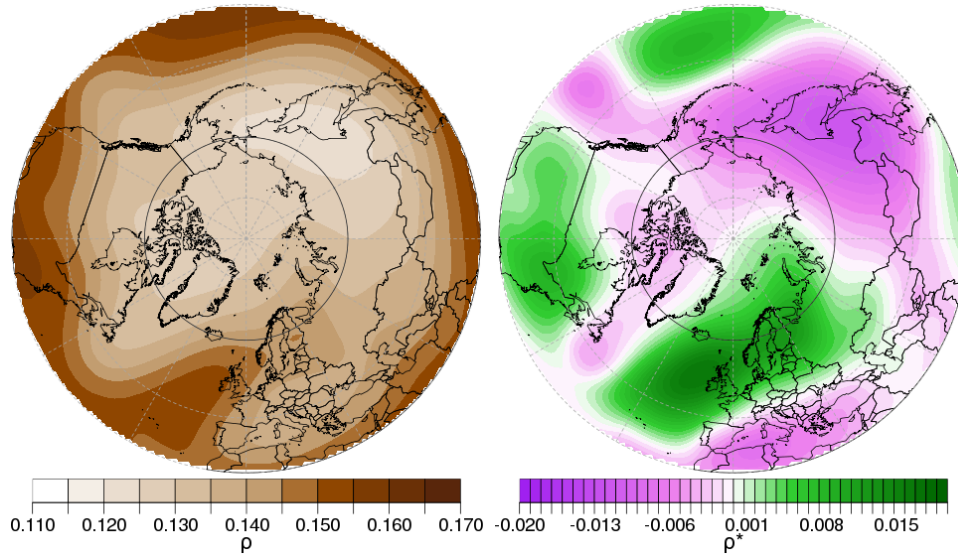
(a) Total air density ρ
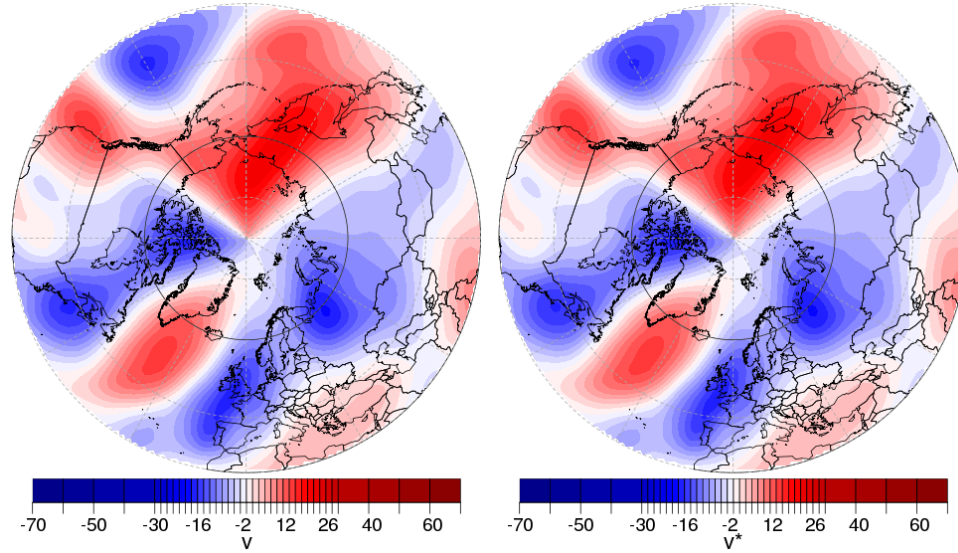
(b) Air density eddy ρ^*

(c) Total meridional wind v

(d) Meridional wind eddy v^*
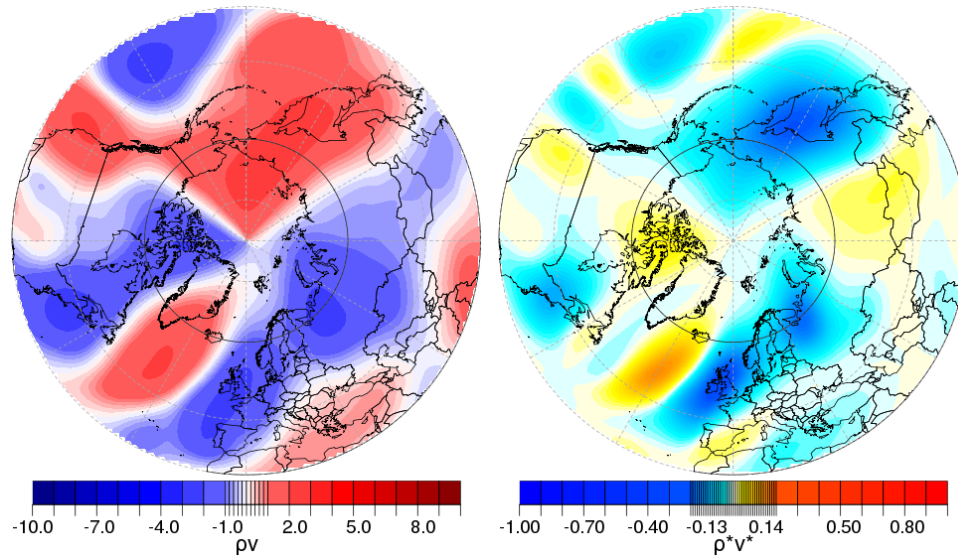
(e) Total mass flux $F = \rho v$

(f) Mass flux eddy $F_E = \rho^* v^*$

Figure 7.9: Vertical averages over 12-25 km for 30th November 1998, Northern Hemisphere. The 65° parallel is shown as a grey line.
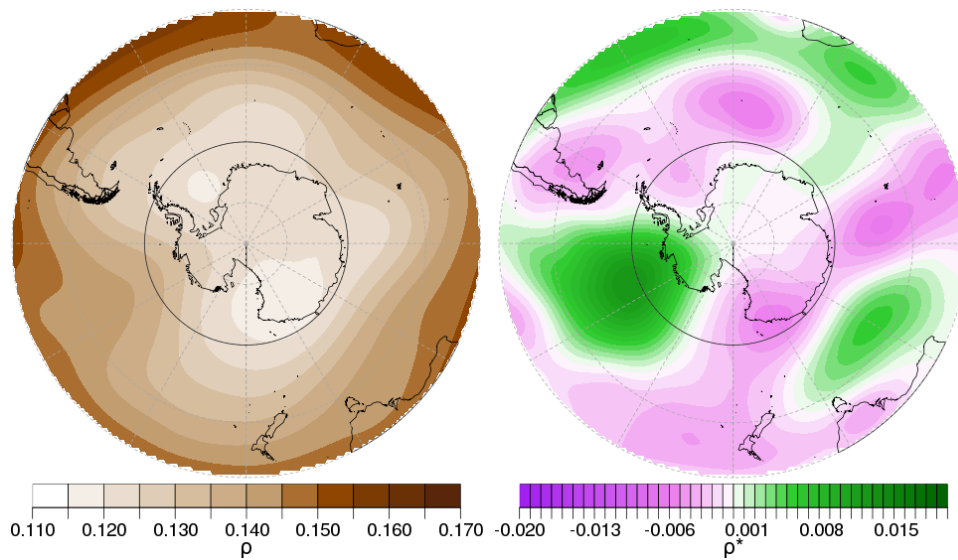
(a) Total air density ρ

(b) Air density eddy ρ^*
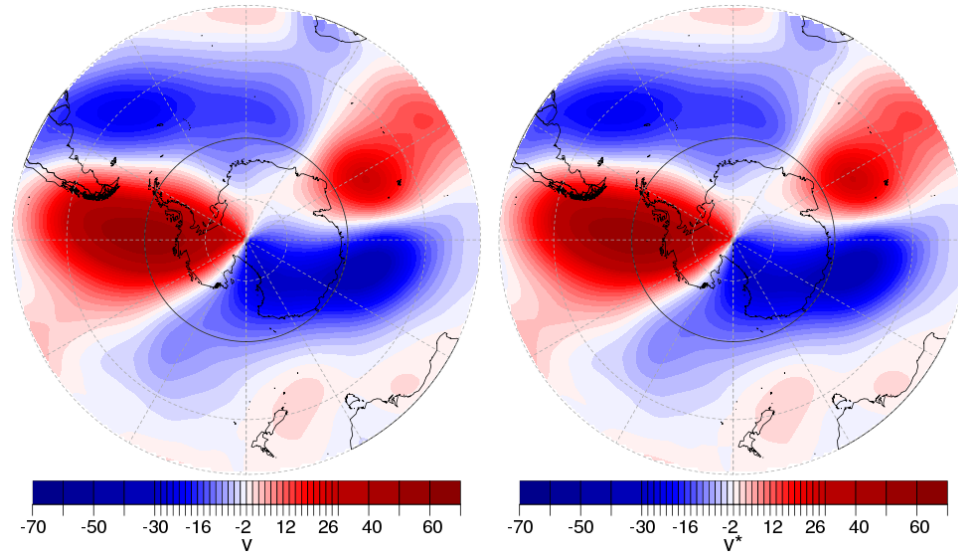
(c) Total meridional wind v

(d) Meridional wind eddy v^*
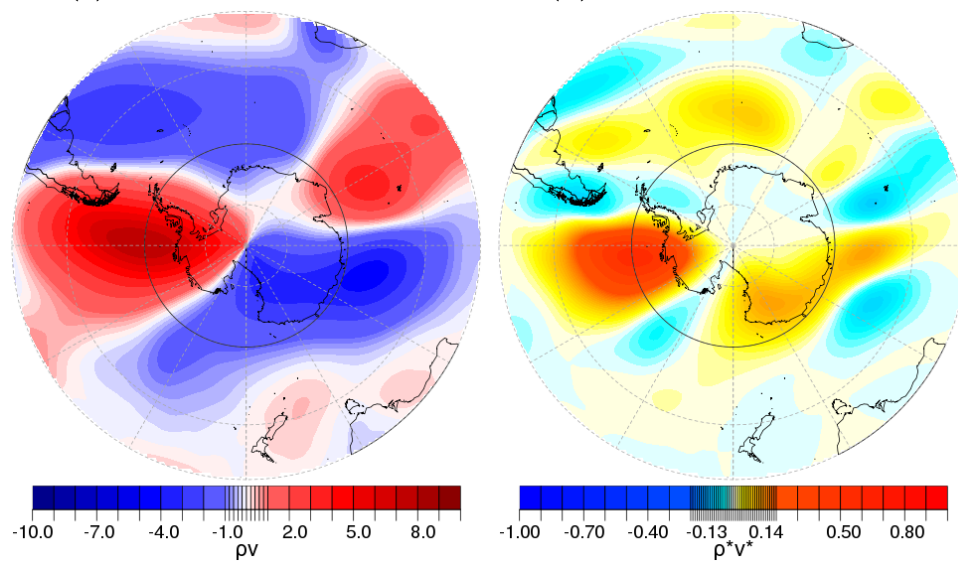
(e) Total mass flux $F = \rho v$

(f) Mass flux eddy $F_E = \rho^* v^*$

Figure 7.10: Vertical averages over 12-25 km for 19th October 1994, Southern Hemisphere. The 65° parallel is shown as a grey line.

7.4   Summary

- Horizontal and vertical mass flux components F and W act to cancel each other out, leaving a very small overall total mass flux. Pressure tendencies are the result of the incomplete cancellation of these two terms. While larger anomalous pressure periods are robust between different reanalysis, the intermediate values are subject to substantial variability.

- $v^* \gg [v]$, but $[\rho v]$ is significantly small that $[v]$ is not negligible. Mass transport F therefore has contribution from both quasi-geostrophic and ageostrophic components.

- There are wave-1 and wave-2 patterns in ρ^* and v, resulting in wave-1, -2, or -4 patterns in $\rho^* v^*$. There appears to be no systematic preference of wave-state coinciding with anomalous mass flux, and thus no wave-state specifically indicative of tropospheric amplification.

8 Conclusions

The main achievements of this thesis are summarised below, followed by suggestions for how this work can be extended in the future.

8.1 Quantifying Stratosphere-Troposphere Coupling

Section 3 introduced the concept of tropospheric amplification, in which a polewards (resp. equatorwards) flow of mass in the tropospheric polar cap region is associated with a larger than normal influx (or outflow) of mass in the stratospheric polar cap region. This can be visualised as either a mean composite of anomalies of p_{cap} from Equation (1), or as a regression slope coefficient β_1 from Equation (2). The regression model uses all the available data, and is more representative of the whole system than the mean composite method. These plots can then be used to quantify tropospheric amplification through regression slope estimates; for example, based on Figure 3.3, a 3.8 hPa increase in pressure at 15–18 km implies that on average there will be a 3.4 hPa increase in pressure at the surface and a 2.2 hPa increase in pressure at the tropopause.

This approach can also be used to quantify the 'strength' of S-T coupling at a particular time. Taking the pressure at 25 km, 16 km, 7 km, and the surface, the values can be compared against each other and the average expected from the ERA-interim regression. The difference between those values and the regression line could then be generated, resulting in a measure of the current S-T coupling. As discussed in Section 4.3, the measure could similarly be taken from the temperature field, which produces a visually similar result.

Tropospheric amplification is shown clearly in every modern reanalysis dataset which started after 1979. In the Northern Hemisphere, representation of the pressure anomaly profile is robust, as the curves are very similar for each reanalysis. There is a clear stratospheric maximum of 2 hPa at 16 km, a minimal value of 1 hPa near the tropopause (7 km), and a tropospheric amplification of 2 hPa near the surface. In the Southern Hemisphere, the thickness of the Antarctic ice cap and the lack

of middle-atmosphere observations results in less agreement between the reanalyses. There is no particular benefit to using any one of the more recent reanalysis datasets over another, and depending on what data is available, both the 25 km pressure data (p_{25}) and the 100 hPa temperature data (T_{100}) can be used to produce similar results.

Quantification of S-T coupling using pressure and height is relatively easy to understand, compared to more complex metrics such as PV diagnostics. As shown in Chapter 4, it is clear that temperature and pressure are a valid proxy for the same information—particularly at certain altitudes where their correlation is very high—so if any of the necessary data are not readily available, either can be used to produce a similar result.

8.2 Climate model simulation of Tropospheric Amplification

By comparing results from reanalysis data with those from complex GCMs from the CMIP5 project, it was discovered that 'high-top' models with a lid of above 1 hPa, and therefore a more realistic stratosphere, were better at recreating tropospheric amplification than 'low-top' models. This suggests that a resolved stratosphere makes climate models more accurate, and that without that, a substantial amount of necessary information would be omitted.

Correlation between the regression slope profiles for CMIP5 models and those of reanalysis is another way that a metric can be derived from this phenomenon, as it can be used to quantify how closely any particular model comes to recreating this aspect of S-T coupling with respect to ERA-interim. Low-top models generally have a lower correlation value between their β_1 and that of ERA-interim, of between 0.42 and 0.75 in the Northern Hemisphere, while high-top models have a correlation of 0.72 to 0.98. This same method could be used to quantify the S-T coupling accuracy of many more models. The investigation could be improved by repeating the regression model analysis for climate models using their T_{100} data, as was done with the reanalysis data, in order to compare and contrast their β_1 profiles.

The study of more idealised models with varying complexity revealed that GFDL-

SDC, a dry core model with Newtonian cooling, could not recreate the tropospheric amplification process. When radiative schemes were replaced with ones which included moisture and ozone, as in MiMA, tropospheric amplification began to appear in the Northern Hemisphere when topographical features were also present in the model. This implies that in the Northern Hemisphere, the phenomenon is linked to effects resulting from topography, such as asymmetries in the circulation and an increase in stratospheric variability, which then cause baroclinic instability. In the Southern Hemisphere, identifying a specific causal process was inconclusive, but again, the result was most accurate when stratospheric variability was closest to that of the reanalysis.

8.3   Tropospheric Amplification in the Future

Future climate projection simulations from CMIP5 models revealed that there are no substantial changes in tropospheric amplification in the Northern Hemisphere over the next 100 years. There was a suggestion from a few of the eleven models that there may be a slightly larger tropospheric amplification effect in the first half of the 21st century, and a slightly smaller one in the latter half of the century, but this result was not consistent between the models.

What was most apparent in the investigation of RCP scenario simulations was the large variation between climate models. The climate change responses of one model varied much less from that model's historical simulation than each of the different climate models' historical and RCP simulations varied from each other.

In the Southern Hemisphere, the results were even less consistent. A few models showed that tropospheric amplification in this hemisphere did not match the profile seen in reanalysis, while others suggested there would not be much change from the current profile. With little change projected, there is no precedent for needing to alter forecasting or climate management systems to accommodate for changes in the system.

8.4 Stratospheric and Tropospheric Mass Flux

Hydrostatic balance and mass continuity shows there is a relationship between mass flux and pressure change, but the fact that this is the result of a difference calculation between two large values (except at the surface) means no clear results can been identified. This suggests that a different approach is needed, including considering integrals over time of mass flux instead of finite difference of pressure, which should smooth out the natural variability and fluctuations, instead of amplifying them.

Comparing the vertical and horizontal components of mass flux into the polar cap has shown that the effect of vertical mass movement is almost exactly sufficient to cancel out the horizontal component, meaning both are major factors in the change of pressure in the region. As such, there was no clear period of time in which significantly more mass entered the polar cap region compared with what left the region, so there was no clear indication of a period of prolonged, higher-than-average, high pressure.

Looking at the regional distribution of mass movement has not revealed any obvious patterns in the geographic location of poleward vs equatorward mass flux, but it has revealed interesting results about the contribution of the zonal mean and eddy components of pressure and velocity. While the mean meridional velocity $[v]$ is negligible next to the eddy component of velocity v^*, it is clear that $[v]$ is a dominant factor in determining the overall zonal mean mass flux $[\rho v]$ on a particular day. This means that zonal mean mass flux has significant contributions from both quasi-geostrophic and ageostrophic components.

8.5 Future Work

Studies of sudden stratospheric warmings are prevalent in existing literature, but studies of anomalous stratospheric cool periods do not appear to be. Extending the work of Section 3.4, which looked at the *effects* of SSWs and anomalous stratospheric cooling, by comparing the *mechanics* behind these phenomena, may increase the understanding of the processes behind both, given how similar their associated pressure changes are.

On the modelling side, existing evaluations of long-term trends, both in this thesis and in previous papers, can be extended into projections of future climate. Additionally, models could be developed to better represent stratospheric processes – it is mentioned numerous times here how including stratospheric processes greatly increases a model's effectiveness in representing the true climate state. Continuing investigation into the differences between the simple model GFDL-SDC and the intermediate model MiMA, future investigations may wish to test the outcomes with certain parts of the Rapid Radiative Transfer Model disabled. Specific things to investigate would include adding water vapour parameters to the previously-dry GFDL-SDC, or including the ozone part of RRTM in MiMA without water vapour. From this, it may be possible to determine in more detail the parameters, and thus the processes, required for a model to recreate tropospheric amplification.

Appendices

A CMIP5 Models

Table A.1: CMIP5 model output analysed in this thesis, including model name, modelling group/institution, atmospheric horizontal grid resolution, number of vertical levels, model 'lid', and datasets used (World Climate Research Programme, 2013).

Model Name	Institution[i]	Horizontal Resolution	Vertical Levels	Grid Top[ii]	Runs
BCC-CSM1.1	BCC	T42	26	2.917 hPa (low)	Historical RCP 4.5 RCP 8.5
BNU-ESM	GCESS	T42	26	2.194 hPa (low)	Historical RCP 4.5 RCP 8.5
CanESM2	CCCMA	Spectral T63	35	0.5 hPa (high)	Historical RCP 4.5 RCP 8.5
CMCC-CESM	CMCC	3.75° × 3.75° (T31)	39	0.01 hPa (high)	Historical RCP 8.5
CMCC-CM	CMCC	0.75° × 0.75° (T159)	31	10 hPa (low)	Historical RCP 4.5 RCP 8.5
CMCC-CMS	CMCC	1.875° × 1.875° (T63)	95	0.01 hPa (high)	Historical RCP 4.5 RCP 8.5
CNRM-CM5	CNRM-CERFACS	TL127	31	10 hPa (low)	Historical RCP 4.5 RCP 8.5
MPI-ESM-LR	MPI-M	1.8° T63	47	0.01 hPa (high)	Historical RCP 4.5 RCP 8.5
MPI-ESM-MR	MPI-M	1.8° T63	95	0.01 hPa (high)	Historical RCP 4.5 RCP 8.5
MPI-ESM-P	MPI-M	1.8° T63	47	0.01 hPa (high)	Historical
NorESM1-M	NCC	1.9° × 2.5° (lat × lon)	26	2.194 hPa (low)	Historical RCP 4.5 RCP 8.5

---

[i]See Table A.2 for Modelling Group / Centre names

[ii]Models with a lid above 1 hPa (∼48 km) are considered 'high-top', while models with lids below this are considered 'low-top' (e.g. Charlton-Perez et al., 2013; Cagnazzo and Manzini, 2009)

Table A.2: CMIP5 Modelling Groups and Institution IDs

Institution ID	Modelling Centre / Group
BCC	Beijing Climate Center, China Meteorological Administration
CCCMA	Canadian Centre for Climate Modelling and Analysis
CMCC	Centro Euro-Mediterraneo per i Cambiamenti Climatici
CNRM-CERFACS	Centre National de Recherches Météorologiques / Centre Européen de Recherche et Formation Avancée en Calcul Scientifique
GCESS	College of Global Change and Earth System Science, Beijing Normal University
MPI-M	Max-Plank-Institut für Meteorologie
NCC	Norwegian Climate Centre

B Reanalysis Datasets

- **ECMWF ERA-40** (Uppala et al., 2005) data have been provided by ECMWF, obtained from the ECMWF Data Server at http://apps.ecmwf.int/datasets/

- **ECMWF ERA-interim** (Dee et al., 2011) data have been provided by ECMWF, obtained from the ECMWF Data Server at http://apps.ecmwf.int/datasets/

- **JMA JRA-55** (Ebita et al., 2011) Japanese 55-year Reanalysis project, carried out by the Japan Meteorological Agency (JMA), data obtained from Dr Blanca Ayarzaguena

- **NCEP-DOE Reanalysis 2** (Kanamitsu et al., 2002) data provided by the NOAA/OAR/ESRL PSD, Boulder, Colorado, USA, from their Web site at http://www.esrl.noaa.gov/psd/

- **NCEP-NCAR Reanalysis 1** (Kalnay et al., 1996) data provided by the NOAA/OAR/ESRL PSD, Boulder, Colorado, USA, from their Web site at http://www.esrl.noaa.gov/psd/

Table B.1: Reanalysis datasets analysed in this thesis, including reanalysis name, reference paper, time period, atmospheric horizontal grid resolution, number of vertical levels, and model 'lid'

Reanalysis Name	Reference	Period	Horizontal Grid	Vertical Levels	Grid Top
ERA-40	Uppala et al. (2005)	Sep 1957 – Aug 2002	3°	23	1 hPa
ERA-interim	Dee et al. (2011)	Jan 1979 – Dec 2015	3°	37	1 hPa
JRA-55	Ebita et al. (2011)	Jan 1958 – Dec 2015	2.5°	37	1 hPa
NCEP-DOE	Kanamitsu et al. (2002)	Jan 1979 – Dec 2013	2.5°	17	10 hPa
NCEP-NCAR	Kalnay et al. (1996)	Jan 1948 – Dec 2013	2.5°	17	10 hPa

C Geopotential Height Interpolation

The data was interpolated from pressure levels as follows:

- The zonal average of geopotential Φ was taken,

$$[\Phi]_{\phi,p,t} \approx n_\lambda^{-1} \sum_{\lambda=0}^{n_\lambda} \Phi_{\lambda,\phi,p,t} \ ,$$

with longitude λ, at each latitude ϕ, pressure level p, and time step t.

- Geopotential height was calculated, $Z = \frac{[\Phi]}{g}$, where $g \approx 9.81$.

- Cubic spline interpolation was used, taking $Z_{\phi,t}$ on $\log(p)$ as the input, and producing output ξ at kilometre increments of Z.

- Pressure values corresponding to these output levels were calculated as $p = 10^\xi$.

D   Removing the Annual Cycle

Removing the annual cycle involves two primary steps: calculating the climatology, and calculating the anomalies. To calculate the climatology C, all values for a single day index t are summed, and divided by the total number of occurrences of that day index n_t (this is usually the number of years in the dataset), generating an average:

$$C_t = \frac{\sum_{i=1}^{n_t} Z_{t,i}}{n_t}$$

For datasets including leap years, such as ERA-interim, Day 366 is calculated as the average of Day 365 and Day 1 (regardless of whether Day 366 actually exists in any given year), $C_{366} = \dfrac{C_{365} + C_1}{2}$, so that the climatology will have 366 days. A 90-day low-pass filter is then applied to the climatology to smooth any extreme values. To calculate the anomalies, the climatology is subtracted from the initial dataset by day index (this means that the anomaly for Day 200 is always based on the climatology of Day 200, regardless of whether it was the 19th or 18th of July).

$$Z_t^* = Z_t - C_t, \quad t = 1, \ldots, 366$$

The anomaly dataset is the same size as the initial dataset, and contains the data used after 'removing the annual cycle'.

E   Calculating p_{cap}

This method can be used to calculate the polar cap average time series of any data set, but since pressure is the primary consideration, polar cap pressure $\hat{p} \approx p_{\text{cap}}$ will be the focus.

The area of the polar cap is:

$$A = \int_A \mathrm{d}A = \int_{\phi_0}^{\frac{\pi}{2}} a \, \mathrm{d}\phi \int_0^{2\pi} \mathrm{d}\lambda \, a \cos(\phi) = 2\pi a^2 (1 - \sin(\phi_0))$$

Pressure averaged over the polar cap is:

$$\hat{p} = \frac{\int p \, \mathrm{d}A}{A}$$

1. If the data has four dimensions, longitude λ, latitude ϕ, height Z and time t, take the zonal average:

$$[p]_{\phi,Z,t} \approx n_\lambda^{-1} \sum_\lambda p_{\lambda,\phi,Z,t} \tag{16}$$

2. Based on the model grid resolution, latitude ϕ is represented by the discrete parallels y. ERA-interim, for example, has a $3° \times 3°$ resolution, so for the polar cap $|\phi| > \phi_0 = 65°$, ERA-interim's polar cap is $y = 66°, 69°, \ldots, 87°, 90°$.

3. A weighting factor h_y is calculated for each latitude y to compensate for the reduction in grid-box size as the data nears the pole:

$$h_y = \cos\left(\frac{\pi y}{180}\right) \tag{17}$$

4. Calculate the polar cap average p_{cap} over latitudes y at each timestep t and height Z:

$$p_{\text{cap},Z,t} = \frac{\sum_y [p]_{y,Z,t} \, h_y}{\sum_y h_y} \tag{18}$$
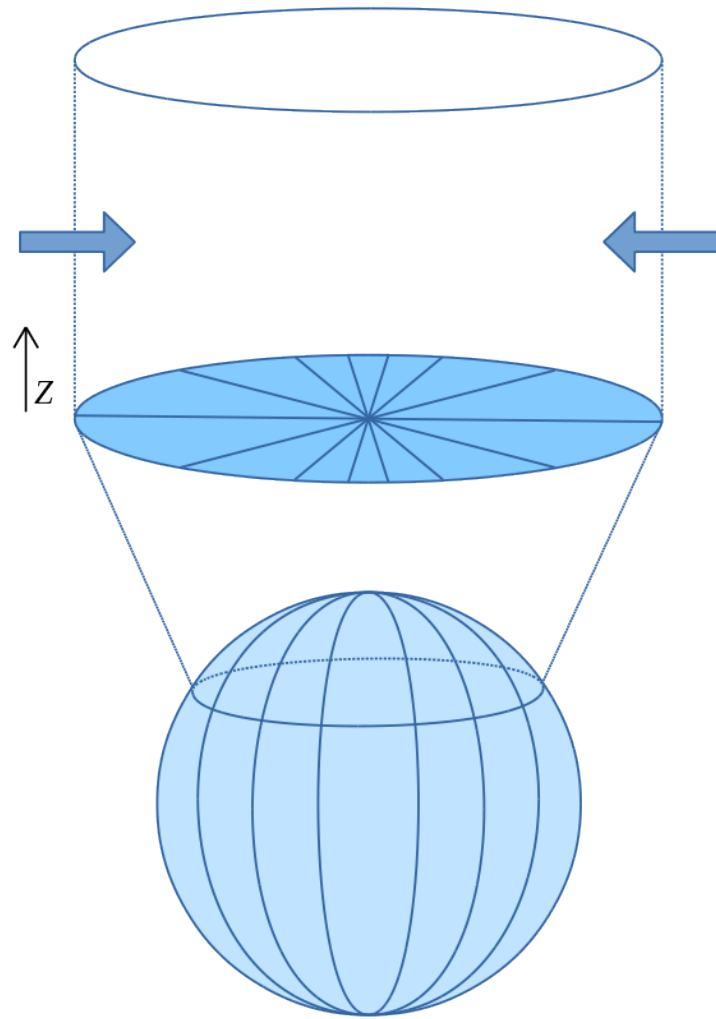
Figure E.1: Diagram of mass movement into the column of air above the 'polar cap'.

F Calculating the Annular Mode

To calculate the annular mode, starting with the anomaly dataset of geopotential height X, only the data from the hemisphere in question is retained (equator to pole, whole year), and the iterative EOF projection method from Baldwin et al. (2009) is used. EOF $\mathbf{u}$ and PC $\mathbf{a}$, as in Section 2.4, are initially drawn from the Normal distribution $N(0, 1)$, and the iteration is

$$\mathbf{u} = \frac{X^T \mathbf{a}}{\mathbf{a}^T \mathbf{a}} \qquad\qquad (*)$$
$$\mathbf{a} = \frac{XW\mathbf{u}}{\mathbf{u}^T W \mathbf{u}}$$

The weighting matrix W contains the cosine of latitude. As in Baldwin and Dunkerton (2001), a separate EOF calculation is made for each pressure level, and as in Baldwin and Thompson (2009), the EOFs are calculated from zonal mean anomalies. The annular mode spatial pattern $\mathbf{u}$ at each pressure level is then found by projecting the original daily mean geopotential height data X onto the first PC time series $\mathbf{a}$ using the same equation $(*)$ (Baldwin and Thompson, 2009; Baldwin et al., 2009). The time series of the annular mode is directly the first principal component $\mathbf{a}$. Note that this EOF calculation is invariant to sign, so the decision was made to follow the same positive/negative convention as Baldwin and Dunkerton (2001).

G Calculating the 95% Confidence Interval

The confidence interval C is calculated from the slope parameter β_1 of Equation 2,

$$C = (\beta_1 - c\,\sigma_E\ , \beta_1 + c\,\sigma_E)\ ,$$

where $c = 1.96$ is the critical value under the standard Normal distribution $X \sim N(0, 1)$, such that $P(-c < X < c) = 0.95$, and σ_E is the standard error of β_1 from the linear model, $\sigma_E = \sqrt{\frac{\sigma^2}{n}}$ where σ is the standard deviation.

The 95% pointwise confidence band is the 95% confidence interval applied to β_1 at each geopotential height level.

H   GFDL-SDC Model Configurations

- h is the height of 'topography' in the model, which provides orographic forcing.

- A is the amplitude of the polar vortex, calculated as the difference in relaxation temperature between the winter pole and equinox conditions at 1 hPa.

- τ_t is the relaxation time at the equator at 100 hPa.

- τ_p is the relaxation time at high latitudes at 100 hPa.

- N is the wave number of the topography.

Table H.1: Model configurations of the GFDL-SDC model as used by Jucker et al. (2014)

Simulation	h (km)	A (K)	τ_t (days)	τ_p (days)	N
Run 1	0	0	40	20	0
Run 2	1.5	0	40	20	1
Run 3	1.5	0	40	20	2
Run 4	3	0	10	20	1
Run 5	3	0	10	20	2
Run 6	3	0	20	20	1
Run 7	3	0	20	20	2
Run 8	3	0	20	30	1
Run 9	3	0	20	30	2
Run 10	3	0	20	40	1
Run 11	3	0	20	40	2
Run 12	3	0	30	10	1
Run 13	3	0	30	10	2
Run 14	3	0	30	20	1
Run 15	3	0	30	20	2
Run 16	3	0	30	30	1
Run 17	3	0	30	30	2
Run 18	3	0	30	40	1

Table H.1: Model configurations of the GFDL-SDC model as used by Jucker et al. (2014)

Simulation	h (km)	A (K)	τ_t (days)	τ_p (days)	N
Run 19	3	0	30	40	2
Run 20	3	0	40	20	1
Run 21	3	0	40	20	2
Run 22	3	0	40	30	1
Run 23	3	0	40	30	2
Run 24	3	0	40	40	1
Run 25	3	0	40	40	2
Run 26	3	5	40	20	1
Run 27	3	5	40	20	2
Run 28	3	10	40	20	1
Run 29	3	10	40	20	2
Run 30	3	15	40	20	1
Run 31	3	15	40	20	2
Run 32	3	20	40	20	1
Run 33	3	20	40	20	2
Run 34	5	0	40	20	1
Run 35	5	0	40	20	2

I Low-Pass Filter

The low-pass filter is started by creating a weighting vector w based on the total number of days N, and the number of days used in the filter c (in this case, 10 or 90), where

$$
\begin{aligned}
w_j = & 1 \text{ for } j < \frac{N}{0.8c} \\
& 1 \text{ for } j > N - \frac{N}{0.8c} \\
& 0 \text{ otherwise},
\end{aligned}
$$

which is then used in a fast Fourier transform. The Fourier transform of the data x is taken, multiplied by the vector w, and then inverted with an inverse Fourier transform to produce the result y. Let f be the Fourier transform of x, where n is the length of f:

$$
f_h = \sum_{k=1}^{n} x_k e^{\frac{1}{n}(-2\pi i(k-1)(h-1))} \text{ for } h = 1, \ldots, n
$$

Then let $z = fw$, where p is the length of z and m is the length of x:

$$
y_h = \frac{1}{m}\left[\sum_{k=1}^{p} z_k e^{\frac{1}{p}(2\pi i(k-1)(h-1))}\right] \text{ for } h = 1, \ldots, p
$$

Bibliography

Ambaum, M.H.P. and B.J. Hoskins, 2002: The NAO Troposphere-Stratosphere Connection. *J. Climate*, **15**, 1969–1978.

Ambaum, M.H.P., B.J. Hoskins, and D.B. Stephenson, 2001: Arctic Oscillation or North Atlantic Oscillation? *J. Climate*, **14**, 3495–3507.

Andrews, D.G. and M.E. McIntyre, 1976: Planetary Waves in Horizontal and Vertical Shear: The Generalized Eliassen-Palm Relation and the Mean Zonal Acceleration. *J. Atmos. Sci.*, **33**(11), 2031–2048.

Andrews, D.G. and M.E. McIntyre, 1978a: An exact theory of nonlinear waves on a Lagrangian-mean flow. *J. Fluid Mech.*, **89**(4), 609–646.

Andrews, D.G. and M.E. McIntyre, 1978b: Generalized Eliassen-Palm and Charney-Drazin Theorems for Waves on Axisymmetric Mean Flows in Compressible Atmospheres. *J. Atmos. Sci.*, **35**, 175–185.

Anstey, J.A., P. Davini, L.J. Gray, T.J. Woollings, N. Butchart, C. Cagnazzo, B. Christiansen, S.C. Hardiman, S.M. Osprey, and S. Yang, 2013: Multi-model analysis of Northern Hemisphere winter blocking: Model biases and the role of resolution. *J. Geophys. Res. Atmos.*, **118**, 3956–3971.

Baldwin, M.P., T. Birner, and B. Ayarzagena, submitted 2017: Polar Amplification of Stratospheric Variability. *Nature*. Submitted to *Nature*, 2017.

Baldwin, M.P. and T.J. Dunkerton, 1999: Propagation of the Arctic Oscillation from the stratosphere to the troposphere. *J. Geophys. Res.*, **104**(D24), 30 937–30 946.

Baldwin, M.P. and T.J. Dunkerton, 2001: Stratospheric Harbingers of Anomalous Weather Regimes. *Science*, **294**, 581–584.

Baldwin, M.P., D.B. Stephenson, and I.T. Jolliffe, 2009: Spatial Weighting and Iterative Projection Methods for EOFs. *J. Climate*, **22**, 234–243.

Baldwin, M.P., D.B. Stephenson, D.W.J. Thompson, T.J. Dunkerton, A.J. Charlton, and A. O'Neill, 2003: Stratospheric Memory and Skill of Extended-Range Weather Forecasts. *Science*, **301**, 636–640.

Baldwin, M.P. and D.W.J. Thompson, 2009: A critical comparison of stratosphere-troposphere coupling indices. *Q. J. R. Meteorol. Soc.*, **135**, 1661–1672.

Black, R.X., 2002: Stratospheric Forcing of Surface Climate in the Arctic Oscillation. *J. Climate*, **15**, 268–277.

Butchart, N., 2014: The Brewer-Dobson circulation. *Rev. Geophys.*, **52**, 157–184.

Butchart, N., A.J. Charlton-Perez, I. Cionni, S.C. Hardiman, P.H. Haynes, K. Krger, P.J. Kushner, P.A. Newman, S.M. Osprey, J. Perlwitz, M. Sigmond, L. Wang, H. Akiyoshi, J. Austin, S. Bekki, A. Baumgaertner, P. Braesicke, C. Brhl, M. Chipperfield, M. Dameris, S. Dhomse, V. Eyring, R. Garcia, H. Garny, P. Jckel, J. Lamarque, M. Marchand, M. Michou, O. Morgenstern, T. Nakamura, S. Pawson, D. Plummer, J. Pyle, E. Rozanov, J. Scinocca, T.G. Shepherd, K. Shibata, D. Smale, H. Teyssdre, W. Tian, D. Waugh, and Y. Yamashita, 2011: Multimodel climate and variability of the stratosphere. *J. Geophys. Res.*, **116**, D05 102.

Cagnazzo, C. and E. Manzini, 2009: Impact of the Stratosphere on the Winter Tropospheric Teleconnections between ENSO and the North Atlantic and European Region. *J. Climate*, **22**, 1223–1238.

Charlton, A.J., A. O'Neill, D.B. Stephenson, W.A. Lahoz, and M.P. Baldwin, 2003: Can knowledge of the state of the stratosphere be used to improve statistical forecasts of the troposphere? *Q. J. R. Meteorol. Soc.*, **129**, 3205–3224.

Charlton-Perez, A.J., M.P. Baldwin, T. Birner, R.X. Black, A.H. Butler, N. Calvo, N.A. Davis, E.P. Gerber, N. Gillett, S. Hardiman, J. Kim, K. Krger, Y.Y. Lee, E. Manzini, B.A. McDaniel, L. Polvani, T. Reichler, T.A. Shaw, M. Sigmond, S.W. Son, M. Toohey, L. Wilcox, S. Yoden, B. Christiansen, F. Lott, D. Shindell, S. Yukimoto, and S. Watanabe, 2013: On the lack of stratospheric dynamical variability in low-top versions of the CMIP5 models. *J. Geophys. Res.: Atmos.*, **118**, 1–12.

Cohen, N.Y., E.P. Gerber, and O. Bhler, 2013: Compensation between Resolved and Unresolved Wave Driving in the Stratosphere: Implications for Downward Control. *J. Atmos. Sci.*, **70**, 3780–3798.

Dee, D.P., S.M. Uppala, A.J. Simmons, P. Berrisford, P. Poli, S. Kobayashi, U. Andrae, M.A. Balmaseda, G. Balsamo, P. Bauer, P. Bechtold, A.C.M. Beljaars, L. van de Berg, J. Bidlot, N. Bormann, C. Delsol, R. Dragani, M. Fuentes, A.J.

Geer, L. Haimberger, S.B. Healy, H. Hersbach, E.V. Hlm, L. Isaksen, P. Kll-berg, M. Khler, M. Matricardi, A.P. McNally, B.M. Monge-Sanz, J.J. Morcrette, B.K. Park, C. Peubey, P. de Rosnay, C. Tavolato, J.N. Thpaut, and F. Vitart, 2011: The ERA-Interim reanalysis: configuration and performance of the data assimilation system. *Quarterly Journal of the Royal Meteorological Society*, **137**(656), 553–597. ISSN 1477-870X. doi:10.1002/qj.828. URL `http://dx.doi.org/10.1002/qj.828`.

Dunkerton, T., 1978: On the Mean Meridional Mass Motions of the Stratosphere and Mesosphere. *J. Atmos. Sci.*, **35**, 2525–2333.

Ebita, A., S. Kobayashi, Y. Ota, M. Moriya, R. Kumabe, K. Onogi, Y. Harada, S. Yasui, K. Miyaoka, K. Takahashi, H. Kamahori, C. Kobayashi, H. Endo, M. Soma, Y. Oikawa, and T. Ishimizu, 2011: The Japanese 55-year Reanalysis "JRA-55" An Interim Report. *SOLA*, **7**, 149–152. doi:10.2151/sola.2011-038.

Eyring, V., J.M. Arblaster, I. Cionni, J. Sedlacek, J. Perlwitz, P.J. Young, S. Bekki, D. Bergmann, P. Cameron-Smith, W.J. Collins, G. Faluvegi, K.D. Gottschaldt, L.W. Horowitz, D.E. Kinnison, J.F. Lamarque, D.R. Marsh, D. Saint-Martin, D.T. Shindell, K. Sudo, S. Szopa, and S. Watanabe, 2013: Long-term ozone changes and associated climate impacts in CMIP5 simulations. *J. Geophys. Res.: Atmos.*, **118**, 5029–5060.

Eyring, V., N.R.P. Harris, M. Rex, T.G. Shepherd, D.W. Fahey, G.T. Amanatidis, J. Austin, M.P. Chipperfield, M. Dameris, P.M.D.F. Forster, A. Gettelman, H.F. Graf, T. Nagashima, P.A. Newman, S. Pawson, M.J. Prather, J.A. Pyle, R.J. Salawitch, B.D. Santer, and D.W. Waugh, 2005: A Strategy for Process-Oriented Validation of Coupled Chemistry–Climate Models. *Bull. Am. Met. Soc.*, **86**, 1117–1133.

Flato, G., J. Marotzke, B. Abiodun, P. Braconnot, S. Chou, W. Collins, P. Cox, F. Driouech, S. Emori, V. Eyring, C. Forest, P. Gleckler, E. Guilyardi, C. Jakob, V. Kattsov, C. Reason, and M. Rummukainen, Evaluation of Climate Models. In T. Stocker, D. Qin, G.-K. Plattner, M. Tignor, S. Allen, J. Boschung, A. Nauels, Y. Xia, V. Bex, and P. Midgley, (eds.), *Climate Change 2013: The Physical*

Science Basis. Contribution of Working Group I to the Fifth Assessment Report of the Intergovernmental Panel on Climate Change (Cambridge University Press, Cambridge, United Kingdom and New York, NY, USA, 2013). ISBN 978-1-107-66182-0. doi:10.1017/CBO9781107415324.020. URL `www.climatechange2013.org`.

Garfinkel, C.I. and D.L. Hartmann, 2007: Effects of the El Niño-Southern Oscillation and the Quasi-Biennial Oscillation on polar temperatures in the stratosphere. *J. Geophys. Res.*, **112**, D19 112.

Garfinkel, C.I. and D.L. Hartmann, 2011a: The Influence of the Quasi-Biennial Oscillation on the Troposphere in Winter in a Hierarchy of Models. Part I: Simplified Dry GCMs. *J. Atmos. Sci.*, **68**, 1273–1289.

Garfinkel, C.I. and D.L. Hartmann, 2011b: The Influence of the Quasi-Biennial Oscillation on the Troposphere in Winter in a Hierarchy of Models. Part II: Perpetual Winter WACCM Runs. *J. Atmos. Sci.*, **68**, 2026–2041.

Gerber, E.P., 2012: Stratospheric versus Tropospheric Control of the Strength and Structure of the Brewer-Dobson Circulation. *J. Atmos. Sci.*, **69**, 2857–2877.

Gerber, E.P., M.P. Baldwin, H. Akiyoshi, J. Austin, S. Bekki, P. Braesicke, N. Butchart, M. Chipperfield, M. Dameris, S. Dhomse, S.M. Frith, R.R. Garcia, H. Garny, A. Gettelman, S.C. Hardiman, A. Karpechko, M. Marchand, O. Morgenstern, J.E. Nielsen, S. Pawson, T. Peter, D.A. Plummer, J.A. Pyle, E. Rozano, J.F. Scinocca, T.G. Shepherd, and D. Smale, 2010: Stratosphere-troposphere coupling and annular mode variability in chemistry-climate models. *J. Geophys. Res.*, **115**, D00M06.

Gerber, E.P., A. Butler, N. Calvo, A. Charlton-Perez, M. Giorgetta, E. Manzini, J. Perlwitz, L.M. Polvani, F. Sassi, A.A. Scaife, T.A. Shaw, S.W. Son, and S. Watanabe, 2012: Assessing and Understanding the Impact of Stratospheric Dynamics and Variability on the Earth System. *Bull. Am. Met. Soc.*, **93**, 845–859.

Gerber, E.P., C. Orbe, and L.M. Polvani, 2009: Stratospheric influence on the tropospheric circulation revealed by idealized ensemble forecasts. *Geophys. Res.*

Lett., **36**, L24 801.

Hannachi, A., I.T. Jolliffe, and D.B. Stephenson, 2007: Empirical orthogonal functions and related techniques in atmospheric science: A review. *Int. J. Climatol.*, **27**, 1119–1152.

Hannachi, A., I.T. Jolliffe, D.B. Stephenson, and N. Trendafilov, 2006: In search of simple structures in climate: simplifying EOFs. *Int. J. Climatol.*, **26**, 7–28.

Hartley, D.E., J.T. Villarin, R.X. Black, and C.A. Davis, 1998: Anewperspective on the dynamical link between the stratosphere and troposphere. *Nature*, **391**, 471–474.

Hartmann, D.L., J.M. Wallace, V. Limpasuvan, D.W.J. Thompson, and J.R. Holton, 2000: Can ozone depletion and global warming interact to produce rapid climate change? *Proc. Natl. Acad. Sci.*, **97**(4), 1412–1417.

Haynes, P., 2005: Stratospheric Dynamics. *Annu. Rev. Fluid Mech.*, **37**, 263–293.

Haynes, P.H., C.J. Marks, M.E. McIntyre, T.G. Shepherd, and K.P. Shine, 1991: On the 'Downward Control' of Extratropical Diabatic Circulations by Eddy-Induced Mean Zonal Forces. *J. Atmos. Sci.*, **48**(4), 651–678.

Hitchcock, P. and I.R. Simpson, 2014: The Downward Influence of Stratospheric Sudden Warmings. *J. Atmos. Sci.*, **71**, 3856–3876.

Holton, J.R., P.H. Haynes, M.E. McIntyre, A.R. Douglass, R.B. Rood, and L. Pfister, 1995: Stratosphere-Troposphere Exchange. *Rev. Geophys.*, **33**, 403–439.

Holton, J.R. and H.C. Tan, 1980: The Influence of the Equatorial Quasi-Biennial Oscillation on the Global Circulation at 50 mb. *J. Atmos. Sci.*, **37**, 2200–2208.

Ivy, D.J., S. Solomon, and D.W.J. Thompson, 2014: On the Identification of the Downward Propagation of Arctic Stratospheric Climate Change over Recent Decades. *J. Climate*, **27**, 2789–2799.

Jones, C.D., J.K. Hughes, N. Bellouin, S.C. Hardiman, G.S. Jones, J. Knight, S. Liddicoat, F.M. O'Connor, R.J. Andres, C. Bell, K.O. Boo, A. Bozzo, N. Butchart, P. Cadule, K.D. Corbin, M. Doutriaux-Boucher, P. Friedlingstein, J. Gornall, L. Gray, P.R. Halloran, G. Hurtt, W.J. Ingram, J.F. Lamarque, R.M. Law, M. Meinshausen, S. Osprey, E.J. Palin, L.P. Chini, T. Raddatz, M.G. Sander-

son, A.A. Sellar, A. Schurer, P. Valdes, N. Wood, S. Woodward, M. Yoshioka, and M. Zerroukat, 2011: The HadGEM2-ES implementation of CMIP5 centennial simulations. *Geosci. Model Dev.*, **4**, 543–570.

Jucker, M., 2017: mjucker/mima: Mima v1.0. doi:10.5281/zenodo.321708.

Jucker, M., S. Fueglistaler, and G.K. Vallis, 2013: Maintenance of the Stratospheric Structure in an Idealized General Circulation Model. *J. Atmos. Sci.*, **70**, 3341–4458.

Jucker, M., S. Fueglistaler, and G.K. Vallis, 2014: Stratospheric sudden warmings in an idealized GCM. *J. Geophys. Res.: Atmos.*, **119**(19), 11,054–11,064. ISSN 2169-8996. doi:10.1002/2014JD022170. URL `http://dx.doi.org/10.1002/2014JD022170`.

Jucker, M. and E.P. Gerber, 2017: Untangling the Annual Cycle of the Tropical Tropopause Layer with an Idealized Moist Model. *J. Climate*, **30**, 7339–7358.

Kalnay, E., M. Kanamitsu, R. Kistler, W. Collins, D. Deaven, L. Gandin, M. Iredell, S. Saha, G. White, J. Woollen, Y. Zhu, A. Leetmaa, R. Reynolds, M. Chelliah, W. Ebisuzaki, W. Higgins, J. Janowiak, K.C. Mo, C. Ropelewski, J. Wang, R. Jenne, and D. Joseph, 1996: The NCEP/NCAR 40-Year Reanalysis Project. *Bulletin of the American Meteorological Society*, **77**(3), 437–471. doi:10.1175/1520-0477(1996)077⟨0437:TNYRP⟩2.0.CO;2.

Kanamitsu, M., W. Ebisuzaki, J. Woollen, S.K. Yang, J.J. Hnilo, M. Fiorino, and G.L. Potter, 2002: NCEP–DOE AMIP-II Reanalysis (R-2). *Bulletin of the American Meteorological Society*, **83**(11), 1631–1643. doi:10.1175/BAMS-83-11-1631.

Keeble, J., P. Braesicke, N.L. Abraham, H.K. Roscoe, and J.A. Pyle, 2014: The impact of polar stratospheric ozone loss on Southern Hemisphere stratospheric circulation and climate. *Atmos. Chem. Phys.*, **14**, 13 705–13 717.

Kidston, J., A.A. Scaife, S.C. Hardiman, D.M. Mitchell, N. Butchart, M.P. Baldwin, and L.J. Gray, 2015: Stratospheric influence on tropospheric jet streams, storm tracks and surface weather. *Nature Geoscience*, **8**, 433–440.

Kushner, P.J. and L.M. Polvani, 2004: Stratosphere–Troposphere Coupling in a Relatively Simple AGCM: The Role of Eddies. *J. Climate*, **17**, 629–639.

Limpasuvan, V. and D.L. Hartmann, 2000: Wave-Maintained Annular Modes of Climate Variability. *J. Climate*, **13**, 4414–4429.

Matsuno, T. and K. Nakamura, 1979: The Eulerian- and Lagrangian-Mean Meridional Circulations in the Stratosphere at the Time of a Sudden Warming. *J. Atmos. Sci.*, **36**, 640–654.

Maycock, A.C., 2016: The contribution of ozone to future stratospheric temperature trends. *Geophys. Res. Lett.*, **43**, 4609–4616.

Mlawer, E.J., S.J. Taubman, P.D. Brown, M.J. Iacono, and S.A. Clough, 1997: Radiative transfer for inhomogeneous atmospheres: RRTM, a validated correlated-k model for the longwave. *J. Geophys. Res.*, **102**(D14), 16 663–16 682.

Osprey, S.M., L.J. Gray, S.C. Hardiman, N. Butchart, and T.J. Hinton, 2013: Stratospheric Variability in Twentieth-Century CMIP5 Simulations of the Met Office Climate Model: High Top versus Low Top. *J. Climate*, **26**, 1595–1606.

Pelly, J.L. and B.J. Hoskins, 2003: A New Perspective on Blocking. *J.Atmos. Sci.*, **60**.

Perlwitz, J. and N. Harnik, 2003: Observational Evidence of a Stratospheric Influence on the Troposphere by Planetary Wave Reflection. *J. Climate*, **16**, 3011–3026.

Plumb, R.A., 2002: Stratospheric Transport. *J. Meteorol. Soc. Jpn.*, **80**(4B), 793–809.

Polvani, L.M. and P.J. Kushner, 2002: Tropospheric response to stratospheric perturbations in a relatively simple general circulation model. *Geophys. Res. Lett.*, **29**(7), 40–43.

Reichler, T., P.J. Kushner, and L.M. Polvani, 2005: The Coupled StratosphereTroposphere Response to Impulsive Forcing from the Troposphere. *J. Atmos. Sci.*, **62**, 3337–3352.

Scott, D., 1979: On Optimal and Data-Based Histograms. *Biometrika*, **66**(3), 605–610.

Seviour, W.J.M., N. Butchart, and S.C. Hardiman, 2012: The Brewer-Dobson circulation inferred from ERA-Interim. *Q. J. R. Meteorol. Soc.*, **138**, 878–888.

Simpson, I.R., M. Blackburn, and J.D. Haigh, 2009: The Role of Eddies in Driving

the Tropospheric Response to Stratospheric Heating Perturbations. *J. Atmos. Sci.*, **66**, 1347–1365.

Simpson, I.R., P. Hitchcock, T.G. Shepherd, and J.F. Scinocca, 2011: Stratospheric variability and tropospheric annularmode timescales. *Geophys. Res. Lett.*, **38**, L20 806.

Song, Y. and W.A. Robinson, 2004: Dynamical Mechanisms for Stratospheric Influences on the Troposphere. *J. Atmos. Sci.*, **61**, 1711–1725.

Stolarski, R.S., A.R. Douglass, M. Gupta, P.A. Newman, S. Pawson, M.R. Schoeberl, and J.E. Nielsen, 2006: An ozone increase in the Antarctic summer stratosphere: A dynamical response to the ozone hole. *Geophys. Res. Lett.*, **33**, L21 805.

Sun, L., G. Chen, and W.A. Robinson, 2014: The Role of Stratospheric Polar Vortex Breakdown in Southern Hemisphere Climate Trends. *J. Atmos. Sci.*, **71**, 2335–2353.

Taylor, K.E., R.J. Stouffer, , and G.A. Meehl, 2012: An Overview of CMIP5 and the Experiment Design. *Bull. Am. Met. Soc.*, **93**, 485–498.

Thompson, D.W.J., M.P. Baldwin, and S. Solomon, 2005: Stratosphere-Troposphere Coupling in the Southern Hemisphere. *J. Atmos. Sci.*, **62**, 708–715.

Thuburn, J. and A.A. White, 2012: A geometrical view of the shallow-atmosphere approximation, with application to the semi-Lagrangian departure point calculation. *Q. J. R. Meteorol. Soc.*, **139**, 261–268.

Uppala, S.M., P.W. Kllberg, A.J. Simmons, U. Andrae, V.D.C. Bechtold, M. Fiorino, J.K. Gibson, J. Haseler, A. Hernandez, G.A. Kelly, X. Li, K. Onogi, S. Saarinen, N. Sokka, R.P. Allan, E. Andersson, K. Arpe, M.A. Balmaseda, A.C.M. Beljaars, L.V.D. Berg, J. Bidlot, N. Bormann, S. Caires, F. Chevallier, A. Dethof, M. Dragosavac, M. Fisher, M. Fuentes, S. Hagemann, E. Hlm, B.J. Hoskins, L. Isaksen, P.A.E.M. Janssen, R. Jenne, A.P. Mcnally, J.F. Mahfouf, J.J. Morcrette, N.A. Rayner, R.W. Saunders, P. Simon, A. Sterl, K.E. Trenberth, A. Untch, D. Vasiljevic, P. Viterbo, and J. Woollen, 2005: The ERA-40 re-analysis. *Quarterly Journal of the Royal Meteorological Society*, **131**(612), 2961–3012. ISSN 1477-870X. doi:10.1256/qj.04.176. URL `http://dx.doi.org/`

10.1256/qj.04.176.

Wallace, J.M., R.L. Panetta, and J. Estberg, 1993: Representation of the Equatorial Stratospheric Quasi-Biennial Oscillation in EOF Phase Space. *J. Atmos. Sci.*, **50**, 1751–1762.

Watson, P.A.G. and L.J. Gray, 2014: How Does the Quasi-Biennial Oscillation Affect the Stratospheric Polar Vortex? *J. Atmos. Sci.*, **71**, 391–409.

Woollings, T., A. Charlton-Perez, S. Ineson, A.G. Marshall, and G. Masato, 2010: Associations between stratospheric variability and tropospheric blocking. *J. Geophys. Res.*, **115**, D06 108.

World Climate Research Programme, 2013: Coupled Model Intercomparison Project Phase 5 (CMIP5). NCAS British Atmospheric Data Centre, *2016-08-02*. http://catalogue.ceda.ac.uk/uuid/85c7d0b09c974bd6abb07a324c2f427b.

Yang, H., K.K. Tung, and E. Olaguer, 1990: Nongeostrophic Theory of Zonally Averaged Circulation. Part II: Eliassen-Palm Flux Divergence and Isentropic Mixing Coefficient. *J. Atmos. Sci.*, **47**(2), 215–241.